

QUANTUM SENSING OF PHOTONIC SPIN DENSITY WITH SPIN QUBITS

by

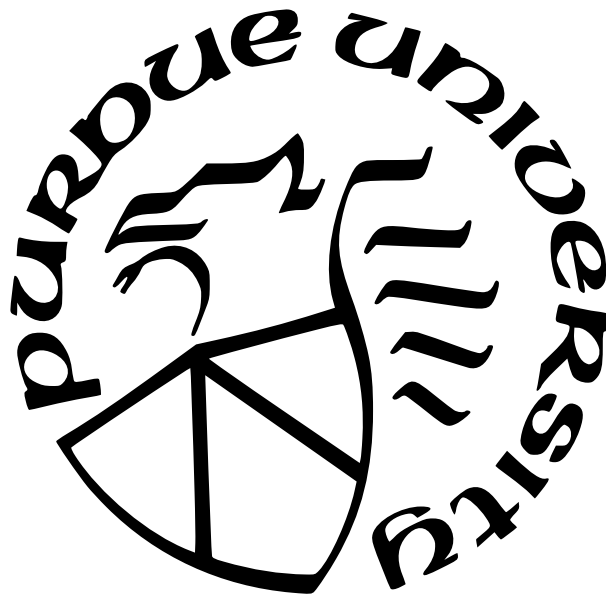
Farid Kalhor

A Dissertation

Submitted to the Faculty of Purdue University

In Partial Fulfillment of the Requirements for the degree of

Doctor of Philosophy



School of Electrical and Computer Engineering

West Lafayette, Indiana

December 2021

**THE PURDUE UNIVERSITY GRADUATE SCHOOL
STATEMENT OF COMMITTEE APPROVAL**

Dr. Zubin Jacob, Chair

School of Electrical and Computer Engineering

Dr. Andrew M. Weiner

School of Electrical and Computer Engineering

Dr. Daniel S. Elliott

School of Electrical and Computer Engineering

Dr. Dana Weinstein

School of Electrical and Computer Engineering

Approved by:

Dr. Dimitrios Peroulis

ACKNOWLEDGMENTS

I would like to thank all the people with whom my path crossed during the past eight years. Most of all, I want to thank my advisor Zubin Jacob. He patiently nurtured me as a student and supported me through the harder days of work. I cannot thank him enough for everything I have learned during this period. His vision and instinct have always amazed me and I hope to have inherited some of his scientific ambition and courage.

Many thanks to my good colleague, friend and roommate Saman Jahani. He introduced me to Zubin and helped me throughout this period. We had many joyful debates from our work in the lab to when is the last day of good weather in Edmonton. I owe him a great debt of gratitude and many cups of tea.

I was lucky to work alongside a large group of talented people in Zubin Jacob's group. I am thankful to all of them for creating a productive and friendly environment and for helping me through discussions in group meetings and coffee breaks. I had the pleasure of working with some of them more closely. I worked with Leif Bauer shoulder to shoulder in the lab while Li-Ping Yang backed us with his thorough quantum theories. Shoaib Mahmud joined our team in the last year of my PhD and I hope he has as much fun as I had. I was lucky to work with Sarang Pendharker and Todd Van Mechelen and learn from their insightful theories. Thanks to Sean Molesky and Cristian Cortes for sharing their scientific rigor and intuition with me, Ashwin Boddeti for his encyclopedic knowledge, Ward Newman for helping me learn to work in a lab, Tyler Sentz and Xueji Wang for beating me at pool, Prashant Shekhar and Ryan Starko-Bowes for beating me in squash, Angshuman Deka for his valuable friendship and good taste in coffee, Sathwik Bharadwaj for taking the time to read my dissertation and comment on it, Farahd Khosravi for his soothing music, Vishal Choudhury and Chinmay Khandekar for sharing with me memorable moments and Indian food.

I would like to thank Dr. Sunil Bhave for granting me access to his lab and sharing the resources and expertise of his group, Dr. Noah Opondo for his skillful work in the cleanroom to patiently fabricate samples for my experiments, Dr. Mahdi Hosseini for sharing his knowledge with me whenever I ran into obstacles in my work, Dr. Thomas Thundat for

his advisory role and kind support at the University of Alberta and Dr. Andrew Weiner, Dr. Daniel Elliott, and Dr. Dana Weinstein for taking the time to serve on my advisory committee and their valuable comments on my dissertation.

Our work at Birck Nanotechnology Center would not be possible without the continuous support of the wonderful staff members. I would like to thank all of them especially Mary Jo Totten, Nancy Black, Brenda Meador, and Kyle Corwin for kindly helping me with equipment purchases and logistics.

I am grateful to all my friends for their constant love and support. Thanks to Fariborz Daneshvar and Sattar Soltani for all the tea break we had. I was fortunate to be near my old friends Alireza Sojoudi, Shaghayegh Aslanpour, Abdollah Farhoodi, and Nazanin Khazra while studying abroad. They kept me connected to the Iranian culture and more importantly to Iranian food. Thanks to Zach, Shellie, Nate, Haley, and Lucas Maddox for letting me into their family. I learned a lot about the American culture from them and enjoyed watching movies and eating food with them.

Finally, I want to thank my parents Morteza and Farah, my brothers Reza and Kian, and my sister-in-law Alexis. They are the ones I look up to and admire the most. Cyrus, my nephew, was born while I was writing this dissertation and brought much joy to our lives.

PREFACE

The first chapter of this thesis is an introduction to the field of near-field photonic spin. We present an overview to the new findings in this field that have emerged over the past decade. Then the achievements of this field are summarized to show the need for a platform to sense and exploit the near-field properties of photonic spin density (PSD) in quantum technologies. We then introduce nitrogen-vacancy (NV) centers in diamond as a promising tool for this purpose. Lastly, the properties and capabilities of NV centers are discussed before we present the original contributions of this thesis.

Chapter 2 is a reproduction of previously published work

- F. Kalhor, T. Thundat, and Z. Jacob, “Universal spin-momentum locked optical forces,” *Applied Physics Letters*, vol. 108, no. 6, p. 061102, Feb. 2016.

This chapter focuses on studying the PSD in evanescent waves and the optical forces that arise from universal spin-momentum locking for these waves. We also study this effect for the case of total internal reflection and optical waveguide modes.

Chapter 3 is a reproduction of previously published work

- F. Kalhor, L.-P. Yang, L. Bauer, and Z. Jacob, “Quantum sensing of photonic spin density using a single spin qubit,” *Physical Review Research*, vol. 3, no. 4, p. 043007, Oct.2021.

This chapter demonstrates that NV centers in diamond can coherently interact with a circularly polarized free space optical beam at room temperature. We show that the strength of this interaction is proportional to PSD of the beam.

Chapter 4 is based on an unpublished work

- F. Kalhor, N. F. Opondo, S. Mahmud, L. Bauer, L.-P. Yang, S. A. Bhave, and Z. Jacob, “Optically induced static magnetic field in ensemble of nitrogen-vacancy centers in diamond,” *manuscript in preparation*.

This chapter demonstrates the optically induced magnetic field for an ensemble of NV centers. We furthermore characterize the wavelength dependence of this effect and determine the

optimal wavelength for optically induced magnetic fields for the spin qubit system at room temperature.

TABLE OF CONTENTS

LIST OF TABLES	10
LIST OF FIGURES	11
ABBREVIATIONS	18
ABSTRACT	20
1 INTRODUCTION	22
1.1 Near-field Properties of Optical Fields	23
1.1.1 Spin-momentum locking in evanescent fields	25
1.1.2 Spin based directional coupling of light into guided modes	27
1.1.3 Novel applications based on near-field photonic spin density	27
1.2 Nitrogen-vacancy Centers in Diamonds	29
1.2.1 Electronic structure of NV centers	30
1.2.2 Polarization and readout	31
1.2.3 Coherent manipulation of spin-states	33
1.2.4 Coherence time and dynamical decoupling	34
1.2.5 Fabrication of NV centers	35
1.3 Layout of the Thesis	36
2 UNIVERSAL SPIN-MOMENTUM LOCKED OPTICAL FORCES	38
2.1 Outline of the Problem	39
2.2 Spin Density and Transverse Spin in Evanescent Waves	39

2.3	Anomalous Optical Force and Directional Coupling	40
2.4	Spin-momentum Locked Optical Force in Total Internal Reflection	42
2.5	Spin-momentum Locked Optical Force in an Optical Fiber	44
2.6	Conclusion	46
3	QUANTUM SENSING OF PHOTONIC SPIN DENSITY USING A SINGLE SPIN QUBIT	48
3.1	Theoretical Model of Spin Qubit Interacting with Photonic Spin Density	49
3.2	Experimental Demonstration Using a Single NV Center	54
3.3	Effective Static Magnetic Field in Optical Waveguides	57
3.4	Conclusion	58
4	OPTICALLY INDUCED STATIC MAGNETIC FIELD IN ENSEMBLE OF NITROGEN-VACANCY CENTERS IN DIAMOND	60
4.1	Outline of the Problem	60
4.2	Coherence Time and Sensitivity	62
4.3	Optically Induced Magnetic Field for an Ensemble of NV Centers	65
4.4	Wavelength Dependence of the Optically Induced Magnetic Field	66
4.5	Conclusion	68
5	CONCLUSIONS	69
	REFERENCES	71
A	OPTICAL FORCE EQUATIONS	82
A.1	Electric and Magnetic Stokes Parameters	82

A.2	Optical Force on a Chiral Particle	82
A.3	Polarizability of the Chiral Particle	83
B	CALCULATIONS FOR PHOTONIC SPIN DENSITY-INDUCED EFFECTIVE STATIC MAGNETIC FIELD	84
B.1	Energy Structure of NV Center	84
B.2	Energy Shifts and Effective Magnetic Field for the Ground-state Spin	85
C	EFFECTIVE STATIC MAGNETIC FIELD FOR PROBE QUBITS	89
C.1	Influence of Coupling between NV Center's Excited-state Sublevels on the Effective Static Magnetic Field	91
D	EXPERIMENTAL SETUP	94
E	PULSE SEQUENCE	97
F	FULL-WAVE ANALYSIS OF PROPAGATION OF LIGHT IN AFM TIP	100

LIST OF TABLES

3.1	Dynamical decoupling measurement parameters used for the results shown in Fig. 3.4.	54
B.1	Selection rules for optical transitions between the triplet ground states and the triplet excited states. We note that any transition connected with circularly polarized light can also be stimulated with linearly polarized lights. But the corresponding transition strength will be smaller.	86

LIST OF FIGURES

- 1.1 Spin-momentum locking in total internal reflection (TIR). (a) A propagating plane wave enters the prism beyond the critical angle and an evanescent wave appears on the opposing side. A component of PSD transverse to the direction of propagation exist in the evanescent wave. The direction of this component is locked to the direction of propagation (κ) and direction of decay (η). (b) The direction of decay is set by the boundary and a growing wave away from the boundary violates causality. In order to generate a transverse spin density in the opposite direction compared to panel (a) the direction of propagation has to change. 25
- 1.2 Spin-momentum locking in an optical waveguide. Reprinted with permission from [15]. (a) Schematic of a ridge waveguide with the PSD near the waveguide for a TE-like mode. (b) Electric component of PSD in the vicinity of the waveguide showing the dependence on the direction of decay. The PSD has opposite direction on the two sides of the waveguide following the spin-momentum locking phenomenon. (c) Same as (b) for the magnetic component of PSD. The magnetic component has higher intensity above and below the waveguide due to the direction of the magnetic field in the optical mode. . . . 26
- 1.3 Demonstration of the spin-momentum locking phenomenon for a spinning dipole coupling to SPP modes and high-k modes of a dielectric medium. (a)-(c) A spinning dipole is placed near the surface of a silver film ((a) and (b)) and a dielectric surface ((c), $\epsilon = 2$). The radiation from the dipole couples to the modes of these surfaces in a preferential direction determined by the spinning direction of the dipole. This directional coupling arises from the matching between the spinning direction of the dipole and the spinning fields (PSD) of the optical mode. (d)-(f) The same dipole radiating between two symmetric interfaces. The directional coupling disappears due to the added symmetry to the system. The additional layer allows for decaying waves in both directions, suppressing the directional coupling effect. The corresponding E_z component of the electric field on the $z = 0$ plane is plotted in all panels. The amplitude of the dipole is $\mathbf{p} = p_0(3i\hat{\mathbf{x}} + \hat{\mathbf{z}})$ and has a wavelength of $\lambda = 500$ nm. 28

1.4	Utilizing PSD in the near-field unlocks novel applications. (a) Schematic of photonic spin and momentum transverse to the direction of propagation of a beam for an evanescent wave. Reprinted with permission from [18]. (b) Spin-texture in the momentum space showing a topologically nontrivial state. Reprinted with permission from [26]. (c) Formation of an optical skyrmion when an optical beam interacts with a SPP mode. Reprinted with permission from [25]. (d) Nonreciprocal waveguide using a tapered optical fiber and spin-polarized atoms trapped next to the optical fiber. The interaction between the spin-polarized atoms and the spin of the optical beam only allows for transmission in one direction determined by spin-momentum locking for evanescent waves. Reprinted with permission from [24]. (e) Polarization dependent response in a YIG microcavity. The different transverse spin of the two polarizations traveling in a nanofiber excites different modes of a cavity resulting in a polarization dependent response. Reprinted with permission from [28]. (f) Photonic-spin based interface between a quantum dot and a waveguide. The interaction between the spin of the quantum dot and the spin of the optical mode of a waveguide determines the direction of coupling of light into the waveguide. Reprinted with permission from [29].	29
1.5	Atomic structure and energy levels of NV center. (a) NV center consists of a substitutional nitrogen atom next a vacancy defect. (b) Simplified energy levels and transitions of NV center showing a 637nm optical transition between the ground and excited states. The ground and excited states are both spin triplets. The transition through the dark state is spin-flipping and allows for optical polarization and readout of the NV center's spin state. (c) Ground state energy levels of NV center showing the zero-field splitting and Zeeman splitting between $ \pm 1\rangle$ states due to an applied magnetic field. An optically detected magnetic resonance (ODMR) measurement can reveal the resonance gaps between the $ 0\rangle$ and $ \pm 1\rangle$ states.	30
1.6	Quantum sensing with NV centers. (a) NV centers in diamond are used to probe magnetic excitations in a ferromagnetic microdisk. Reprinted with permission from [32]. (b) Single NV centers in diamond are used to probe the thermally induced magnetic noise in the vicinity of a silver film. The noise reduces the coherence time of the NV center. Reprinted with permission from [34]. (c) An NV center is used to scan the magnetic field generated near a flake of CrI_3 with nanometer resolution. Reprinted with permission from [33]. (d) An NV center is used to generate a map of the magnetic field produced by an skyrmion at room temperature. Reprinted with permission from [35].	31
2.1	Direction of transverse spin in evanescent fields for (a) total internal reflection, (b) surface plasmon polariton, and (c) optical fiber. The blue vectors show the electric field at an instance of time and the orange vectors show the direction of transverse spin. In all cases the direction of momentum, direction of decay, and transverse spin follow a right-hand rule.	41

- 2.2 Lateral force caused by transverse spin of the evanescent fields. (a) An achiral non-magnetic particle is placed in an evanescent field generated by total internal reflection of a p polarized incident beam. The handedness of the scattered radiation follows the direction of transverse spin of the evanescent field and is locked to the direction of momentum of the incident field. Due to symmetry, the scattered waves propagating in $+\hat{y}$ and $-\hat{y}$ directions have equal power densities which leads to zero lateral force on the particle. (b) A chiral particle is placed in an evanescent field experiences a lateral force. The lateral force is proportional to the transverse spin of the evanescent field. The spin of the evanescent field causes a directional scattering by the particle. The direction of the scattered radiation is parallel (anti-parallel) to the direction of spin, therefore, the recoil force caused by the directional radiation will be anti-parallel (parallel) to the direction of spin. (c) Reciprocal setup of (a). An achiral particle placed near a dielectric surface is illuminated by a circularly polarized beam. The scattered radiation by the particle propagates directionally inside the dielectric and exerts a recoil force on the particle. 43
- 2.3 Optical forces on a chiral particle (solid line) and an achiral particle (dots) in an evanescent field. (a) Schematic of a chiral particle placed near a prism showing the direction of incident beam and the forces. (b) Time averaged force in \hat{x} direction. This component of the force is dominated by the gradient force and is toward the prism. (c) Time averaged force in \hat{y} direction. This component of the force is proportional to the transverse spin. (d) Time averaged force in \hat{z} direction. This component of the force is dominated by radiation pressure. The particle is $100nm$ away from the surface of the prism. See Appendix A for the polarizability of the chiral and achiral particles. The incident beam is p polarized with wavelength $\lambda = 5 \mu m$ and carries a power of $p = 50 mW/mm^2$. The refractive index of the prism is $n = 3.5$ and the horizontal axis is related to the incident angle of the beam. 44
- 2.4 Direction of Poynting vector, spin density and spin density force on a chiral particle for $m = 1$ and $m = -1 HE_{11}$ modes. (a) and (b) Direction of Poynting vector outside the optical fiber for the two modes. (c) and (d) Direction of spin density and spin density force outside the optical fiber for the two modes. The longitudinal component of the spin density has opposite directions for the two modes, but, its transverse component is in the same direction for both modes which shows the spin-momentum locking in evanescent fields. The direction of spin density force on a chiral particle placed outside the optical fiber is also shown. The longitudinal component of the force, F_z , has opposite directions for the two modes, but, the transverse component, F_ϕ , is in the same direction for both modes. 45

- 2.5 (a) Schematic of a chiral particle near an optical fiber. (b), (c) and (d) Time averaged optical force in different directions plotted versus radius of the fiber. The solid line shows the force for $m = 1$ mode and the dots show the force for $m = -1$ mode. The \hat{r} component is dominated by the gradient force and has the same value for both modes while the $\hat{\phi}$ component is dominated by the spin density force. The transverse component of the Poynting vector applies a radiation pressure force which is responsible for the difference in the $\hat{\phi}$ component of the force for the two modes. The direction of the transverse spin and transverse spin density force is independent of the OAM of the mode and is locked to its direction of propagation. Both radiation pressure and the spin density forces contribute to the \hat{z} component of the force. The radiation pressure is in $+\hat{z}$ direction for both modes but the spin density force has opposite directions. Therefore, for the $m = 1$ mode the force is in $+\hat{z}$ direction but for the $m = -1$ mode the force is in the opposite direction. The particle is placed $100nm$ away from the surface of the fiber and has the same properties as the particle in Fig. 2.3. The refractive index of the fiber is $n_1 = 1.5$ and the surrounding medium is vacuum. The wavelength of the incident beam is $\lambda = 5\mu m$ and the mode carries a total power of $P = 1\mu W$ 47
- 3.1 Probing PSD with a single NV center. (a) A target beam, red-detuned to the NV center transition, is incident on a single NV center on an AFM tip. We measure the relative energy level shifts in the ground state and show its proportionality to the PSD. The single NV center serves as a room-temperature nanoscale probe for PSD. (b) Ground- and excited-state energy levels of an NV center showing the selection rules for RCP and LCP excitation. (c) Level shifts induced in the ground state due to the virtual transitions under the off-resonant target beam. (d) Power and polarization (spin) dependence of the relative energy shifts in the ground state, resembling Zeeman splitting. An effective static magnetic field is defined as $B_{eff} = (\delta_{+1} - \delta_{-1})/2\gamma$ 51
- 3.2 Effective static magnetic field induced by PSD. (a) A linear polarizer and a quarter wave plate control the PSD. (b) The effective magnetic field calculated for different QWP angles (θ) and alignment angles (ϕ). (c) The effective magnetic field calculated for an NV center in a (100) cut diamond, $\phi = 54.7^\circ$ 53

- 3.3 Isolating the signature of photonic spin density using dynamical decoupling and ac magnetometry with a single spin qubit. (a) Pulse sequence used for measuring the PSD. In each measurement a pair of 532nm laser pulses initialize (polarize) and read out the state of the NV center. During each measurement an XY8 MW pulse performs dynamical decoupling on the spin of the NV center. The target beam, generating the PSD, is turned on and off during the XY8 sequence to generate a net effect on the final state of the NV center. We perform two measurements in which the target beam induces rotations in opposite directions on the spin vector in the Bloch sphere. By subtracting the outcome of these two measurement we eliminate any systematic noise in the measurement. [(b)-(f)] Bloch sphere representation of the state of the qubit after polarization, before the XY8 pulse, after the XY8 pulse, and before readout. Panels (e) and (f) show a schematic comparison between the PSD-induced rotations in measurement 1 and measurement 2. The PSD is generated by the target beam. RO, readout; Pol, polarizing. 55
- 3.4 Demonstration of nanoscale PSD probe with a single NV center. (a) Simplified schematic of the experimental setup. (b) Pulse sequence showing dynamical decoupling for ac magnetometry and amplitude modulation of the target beam to generate an ac effective magnetic field suitable for high sensitivity measurement. (c) Measured PSD for different QWP angles with target beam power of 4mW. The dashed red curve is a sine fit to the data, the solid purple curve is the numerical simulation results, matching closely to the measurements. (d) Measured PSD as a function of incident power for $\theta = 3\pi/4$ showing a linear dependence. The dashed red curve is a linear fit. Insets show the raw measurement data for $|0\rangle \rightarrow | + 1\rangle$ (red) and $|0\rangle \rightarrow | - 1\rangle$ (blue) transitions. Panels (c) and (d) show that the effective field is directly proportional to PSD. 56
- 3.5 Effective static magnetic field sensed by an NV center near optical waveguides. Our rigorous simulations are performed using full wave analysis of the optical fields along with the light-matter interaction theory of Sec. 1. A plasmonic waveguide (a), a ridge waveguide (b), and an optical fiber (c) all producing transverse effective static magnetic fields due to the PSD of their evanescent fields. The direction of the effective static magnetic field is shown with black arrows and its amplitude with the colormap. The mode of the ridge waveguide is transverse electric (TE) and the mode of the optical fiber is \hat{x} polarized HE_{11} . 58
- 4.1 Interaction of the PSD of an optical beam with the electronic spin of NV centers. (a) Schematic of the measurements where a focused beam with elliptical polarization interacts with an ensemble of NV centers. (b) The Bloch sphere representation of the NV centers' electronic spin showing an induced rotation caused by the optical beam. The amount of this induced rotation depends on the PSD of the beam. The direction of the PSD and the bias magnetic field are aligned such that the induced rotation is equal for all NV centers in the ensemble. 61

- 4.2 Optimizing the coherence time of NV center ensemble. (a) The pulse sequence used for measuring Rabi oscillations and inhomogeneous broadening T_2^* for the ensemble. (b) The Hahn echo pulse sequence for measuring spin echo and coherence time T_2 . (c) Measurement results for the pulse sequences shown in (a) (blue dots) and (b) (purple circles). The Rabi oscillations show the shortest timescale, T_2^* . The inset shows the detail of this measurement. The red line is the envelope of the red curve from the the inset. The Hahn echo shows a slower decay due to elimination of inhomogeneous broadening and periodic revivals in the signal. The fits to the decay and revivals are shown with dashed blue and dotted green lines, respectively. The revivals are due to the periodic motion of the carbon-13 nuclear spins under the bias magnetic field. We use the second revival point ($\tau = 42\mu s$) for the effective static magnetic field measurements. 63
- 4.3 Incorporation of the PSD signal with the Hahn echo pulse sequence. (a) The PSD signal is added to the Hahn echo pulse sequence. Since this pulse sequence is only sensitive to ac magnetic fields, we add the PSD signal to one half of the sequence. Adding the PSD pulse to the first or second half induces rotations in opposite directions in the spin of the NV center which is similar to ac magnetic field with π phase difference. We extract the amplitude of the effective static magnetic field by subtracting the outcome of the two measurements. (b) Pulse sequence designed to measure the decoherence caused by the off-resonant absorption of the PSD signal. Here we add the PSD signal to both halves of the Hahn echo sequence to avoid spin rotations due to the effective static magnetic field. By increasing the pulse length τ we increase the probability of off-resonant absorption events in one measurement and observe the trend of the loss of the coherence signal. (c) The decoherence induced by the PSD signal for different PSD laser powers measured for $\lambda = 705nm$. In the case of complete decoherence the signal reaches half of the maximum contrast which is the average for the $|0\rangle$ and $|\pm 1\rangle$ states. 64
- 4.4 Scaling of the effective static magnetic field with beam power and polarization ellipticity. (a)-(c) Scaling of the effective field with the optical power of the PSD beam for different wavelengths. We observe linear dependence independent of the wavelength. (d)-(f) The dependence of the effective field on the ellipticity of polarization for different wavelengths. The ellipticity is controlled by rotating a QWP by an angle θ where $\theta = 0^\circ, 90^\circ$ correspond to linear polarization and $\theta = \pm 45^\circ, 135^\circ$ correspond to circular polarization. The fits to the curves are $y = \sin(2\theta)$ which is the expected dependence of PSD to QWP angle θ . We observe good agreement between theory and experiment for all wavelengths. 66

4.5	The dependence of the effective static magnetic field strength on the wavelength of the PSD beam. The rapid increase of field strength as the wavelength decreases shows a promising route for enhancing the effective static magnetic field. The inset in the top right corner shows the data in log scale along with the optical transition of the NV center at $\lambda = 637nm$. As the detuning decreases, the off-resonant absorption by the NV centers affects their coherence and the error bars become larger. To measure the data point at $\lambda = 705nm$ the sample is cooled to 30° below room temperature to lower the off-resonant absorption.	67
B.1	Schematic of energy levels of the NV center. Here, there are no external magnetic field and strain. Left and right panels show the possible transitions induced by left circularly polarized (LCP) and right circularly polarized (RCP) lights.	86
C.1	Transformation between the NV center coordinate frame and the off-resonant beam coordinate frame.	89
C.2	(a) The effective static magnetic field B_{eff} experienced by the qubit formed by $ - 1 \rangle$ and $ + 1 \rangle$ as a function of spin-spin-induced zero-field splitting ζ' and ζ'' . (b) The effective static magnetic field B_{eff} as a function of the external magnetic field B and the strain η_1 . Here, the other parameters are taken as $\lambda_z/2\pi = 5.5$ GHz, $\Delta_{es}/2\pi = 1.42/3$ GHz, the center wavelength of the right-handed circularly polarized excitation is $\lambda_0 = 800$ with laser power 1mW.	91
D.1	Schematic of the experimental setup. (a) Schematic of the setup showing the beam paths and filters. (b) Second-order correlation measurement showing that the AFM tip contains a single NV center. (c) Rabi oscillations showing the interaction of the microwave beam (MW) with the NV center. LP, linear polarizer; DM, dichroic mirror; BPF, band-pass filter; LPF, long-pass filter; SPF, short-pass filter; QWP, quarter-wave plate.	94
D.2	Instrument response function of the detection system. (a)-(b) Pictures of the experimental setup showing the key components. (c)-(d) The response function of the detection system for two different wavelengths covering the PL spectrum of NV center. The excitation signal is a femtosecond pulsed laser. (e)-(f) The spectra for the excitation signals used in panels (c) and (d) to measure the instrument response function.	96
F.1	Numerical simulations for the effective field amplitude in an AFM tip. (a) Amplitude of the electric field in an AFM tip made of diamond. (b) Amplitude and direction of the transverse component of the effective field in the plane of the NV center. (c) The effective field seen by an NV center with direction $\hat{n} = (\hat{x} + \hat{y} - \hat{z})/\sqrt{3}$ placed at various locations shown in panel (b) with white dots.	102

ABBREVIATIONS

AFM	atomic force microscopy
BPF	band-pass filter
DM	dichroic mirror
es	excited state
gs	ground state
IRF	instrument response function
LCP	left-handed circularly polarized
LP	linear polarizer
LPF	long-pass filter
MW	microwave
NV center	nitrogen-vacancy center
OAM	orbital angular momentum
ODMR	optically detected magnetic resonance
PDMR	photoelectric detection of magnetic resonance
PL	photoluminescence
PM	polarization maintaining
PSD	photonic spin density
QED	quantum electrodynamics
QWP	quarter-wave plate
RCP	right-handed circularly polarized
RO	readout
SAM	spin angular momentum
SPAD	single-photon avalanche diode
SPF	short-pass filter
TE	transverse electric
TIR	total internal reflection
TM	transverse magnetic
ZFS	zero-field splitting

ZPL zero-phonon line

ABSTRACT

Optical signals are a necessary tool for quantum technologies to carry information both for long-range and on-chip application. The scope of their use is determined by their ability to effectively interact with qubits. The deep-subwavelength interaction volume demands the understanding of the properties of optical fields in the near-field and light-matter interaction in this regime. Recent studies have unraveled the rich characteristics in the physical quantity known as the near-field photonic spin density (PSD). Photonic spin density is the spatial distribution of light's spin angular momentum. It is characterized by the degree of circular polarization of an optical field in deep-subwavelength volumes. In this thesis we study the properties of PSD in the near-field regime and demonstrate a platform for coherent light-spin-qubit interaction based on PSD. We show that nitrogen-vacancy (NV) centers in diamond can coherently interact with an optical beam where the interaction strength is determined by PSD in the nanoscale. To understand the near-field characteristics of PSD we study the evanescent waves and spin-momentum locking of light.

Evanescent electromagnetic waves possess spin-momentum locking, where the direction of propagation (momentum) is locked to the inherent polarization of the wave (transverse spin). We study the optical forces arising from this universal phenomenon and show that the fundamental origin of recently reported optical chiral forces is spin-momentum locking. For evanescent waves, we show that the direction of energy flow, direction of decay, and direction of spin follow a right hand rule for three different cases of total internal reflection, surface plasmon polaritons, and HE_{11} mode of an optical fiber. Furthermore, we explain how the recently reported phenomena of lateral optical force on chiral and achiral particles is caused by the transverse spin of the evanescent field and the spin-momentum locking phenomenon. Our work presents a unified view on spin-momentum locking and how it affects optical forces on chiral and achiral particles.

To probe the near-field properties of PSD, we propose and employ a single NV center in diamond as a nanoscale sensor. NV centers have emerged as promising room-temperature quantum sensors for probing condensed matter phenomena ranging from spin liquids, two-dimensional (2D) magnetic materials, and magnons to hydrodynamic flow of current. Here,

we demonstrate that the NV center in diamond can be used as a quantum sensor for detecting the photonic spin density. We exploit a single spin qubit on an atomic force microscope tip to probe the spinning field of an incident Gaussian light beam. The spinning field of light induces an effective static magnetic field in the single spin qubit probe. We perform room-temperature sensing using Bloch sphere operations driven by a microwave field (XY8 protocol). This nanoscale quantum magnetometer can measure the local polarization of light in ultra-sub-wavelength volumes. We also put forth a rigorous theory of the experimentally measured phase change using the NV center Hamiltonian and perturbation theory involving only virtual photon transitions.

In order to study the wavelength dependence of the optically induced magnetic field, we demonstrate this effect for an ensemble of NV centers. We characterize the wavelength dependence of the effective static magnetic field caused by the interaction of PSD and the spin qubit. We show that the strength of the field is inversely dependent on the detuning between the frequency of the optical beam and the optical transition of the NV centers. We show an optically induced rotation of over 10 degrees in the spin qubit of NV centers at room temperature. The direct detection of the photonic spin density at the nanoscale using NV centers in diamond opens interesting quantum metrological avenues for studying exotic phases of photons, nanoscale properties of structured light as well as future on-chip applications.

1. INTRODUCTION

Fundamental properties of particles such as linear and angular momentum govern their interactions with their environment. Optical beams also possess linear and angular momentum. Upon absorption or emission of light by particles these momenta are exchanged between photons and the particles along with the energy of the photons. These properties are well explained by the Poynting vector and Jones matrices in the far-field regime. However, these interaction phenomena show richer properties in the near-field that has come to light only recently. One reason is that probing the properties of optical fields in the near-field is challenging due to lack of universal probes in the nanoscale regime. These properties especially become more important as we move toward nanoscale photonic devices and circuits. Engineering the properties of optical fields in this regime is necessary to unlock the full potential of optical technologies.

Optical signals can be a suitable information carrier for on-chip quantum technologies. Understanding phenomena that govern the near-field properties of light leads to better tuning of its interaction with particles. This interaction can be based on absorption and emission of light by particles or coherent non-absorbing interactions. In order to study such applications it is crucial to introduce new platforms where coherent interaction of light and spin qubits in the near-field regime can be studied. In Chapter 3 we propose a room-temperature platform to experimentally study the near-field properties of light and its coherent interaction with a spin-qubit.

Nitrogen-vacancy (NV) centers are point defects in diamond lattice that have emerged as a powerful tool for probing nanoscale phenomena in condensed matter physics both at room temperature and cryogenic temperatures. NV centers have been extensively studied for their sensitivity to magnetic fields, electric fields, strain, and temperature. NV centers can be used in single NV configuration to achieve high resolutions or ensemble to increase the sensitivity of a measurement. In this thesis, we propose and demonstrate that they can be used to probe near-field properties of light such as photonic spin density at room temperature.

In this chapter, we first explore the properties of photonic spin density (PSD) and its non-trivial features in the near-field regime. Then we focus on the properties of NV centers

that make them suitable probes for nanoscale quantum sensing. This chapter serves as an introduction to the subsequent chapters. In the next chapter, we first investigate optical forces arising from spin-momentum locking in the evanescent optical fields. Then we introduce NV centers as a room-temperature platform for studying the PSD in the near-field regime and its interaction with spin qubits at room temperature.

1.1 Near-field Properties of Optical Fields

The polarization of optical fields governs many of their properties, such as the spin angular momentum carried by the field and their transmission through different media, as well as their interaction with particles [1], [2]. In the far-field limit the electric and magnetic field vectors lie in the plane transverse to the direction of the propagation of the beam. This is not the case in the near-field which gives rise to non-trivial phenomena in this regime. Wang and Chan [3] have shown that if a chiral particle is placed near a surface it can experience an optical force perpendicular to the direction of the momentum of the incident beam. Mitsch *et al.* [4] show that the directionality of the coupling of light scattered from a nanoparticle into an optical waveguide can be controlled by changing the handedness of the polarization of the incident beam. These seemingly unrelated examples along with other similar works [5]–[15] can be unified in theory by studying the properties of optical fields in the near-field regime.

We start with an illustrative example to contrast the properties of spin density for propagating plane waves and decaying evanescent waves. Exploring the characteristics of the optical fields in the near-field reveals an intrinsic component of the photonic spin density in the evanescent waves (Fig. 1.1). The spin density here is defined as $\vec{S}^{\text{obs}} = \epsilon \vec{\mathcal{E}}_{\perp}(\vec{r}, t) \times \vec{A}_{\perp}(\vec{r}, t)$ where $\vec{\mathcal{E}}(\vec{r}, t)$ is the electric field, $\vec{A}(\vec{r}, t)$ is the vector potential, the subindex \perp denotes the transverse part of the vector field, and ϵ is the permittivity [16], [17]. For a monochromatic wave propagating in the free space the spin density is time independent and can be written as [18]–[20]

$$\vec{S}^{\text{obs}} = (1/4\omega) \text{Im} \left[\epsilon_0 \vec{E}^* \times \vec{E} + \mu_0 \vec{H}^* \times \vec{H} \right] = \vec{S}_E^{\text{obs}} + \vec{S}_M^{\text{obs}}, \quad (1.1)$$

where \vec{S}_E^{obs} and \vec{S}_M^{obs} are the electric and magnetic spin densities, respectively.

For a plane wave propagating along \hat{z} in free space with complex electromagnetic fields

$$\vec{E} = E_0[\cos(\theta)\hat{x} + i\sin(\theta)\hat{y}]e^{ik_0z} \quad (1.2)$$

and

$$\vec{H} = \sqrt{\epsilon_0/\mu_0}E_0[-i\sin(\theta)\hat{x} + \cos(\theta)\hat{y}]e^{ik_0z}, \quad (1.3)$$

the spin densities are

$$\vec{S}^{\text{obs}} = 2\vec{S}_E^{\text{obs}} = 2\vec{S}_M^{\text{obs}} = [\epsilon_0\sin(2\theta)/\omega]|E_0|^2\hat{z}. \quad (1.4)$$

Here k_0 is the free-space wavenumber and θ is an arbitrary angle where $\theta = \pm\pi/4$ corresponds to left- and right-handed circularly polarized beams and $\theta = 0, \pi/2$ corresponds to \hat{x} and \hat{y} linearly polarized beam. This shows that the spin density for a plane wave is always along the direction of propagation and its amplitude is maximum for a circularly polarized beam and zero for a linearly polarized beam.

On the other hand, for an evanescent beam propagating in \hat{z} direction and decaying in \hat{y} direction ($\vec{k} = \kappa\hat{z} + i\eta\hat{y}$, $\kappa^2 - \eta^2 = k_0^2$) the complex electromagnetic fields are

$$\vec{E} = E_0[\cos(\theta)\hat{x} + i\sin(\theta)(\kappa\hat{y} - i\eta\hat{z})/k_0]e^{i\vec{k}\cdot\vec{r}} \quad (1.5)$$

and

$$\vec{H} = \sqrt{\epsilon_0/\mu_0}E_0[-i\sin(\theta)\hat{x} + \cos(\theta)(\kappa\hat{y} - i\eta\hat{z})/k_0]e^{i\vec{k}\cdot\vec{r}}. \quad (1.6)$$

The spin density for this wave is

$$\vec{S}^{\text{obs}} = (\epsilon_0/4\omega)[-(2\kappa\eta/k_0^2)\hat{x} + \sin(2\theta)(\kappa/k_0)\hat{z}]|E_0|^2e^{-2\eta y}. \quad (1.7)$$

In contrast to the propagating plane wave, the evanescent wave has a component of spin density perpendicular to the direction of propagation and decay. This component is independent of the polarization of the beam (determined by m). This phenomenon known as

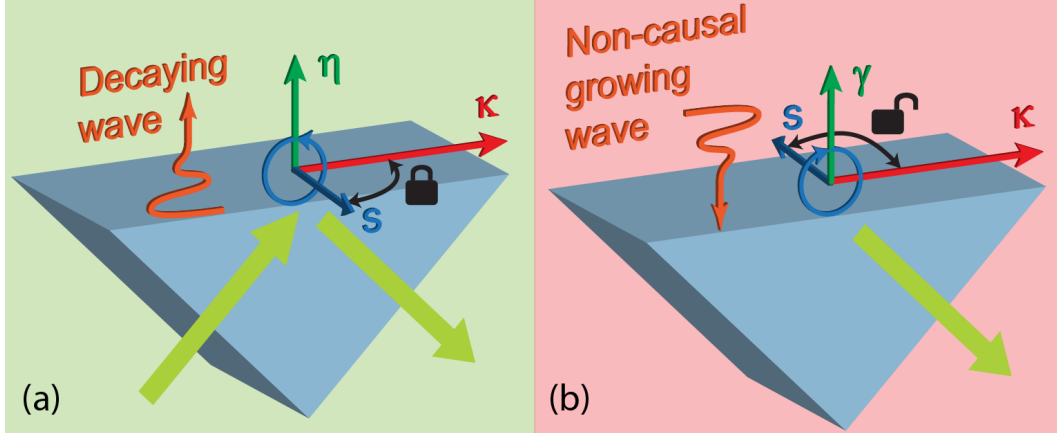


Figure 1.1. Spin-momentum locking in total internal reflection (TIR). (a) A propagating plane wave enters the prism beyond the critical angle and an evanescent wave appears on the opposing side. A component of PSD transverse to the direction of propagation exist in the evanescent wave. The direction of this component is locked to the direction of propagation (κ) and direction of decay (η). (b) The direction of decay is set by the boundary and a growing wave away from the boundary violates causality. In order to generate a transverse spin density in the opposite direction compared to panel (a) the direction of propagation has to change.

spin-momentum locking of evanescent waves is discussed in more detail in the next subsection.

1.1.1 Spin-momentum locking in evanescent fields

Bliokh *et al.* [18] and Mechelen and Jacob [21] showed that for evanescent waves there is an intrinsic component of spin that is transverse to the direction of propagation of the beam. This component forms a right-handed triplet with the momentum vector and the decay vector. Figure 1.1 shows this effect in total internal reflection from an air/dielectric interface. Here the evanescent wave has a transverse component of photonic spin density that is determined by the direction of propagation of the incident beam. This phenomenon is called spin-momentum locking for evanescent waves and it is universal to all structures that produce evanescent fields.

The spin-momentum locking phenomenon is also present in the evanescent field generated near optical waveguides. Figure 1.2 shows this effect for a ridge waveguide where the

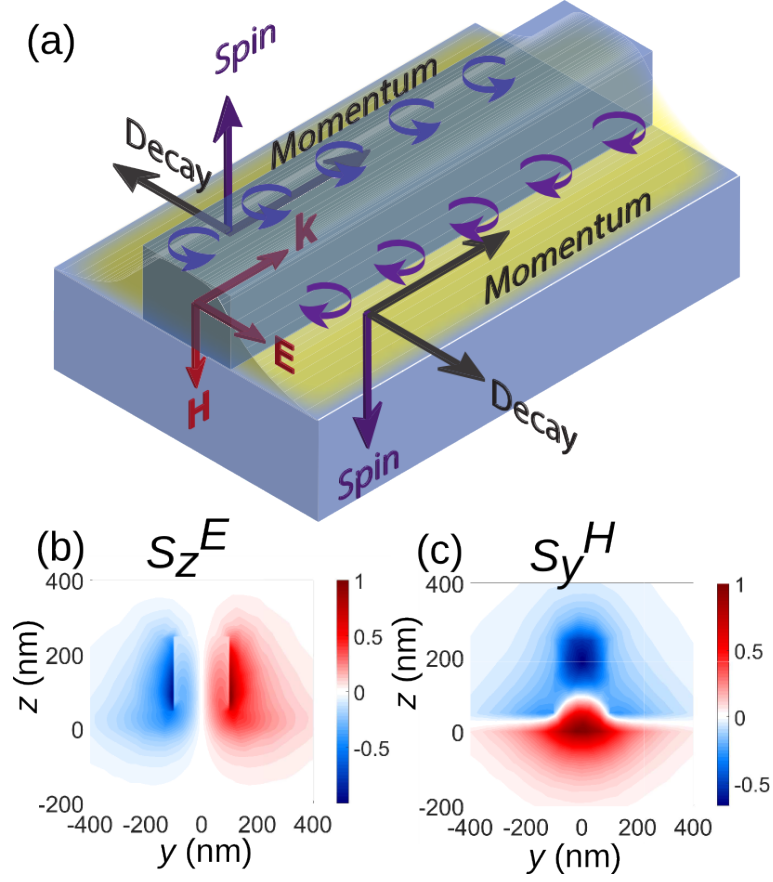


Figure 1.2. Spin-momentum locking in an optical waveguide. Reprinted with permission from [15]. (a) Schematic of a ridge waveguide with the PSD near the waveguide for a TE-like mode. (b) Electric component of PSD in the vicinity of the waveguide showing the dependence on the direction of decay. The PSD has opposite direction on the two sides of the waveguide following the spin-momentum locking phenomenon. (c) Same as (b) for the magnetic component of PSD. The magnetic component has higher intensity above and below the waveguide due to the direction of the magnetic field in the optical mode.

direction of PSD is locked to the direction of propagation of the beam inside the waveguide. Figure 1.2(b) and 1.2(c) show the electric and magnetic components of the PSD in the vicinity of the waveguide. These panels show the effect of the polarization of the optical mode on the spatial distribution of the electric and magnetic components of PSD. However, the direction of the transverse spin density is governed by the spin-momentum locking phenomenon.

1.1.2 Spin based directional coupling of light into guided modes

The phenomenon of directional coupling is shown in Fig. 1.3. This figure shows an spinning dipole radiating next to a metallic (silver) or dielectric ($\epsilon_r = 2$) surface. The dipole couples to the high-k modes of the dielectric media and the plasmonic modes of the silver layer with a preferred direction depending on the direction of its spin. This directional coupling is related to the PSD of the high-k modes in the dielectric and the surface plasmon polariton modes in the silver layer as illustrated in Fig. 1.1. However, if the dipole is radiating between two surfaces where the structure is symmetric the directional coupling is suppressed in both layers (panels (d)-(f)). This is due to the existence of both the growing and decaying evanescent waves in the gap between the two layers in contrast to the top panels where only a decaying wave can be present in the vacuum.

This phenomenon is demonstrated in different platforms such as optical waveguides, cavities, surface plasmon polariton modes, and metamaterials [4], [6]–[8], [12], [13], [22], [23]. The directional coupling allows for development of on chip spin-based interfaces and novel applications such as optical diodes [24].

1.1.3 Novel applications based on near-field photonic spin density

Exploring the properties of PSD in the near-field has given rise to new applications in nanophotonics. Exotic phenomena such as topologically non-trivial spin textures (Figs. 1.4(b) and 1.4(c)) have been reported in the near-field arising from interaction of light with electronic excitations as well as interference of optical beams [25]–[27]. The spin texture in these excitations have deep-subwavelength features that can be used for super-resolution imaging. Moreover, the near-field spin density can be utilized to create non-reciprocal devices. Figure 1.4(d) shows such a device where cold atoms are trapped near an optical nanofiber to make a non-reciprocal device. The nanofiber only allows transmission in one direction depending on the externally controlled spin-polarization of the trapped atoms.

The near-field spin density of the optical modes can also be utilized to control the interaction between two optical modes [28], [30], [31]. Figure 1.4(e) shows an optical nanofiber interacting with the whispering gallery modes of a microcavity. The near-field PSD of each

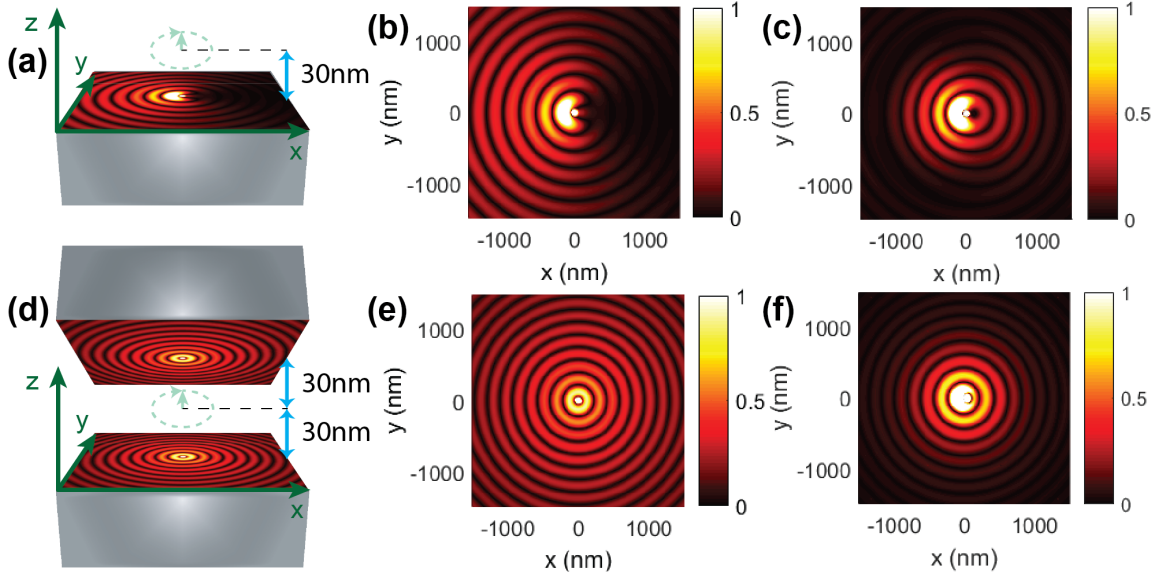


Figure 1.3. Demonstration of the spin-momentum locking phenomenon for a spinning dipole coupling to SPP modes and high-k modes of a dielectric medium. (a)-(c) A spinning dipole is placed near the surface of a silver film ((a) and (b)) and a dielectric surface ((c), $\epsilon = 2$). The radiation from the dipole couples to the modes of these surfaces in a preferential direction determined by the spinning direction of the dipole. This directional coupling arises from the matching between the spinning direction of the dipole and the spinning fields (PSD) of the optical mode. (d)-(f) The same dipole radiating between two symmetric interfaces. The directional coupling disappears due to the added symmetry to the system. The additional layer allows for decaying waves in both directions, suppressing the directional coupling effect. The corresponding E_z component of the electric field on the $z = 0$ plane is plotted in all panels. The amplitude of the dipole is $\mathbf{p} = p_0(3i\hat{\mathbf{x}} + \hat{\mathbf{z}})$ and has a wavelength of $\lambda = 500$ nm.

mode of the fiber can determine which modes of the microcavity are excited which gives rise to different response of the system. In addition, the near-field PSD can govern the direction of coupling of emitted light from quantum dots into a waveguide or cavity [13], [29]. This is shown in Fig 1.4(f) where a quantum dot emits light into a cavity based on its spin-state.

The phenomenon of spin-momentum locking is studied in detail in Chapter 2. In Chapter 2 we establish a connection between the phenomena of directional coupling, transverse optical forces on chiral particles and spin-momentum locking for evanescent waves. We study

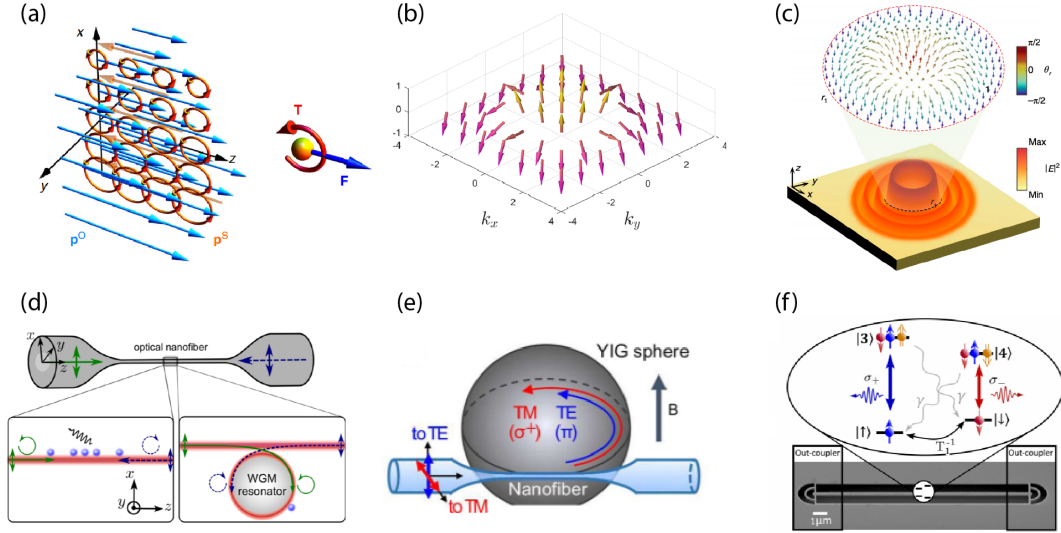


Figure 1.4. Utilizing PSD in the near-field unlocks novel applications. (a) Schematic of photonic spin and momentum transverse to the direction of propagation of a beam for an evanescent wave. Reprinted with permission from [18]. (b) Spin-texture in the momentum space showing a topologically nontrivial state. Reprinted with permission from [26]. (c) Formation of an optical skyrmion when an optical beam interacts with a SPP mode. Reprinted with permission from [25]. (d) Nonreciprocal waveguide using a tapered optical fiber and spin-polarized atoms trapped next to the optical fiber. The interaction between the spin-polarized atoms and the spin of the optical beam only allows for transmission in one direction determined by spin-momentum locking for evanescent waves. Reprinted with permission from [24]. (e) Polarization dependent response in a YIG microcavity. The different transverse spin of the two polarizations traveling in a nanofiber excites different modes of a cavity resulting in a polarization dependent response. Reprinted with permission from [28]. (f) Photonic-spin based interface between a quantum dot and a waveguide. The interaction between the spin of the quantum dot and the spin of the optical mode of a waveguide determines the direction of coupling of light into the waveguide. Reprinted with permission from [29].

the optical forces exerted on chiral and achiral particles in evanescent fields and show the phenomenon of spin-momentum locked optical forces.

1.2 Nitrogen-vacancy Centers in Diamonds

NV centers are color centers in diamond consisting of a substitutional nitrogen atom next to a vacancy cite (Fig. 1.5). These defects have long coherence time at room temperature

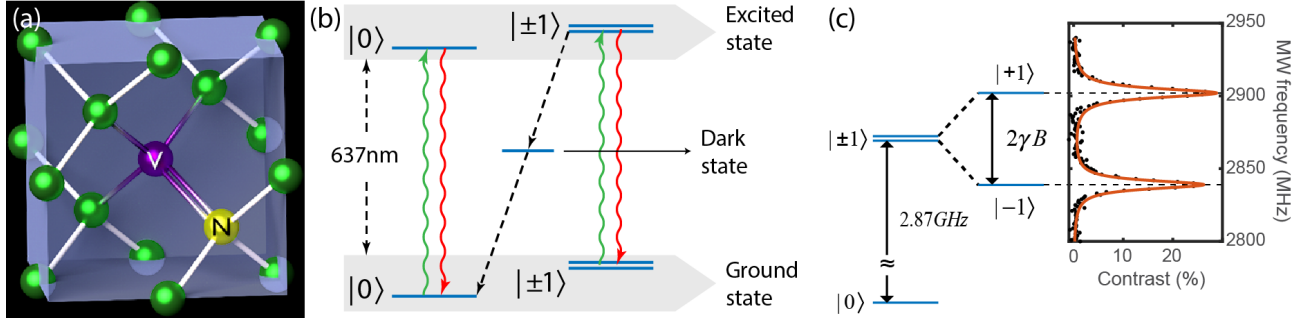


Figure 1.5. Atomic structure and energy levels of NV center. (a) NV center consists of a substitutional nitrogen atom next a vacancy defect. (b) Simplified energy levels and transitions of NV center showing a 637nm optical transition between the ground and excited states. The ground and excited states are both spin triplets. The transition through the dark state is spin-flipping and allows for optical polarization and readout of the NV center’s spin state. (c) Ground state energy levels of NV center showing the zero-field splitting and Zeeman splitting between $|\pm 1\rangle$ states due to an applied magnetic field. An optically detected magnetic resonance (ODMR) measurement can reveal the resonance gaps between the $|0\rangle$ and $|\pm 1\rangle$ states.

and high sensitivity to magnetic fields. Due to their atomic size, NV centers have been utilized to probe nanoscale phenomena in the condensed matter physics (Fig. 1.6) such as probing spin waves [32], probing magnetism in 2D materials [33], probing Johnson noise [34], and mapping skyrmionic fields [35].

1.2.1 Electronic structure of NV centers

NV center can appear in two different charge states—negatively charged and neutral [36]. In this thesis we refer to the negatively charged state as NV center. Figure 1.5(b) shows a simplified energy level of NV center in the negatively charged state that gives rise to its optical properties that allow it to be a quantum sensor suitable for many applications. The ground and excited state of NV center are both spin triplets. The dark state is a singlet state which has a much longer lifetime ($\tau > 150\text{ns}$) compared to the excited state ($\tau = 12 - 25\text{ns}$) [36]. The emission spectrum features a zero-phonon line (ZPL) at $\lambda = 637\text{nm}$ and a phonon sideband extending from $\lambda = 640\text{nm}$ to $\lambda = 780\text{nm}$ [37]–[39].

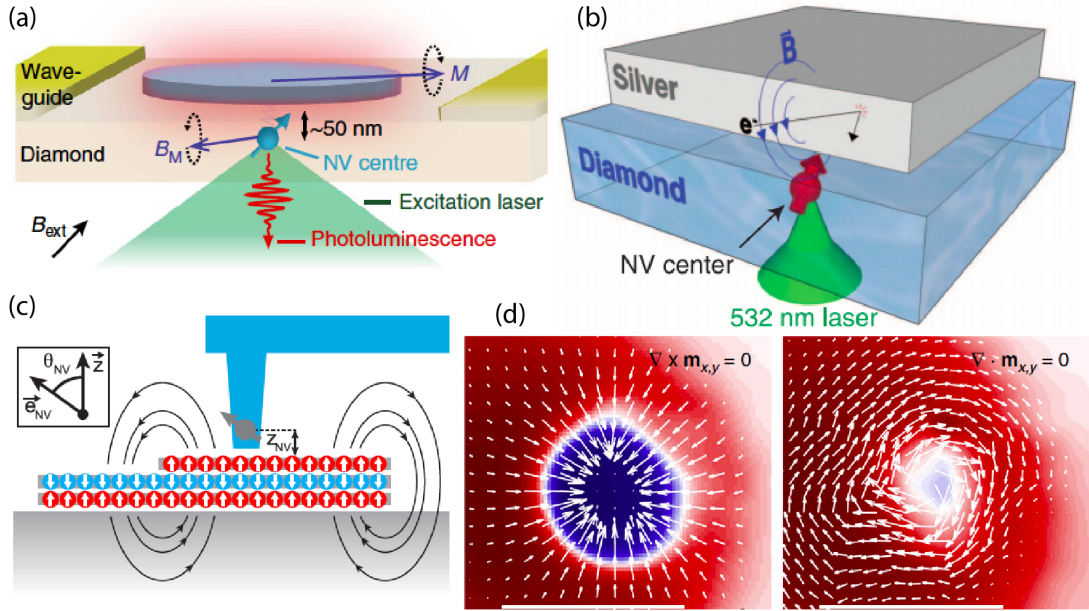


Figure 1.6. Quantum sensing with NV centers. (a) NV centers in diamond are used to probe magnetic excitations in a ferromagnetic microdisk. Reprinted with permission from [32]. (b) Single NV centers in diamond are used to probe the thermally induced magnetic noise in the vicinity of a silver film. The noise reduces the coherence time of the NV center. Reprinted with permission from [34]. (c) An NV center is used to scan the magnetic field generated near a flake of CrI₃ with nanometer resolution. Reprinted with permission from [33]. (d) An NV center is used to generate a map of the magnetic field produced by an skyrmion at room temperature. Reprinted with permission from [35].

The ground state of the NV center has a zero-field splitting gap $\Delta_{gs} = 2.87\text{GHz}$ between the $|0\rangle$ state and $|\pm 1\rangle$ states (Fig. 1.5(c)). The degeneracy between the $|\pm 1\rangle$ states can be broken by applying a magnetic field along the axis of the NV center. Most applications use only two of the energy levels in the ground state ($|0\rangle$ and $|+1\rangle$ or $|0\rangle$ and $|-1\rangle$) as a two level quantum system. The two levels can be selected by tuning the frequency of a microwave excitation to the gap between the desired energy levels.

1.2.2 Polarization and readout

The optical excitation/relaxation cycle in NV center is spin preserving. However, an intersystem crossing through the dark state allows a spin-flip from $|0\rangle$ state to $|\pm 1\rangle$ states.

The probability of this spin-flip is higher if the NV center is in spin ± 1 states ($\frac{P_{|\pm 1\rangle \rightarrow |0\rangle}}{P_{|0\rangle \rightarrow |\pm 1\rangle}} \approx 4$) [40], [41]. This effect allows for optical polarization of NV center spin state. If the NV center is illuminated by an optical excitation, after a number of excitation/relaxation cycles the NV center is polarized in spin $|0\rangle$ state. The purity of this polarization can exceed 80% [41].

The other key property of the NV center is the possibility of optical readout of its spin state. The dark state has a longer lifetime compared to the excited state of the NV center. Therefore, when the NV center decays into the dark state the photoluminescence (PL) probability decreases. Since the $|\pm 1\rangle$ states have a higher probability of decaying into the dark state, the PL probability is lower for these states compared to the $|0\rangle$ state. We define a contrast to measure this change in the PL of an NV center

$$Contrast = \frac{I_{|0\rangle} - I_{meas}}{I_{|0\rangle}} \quad (1.8)$$

where $I_{|0\rangle}$ is the PL intensity for the $|0\rangle$ state and is the highest achievable PL intensity, and I_{meas} is the PL intensity for an unknown state. The contrast is zero for an NV center in $|0\rangle$ state and maximum for an NV center in $|\pm 1\rangle$ states. Therefore, we can optically read out the spin state of an NV center. We first characterize the contrast for the $|\pm 1\rangle$ states and compare it to the PL intensity of an unknown state.

The change in contrast is shown in Fig. 1.5 where a microwave excitation is tuned into the two resonance energies between $|0\rangle$ and $|\pm 1\rangle$ sublevels. When the microwave excitation is resonant to one of the transitions, the NV center spin state couples from $|0\rangle$ state to $|\pm 1\rangle$ states. This leads to a reduction in the PL of the NV center and therefore an increase in the contrast.

Alternative readout techniques have been demonstrated for NV centers [42]–[45]. Most of the proposed methods take advantage of charge state conversion of NV centers to perform the readout. Charge state conversion is the transformation of a negatively charged NV center to a neutral charge state through photoionization [46]–[50]. However, photoelectric detection of magnetic resonance (PDMR) and laser threshold readout have been demonstrated as well [51], [52].

1.2.3 Coherent manipulation of spin-states

An NV center can be optically polarized only into the $|0\rangle$ state. To prepare the NV center in $|\pm 1\rangle$ states or a mixed state we use a MW signal. When the MW signal is resonant to $|0\rangle \rightarrow |-1\rangle$ or $|0\rangle \rightarrow |+1\rangle$ transitions, the spin-state coherently oscillates between the two states. This behavior is known as Rabi oscillations and can be measured using the pulse sequence shown in Fig. 4.2(a). The inset of Fig. 4.2(c) and Fig. D.1(c) show Rabi oscillations for an ensemble and a single NV center, respectively.

Measuring the Rabi oscillations allows us to determine the MW pulse-lengths required for performing dynamical decoupling and ac magnetometry. The period of Rabi oscillations determines a full cycle of the spin-state changing from $|0\rangle$ to $|\pm 1\rangle$ and back to $|0\rangle$. Therefore, if the spin-state is optically polarized into $|0\rangle$ state, to polarize it into $|\pm 1\rangle$ states we apply a MW pulse with a width equal to half of the Rabi cycle (π -pulse). Similarly, to change the spin-state to a superposition of $|0\rangle$ and $|\pm 1\rangle$ states we apply a pulse with a width equal to a quarter of a Rabi cycle ($\pi/2$ -pulse). The Rabi oscillations can be visualized by rotations on the Bloch sphere. Changing the phase of the MW pulse allows us to determine the axis of this rotation.

The readout of an unknown spin-state reveals the population of NV centers in each state for an ensemble or the probability of finding an NV center in each of the states for a single NV center. If the population is fully in $|0\rangle$ state the readout contrast is equal to zero and if the population is fully in $|\pm 1\rangle$ states the readout signal is maximum. On the Bloch sphere, the readout signal is related to the projection of the spin-vector on the z axis. The interaction of an external magnetic field or PSD induced effective field with an NV center only changes the phase between the $|0\rangle$ and $|\pm 1\rangle$ states and leaves the populations unchanged. A change in the phase between the states is equivalent to a rotation of the spin-vector in the $x - y$ plane on the Bloch sphere. We use the MW induced rotations to project an acquired phase onto the z axis before the readout is performed (see Fig. 3.3(b)-(f)).

1.2.4 Coherence time and dynamical decoupling

Sensitivity of NV center measurements are limited by the spin relaxation time and dephasing time of the NV center. Spin relaxation time (T_1) determines the characteristic time for transitions between the ground state sublevels to occur and reaches a few milliseconds at room temperature. These transitions lead to thermalization of the population between the triplet state sublevels. The spin relaxation time is sensitive to magnetic noise in the environment and can be used to probe this noise [34].

On the other hand magnetic fluctuations in the environment can lead to homogeneous dephasing in the NV center spin state as well. The dominant source of these fluctuations in diamond crystal is carbon-13 atoms. Carbon-13 is a stable isotope of carbon that has a 1.1% natural abundance. The homogeneous dephasing time (T_2) is limited to 100us at room temperature. However, in isotopically engineered diamond this dephasing time can exceed $T_2 = 1ms$ [53].

The coherence time of NV center can be limited by inhomogeneous dephasing both for ensemble of NV centers and single NV center measurements. In the case of an ensemble of NV center the inhomogeneous dephasing arises from each NV centers being affected by a different local magnetic noise. For single NV center measurement this dephasing comes from the inhomogeneity of the noise over many repetitions of the measurement in contrast to the homogeneous dephasing where only a single measurement is of concern. The inhomogeneous dephasing time is limited to $T_2^* \approx 1\mu s$ for diamond crystals with natural abundance of carbon-13 atoms. The T_2^* time can be revealed by Rabi oscillation measurements (shown in D.1(c) for single NV center and 3.2(c) for an ensemble of NV centers) or Ramsey interferometry [54]–[56].

To avoid the effect of inhomogeneous dephasing we take advantage of the nature of magnetic noise in diamond. The dominant source of magnetic noise is the nuclear spins in the lattice. This includes the carbon-13 atoms as well as nitrogen impurities. The characteristic time dynamics of nuclear spins is much smaller than that of electronic spin of the NV centers. The gyromagnetic ratio for carbon-13 atoms is $\gamma_{13C} = 10.7\text{KHz/mT}$ in comparison to $\gamma_{NV} = 28\text{MHz/mT}$ for NV center electronic spin. This means while over repeating measurements

on a single NV center the ambient noise fluctuates, during a single measurement the noise is only slowly varying. We use this feature to eliminate the effect of the inhomogeneous dephasing by dynamically decoupling the NV center’s electronic spin from the slowly varying background noise. The simplest form of dynamical decoupling is spin echo [57], [58]. In these techniques periodic rotation of the spin of the NV center prevents it from interacting with a dc field. As a result of this only magnetic fields that oscillate at the same frequency with the dynamical decoupling rotations can effectively interact with the spin qubit. Therefore, these techniques cannot be combined with dc magnetometry technique to improve the sensitivity of the system. If the time-scale of these rotations is much shorter than that of the variations in the background noise, the effect of the noise on the dephasing of the qubit will be reduced. Different pulse sequences have been implemented for increasing the coherence time of NV centers [58], [59]. In our work we employ the XY8 technique for single NV center in Chapter 3 and Hahn echo technique for an ensemble of NV center in Chapter 4 to achieve the highest sensitivity with each system.

1.2.5 Fabrication of NV centers

Diamonds containing NV centers can be made in many different forms. Bulk diamond NV centers and NV centers in nanodiamond are two main categories. Nanodiamond containing NV centers are available in different sizes from a few nanometers to hundreds of nanometers and can contain a single NV center or an ensemble of NV centers. This allows for high resolution sensing as well as high sensitivity measurement by choosing the proper nanodiamond. These nanodiamonds are useful for spin-coating on different surfaces or using with biological samples for magnetic field measurements or temperature sensing [60]–[63].

The NV centers can also be found naturally or synthetically produced in bulk diamond. The nitrogen impurities in diamond crystal can be introduced during the fabrication of diamond or after fabrication through ion implantation [64], [65]. The creation efficiency of the NV centers is improved by electron irradiation and annealing after fabrication and ion implantation of the nitrogen impurities [66]–[68]. The annealing temperature and time determines the quality of the NV centers created in this method [69], [70].

The ion implantation technique allows for precise control over the location and depth of NV center [66], [71]. The implanted NV centers can be as close as 5nm to the surface of the diamond which allows for high resolution sensing of the environment next to the diamond. The coherence time of the shallow NV centers, however, is affected by the surface which limits the distance to the surface [72]–[77].

1.3 Layout of the Thesis

The major achievement of the thesis is the merger of the fields of research related to photonic spin density and quantum magnetometry using NV centers in diamond.

Chapter 2 will explore the optical forces arising from the PSD in the presence of evanescent waves on both chiral and achiral particles. Moreover, we connect the different phenomena that have been observed in the presence of evanescent optical fields such as unidirectional coupling and transverse optical forces using the principle of spin-momentum locking for evanescent waves. We show that the photonic spin, momentum, and decay direction form a right-handed triplet in the presence of evanescent fields. This chapter presents theoretical work that combines the Maxwell stress tensor formalism with photonic spin density to analyze optical forces. Measurement of such predicted forces will be possible in the future using optically trapped nanoparticles.

Even though there have been recent indirect demonstrations of PSD using 2D materials, quantum dots and their directional spontaneous emission, an open question for the field is direct measurement of the PSD. We propose and demonstrate a nanoscale probe for PSD in Chapter 3—NV centers in diamond acting as room temperature quantum magnetometers. We demonstrate that the NV center in diamond can coherently interact with an optical beam at room temperature. We utilize this interaction to probe PSD of an optical beam. This platform allows for study of spin-based interactions between light and a spin-qubit in the presence of evanescent fields due to the nanometer size of an NV center. We further explore the paths to enhancing this interaction in order to enable all-optical coherent control of spin-qubits.

There are two widely utilized NV center systems in the community - one based on nanodiamond and the other based on bulk diamond. The nanodiamond system on an AFM tip is used widely for scanning magnetometry of quantum materials as well as for temperature measurements inside cells. On the other hand, bulk diamond nanobeams and resonators with NV centers have been utilized for integrated quantum photonics applications. In the final chapter, we show that circularly polarized light can induce an effective static magnetic field in NV centers in bulk diamond. The distinct advantage of this platform compared to the nanodiamond on the AFM tip employed in Chapter 3 is the reduced scattering and perturbation of the transverse field profile of in-coupled light. A detailed wavelength dependent study is made possible by this new configuration since the power density at the location of the NV center can be controlled to be constant.

Both experimental set-ups utilized to obtain the results in the final two chapters were developed entirely from the ground up specifically for this thesis. This includes the single photon level read-out optics, second order photon correlation set-up and microwave antenna based qubit driving system. The work in this thesis can lay the foundations for the development of future on-chip spin photonic applications and quantum technologies.

2. UNIVERSAL SPIN-MOMENTUM LOCKED OPTICAL FORCES

Evanescent electromagnetic waves possess a unique intrinsic property of spin-momentum locking where the direction of phase propagation, which can be associated with momentum, is locked to the direction of an intrinsic polarization [18], [78]–[80]. The similarities with surface states of electronic topological insulators led to the coining of the term - quantum spin Hall effect of light [81], [82]. However, it should be emphasized that the evanescent surface electromagnetic waves on conventional media are not symmetry protected and the analogy is limited only to spin-momentum locking [79]. This intrinsic polarization of evanescent waves can be associated with a spin-density vector which is transverse to both the direction of its momentum and the direction of decay [79], [81]. The evanescent waves also transfer the spin-momentum locking to bulk modes through electromagnetic boundary conditions [79]. The phenomenon of spin-momentum locking of light has been observed in a variety of systems including optical fibers, surface plasmon-polaritons and photonic crystal waveguides [4], [6], [8], [9], [12], [13], [22], [83]–[85]. A unifying theme in these experiments is that scattered or spontaneously emitted light with an intrinsic polarization shows unidirectional propagation.

It is an interesting question whether this intrinsic polarization of the evanescent wave (transverse spin) can lead to optical forces and whether they show fundamental behavior different from well-known gradient and radiation pressure forces [86], [87]. Very recent studies involving optical forces on chiral particles, which contain both induced electric and magnetic moments, show that these particles can experience an optical force perpendicular to the direction of the momentum of the incident field [3], [5], [10]. It was recently shown that the particle in the unidirectional coupling experiment also experiences an anomalous optical force perpendicular to the direction of the momentum of the incident beam [11]. These anomalous forces cannot be explained by the gradient or radiation pressure forces.

2.1 Outline of the Problem

In this chapter we present a unified view of anomalous optical forces on chiral and achi-ral particles and uncover the fundamental connection to the spin-momentum locking phe-nomenon associated with evanescent waves. This force is different in nature from the gradient force or the optical pressure and is in fact related to the transverse spin of evanescent electro-magnetic fields interacting with the particle. We make the important observation that there exists a fundamental right-handed triplet vector for evanescent waves related to momentum, decay and transverse spin which governs the direction of optical forces. The spin-density forces are rigorously calculated using a stress tensor formalism for evanescent waves gen-erated during total internal reflection (TIR) and the near-field of an optical fiber. Subtle connections between spin-momentum locking and the non-trivial direction of the spin forces are revealed paving the way for experimental demonstrations. Our work also shows clearly the independence of the orbital angular momentum (OAM) of the propagating optical fiber mode and the transverse spin-density of the evanescent waves associated with the near-field.

2.2 Spin Density and Transverse Spin in Evanescent Waves

We start with a discussion of the field quantities defining the intrinsic spin density of elec-tromagnetic evanescent waves. This is a subtle question and can only be answered by making connections to experimental observables such as energy and optical forces. Momentum den-sity of electromagnetic waves is proportional to the Poynting vector [82], $\langle \vec{p} \rangle = \langle \vec{N} \rangle / c^2$, where $\langle \vec{p} \rangle$ is the time-averaged momentum density, $\langle \vec{N} \rangle = 1/2 \text{Re}[\vec{E} \times \vec{H}^*]$ is the time-averaged Poynting vector, and c is the speed of light. For evanescent waves, the direction of this momentum is always perpendicular to the direction of decay and is the same as the direction of the real part of the wave vector [79]. The spin density of evanescent waves has been defined by [18], [19], [88], $\vec{S}^{\text{obs}} = \langle \vec{s} \rangle = (1/4\omega) \text{Im}[\epsilon_0 \vec{E}^* \times \vec{E} + \mu_0 \vec{H}^* \times \vec{H}] = \vec{S}_E^{\text{obs}} + \vec{S}_M^{\text{obs}}$, where \vec{S}_E^{obs} and \vec{S}_M^{obs} are the electric and magnetic spin densities, respectively. Another equivalent approach is to define the electric and magnetic spin densities by introducing the generalized electric and magnetic Stokes parameters (see Appendix A), $\vec{S}_E^{\text{obs}} = \vec{V}^e / (\omega c)$ and $\vec{S}_M^{\text{obs}} = \vec{V}^m / (\omega c)$.

In Fig. 2.1 the direction of the component of the spin density transverse to the plane of momentum and decay direction is shown for three different cases. This figure illustrates that the triplet of momentum, decay direction and transverse spin follows a right-hand rule. This means for a beam propagating in $+\hat{z}$ direction if the wave is decaying in $+\hat{x}$ direction the transverse spin will be in $+\hat{y}$ direction. We emphasize the subtle observation that the opposite direction of the transverse spin is inconsistent with causality because it refers to a wave growing in magnitude away from the boundaries.

2.3 Anomalous Optical Force and Directional Coupling

Spin-momentum locking has profound consequences on optical forces. Optical force acting on a chiral particle in an incident electromagnetic field, with induced dipole moments $\begin{bmatrix} \vec{p} \\ \vec{m} \end{bmatrix} = \begin{bmatrix} \alpha_{ee} & i\alpha_{em} \\ -i\alpha_{em} & \alpha_{mm} \end{bmatrix} \begin{bmatrix} \vec{E} \\ \vec{H} \end{bmatrix}$, can be expressed as (see Appendix A) $\langle \vec{F} \rangle = \langle \vec{F}_{gr} \rangle + \langle \vec{F}_{op} \rangle + \langle \vec{F}_{sr} \rangle$ where all the forces are time averaged. $\langle \vec{F}_{gr} \rangle$ and $\langle \vec{F}_{op} \rangle$ are the gradient force and radiation pressure, respectively. $\langle \vec{F}_{sr} \rangle = -(ck_0^4/6\pi) \left\{ \left(\text{Re}[\alpha_{ee}\alpha_{mm}^*] + |\alpha_{em}|^2 \right) \langle \vec{N} \rangle + \sqrt{\mu_0/\epsilon_0} \text{Re}[\alpha_{ee}\alpha_{em}^*] \vec{V}^e + \sqrt{\epsilon_0/\mu_0} \text{Re}[\alpha_{mm}\alpha_{em}^*] \vec{V}^m - 1/2 \text{Im}[\alpha_{ee}\alpha_{mm}^*] \text{Im}[\vec{E} \times \vec{H}^*] \right\}$ is the scattering recoil force. It vanishes for an achiral particle with no magnetic polarizability. In the case of a chiral particle, this force has two terms proportional to the electric and magnetic fourth Stokes parameters (or equivalently electric and magnetic spin densities). The sum of these two terms is known as the spin density force. Therefore, the spin density force is a part of the overall scattering recoil force. Our aim is to show that the subtle phenomenon of spin-momentum locking dictates the non-trivial direction of this force in various scenarios where nanoparticles are interacting with evanescent waves.

We first consider the phenomenon of total internal reflection at a dielectric-air interface with a nanoparticle placed on the air side as shown in Fig. 2.2. The evanescent waves generated have the same direction of propagation parallel to the interface as the incident beam i.e. their momentum is fixed. This immediately fixes the transverse spin direction of the evanescent wave by the spin-momentum locking phenomenon. Consequently, light scattered by chiral and achiral particles will show fundamentally different behavior since the

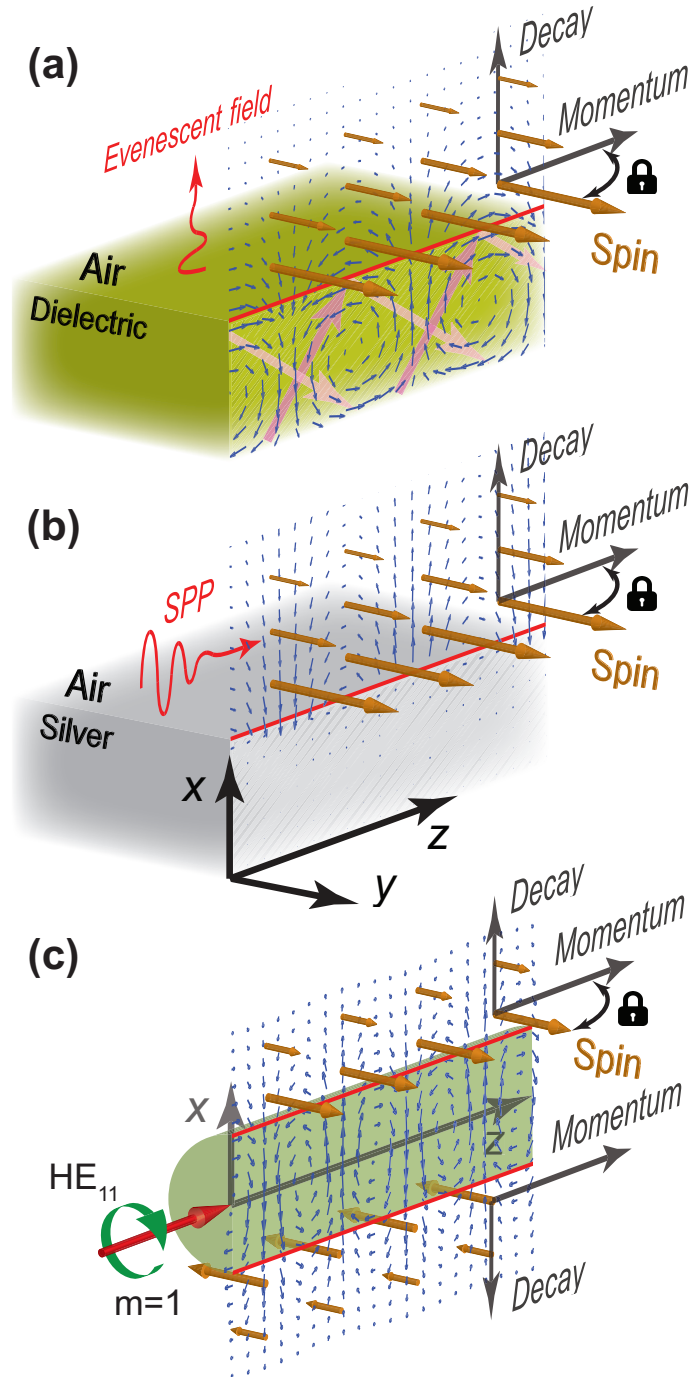


Figure 2.1. Direction of transverse spin in evanescent fields for (a) total internal reflection, (b) surface plasmon polariton, and (c) optical fiber. The blue vectors show the electric field at an instance of time and the orange vectors show the direction of transverse spin. In all cases the direction of momentum, direction of decay, and transverse spin follow a right-hand rule.

incident evanescent wave is intrinsically handed. In Fig. 2.2(a), the achiral particle scatters the evanescent wave equally in two directions leading to zero net momentum in direction transverse to the plane of incidence and therefore no recoil force in this direction. However, Fig. 2.2(b) shows the case of a chiral particle which interacts with the spin of the evanescent waves and scatters the light asymmetrically leading to a “sideways” (lateral) recoil force i.e. transverse to the incident plane. This phenomenon is the cause of the anomalous lateral force reported in recent works [3], [10]. The resulting force will be in opposite directions for the two enantiomers of a chiral particle. To obtain a lateral force on an achiral particle, we can use the reciprocal experiment of Fig. 2.2(a) shown in Fig. 2.2(c). This means, if we illuminate an achiral particle placed near an air/dielectric interface with right-handed circularly polarized light propagating in $+\hat{y}$ direction, the scattered evanescent fields will be right-handed i.e. their spin is fixed. This fixes the direction of momentum parallel to the interface due to spin-momentum locking and the tunneled evanescent waves propagate preferentially with a net momentum in $-\hat{z}$ direction. This directional scattering will apply a recoil force on the particle in $+\hat{z}$ direction. Note the right-hand rule from Fig. 2.1 is central to this interplay of spin and momentum of incident light and lateral recoil force.

2.4 Spin-momentum Locked Optical Force in Total Internal Reflection

The effect of the chirality of a particle on the transverse spin density force is illustrated in Fig. 2.3, where the forces on a chiral and an achiral particle are compared. By calculating the force in a purely evanescent wave we show that the origin of the aforementioned lateral optical force is the transverse spin of evanescent waves. Fig. 2.3(c) shows that the lateral force only appears when the angle of incidence is larger than the critical angle of the prism/air interface. In this regime, the power is fully reflected and only evanescent fields exist beyond the prism surface. Furthermore, this figure shows that only a chiral particle can probe the transverse spin of an evanescent wave if the incident wave is linearly polarized.

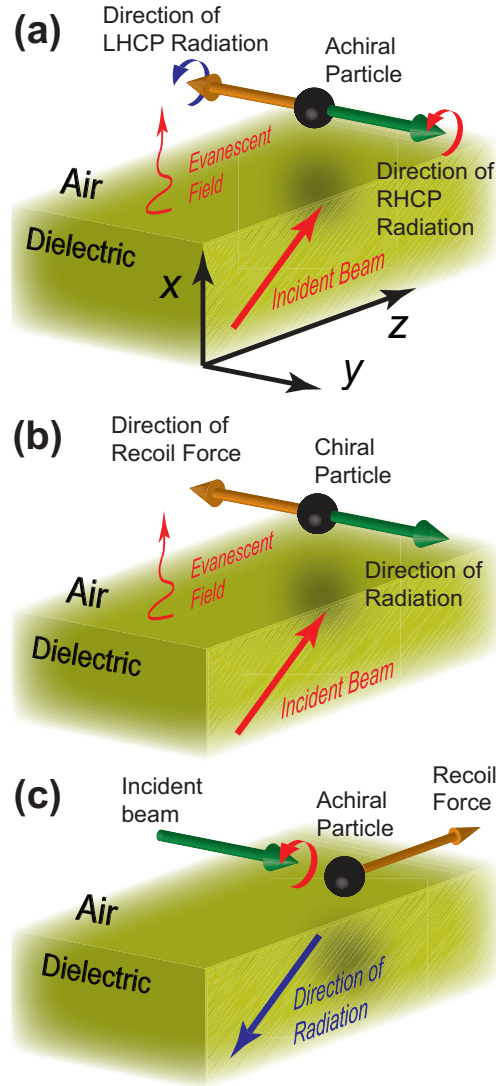


Figure 2.2. Lateral force caused by transverse spin of the evanescent fields. (a) An achiral non-magnetic particle is placed in an evanescent field generated by total internal reflection of a p polarized incident beam. The handedness of the scattered radiation follows the direction of transverse spin of the evanescent field and is locked to the direction of momentum of the incident field. Due to symmetry, the scattered waves propagating in $+\hat{y}$ and $-\hat{y}$ directions have equal power densities which leads to zero lateral force on the particle. (b) A chiral particle is placed in an evanescent field experiences a lateral force. The lateral force is proportional to the transverse spin of the evanescent field. The spin of the evanescent field causes a directional scattering by the particle. The direction of the scattered radiation is parallel (anti-parallel) to the direction of spin, therefore, the recoil force caused by the directional radiation will be anti-parallel (parallel) to the direction of spin. (c) Reciprocal setup of (a). An achiral particle placed near a dielectric surface is illuminated by a circularly polarized beam. The scattered radiation by the particle propagates directionally inside the dielectric and exerts a recoil force on the particle.

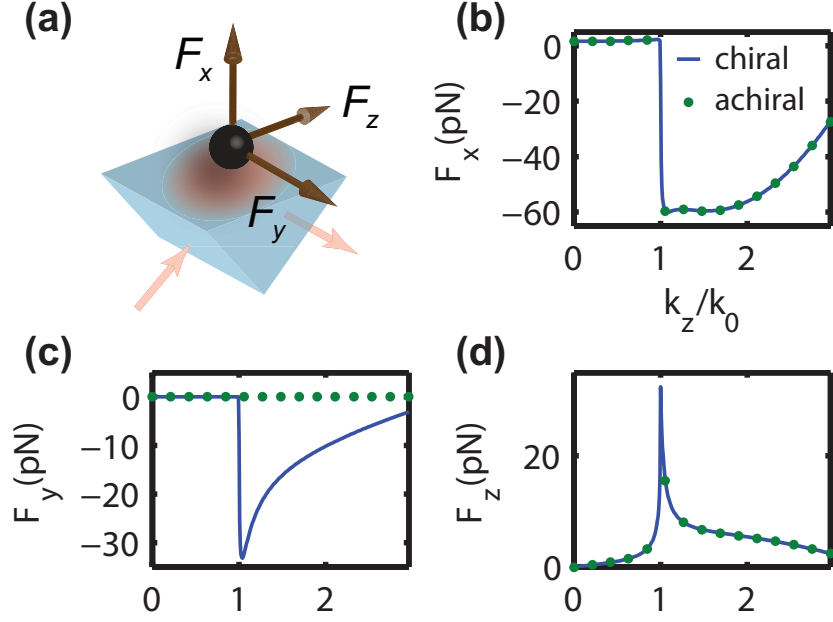


Figure 2.3. Optical forces on a chiral particle (solid line) and an achiral particle (dots) in an evanescent field. (a) Schematic of a chiral particle placed near a prism showing the direction of incident beam and the forces. (b) Time averaged force in \hat{x} direction. This component of the force is dominated by the gradient force and is toward the prism. (c) Time averaged force in \hat{y} direction. This component of the force is proportional to the transverse spin. (d) Time averaged force in \hat{z} direction. This component of the force is dominated by radiation pressure. The particle is $100nm$ away from the surface of the prism. See Appendix A for the polarizability of the chiral and achiral particles. The incident beam is p polarized with wavelength $\lambda = 5\mu m$ and carries a power of $p = 50mW/mm^2$. The refractive index of the prism is $n = 3.5$ and the horizontal axis is related to the incident angle of the beam.

2.5 Spin-momentum Locked Optical Force in an Optical Fiber

We now show effects of spin-momentum locking phenomenon on optical forces in the cylindrically symmetric case of an optical fiber. The fundamental mode of an optical fiber is the HE_{11} mode [89] and can appear in two degenerate forms of $m = 1$ and $m = -1$ where m is related to the OAM of the mode. Fig. 2.4 depicts how this OAM related to the propagating wave field is fundamentally different from the transverse spin density related to the evanescent waves present outside the core of the fiber. This is revealed through the arrows depicting the contrasting nature of energy flow and spin-density flow when the OAM

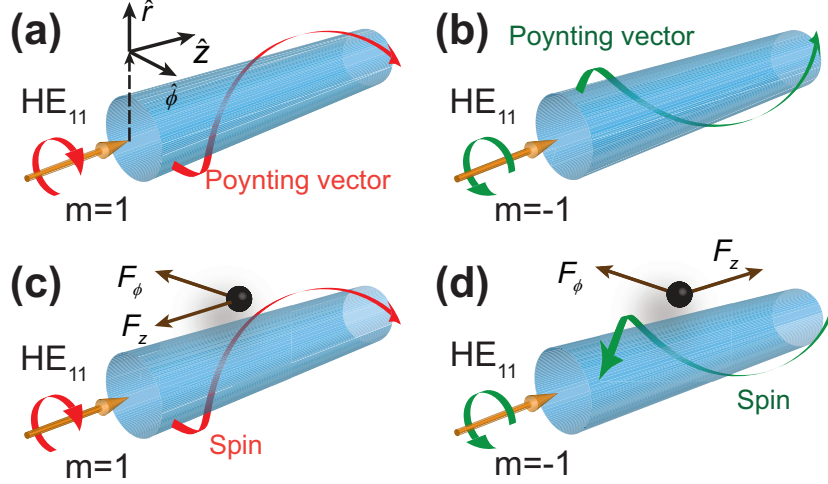


Figure 2.4. Direction of Poynting vector, spin density and spin density force on a chiral particle for $m = 1$ and $m = -1$ HE_{11} modes. (a) and (b) Direction of Poynting vector outside the optical fiber for the two modes. (c) and (d) Direction of spin density and spin density force outside the optical fiber for the two modes. The longitudinal component of the spin density has opposite directions for the two modes, but, its transverse component is in the same direction for both modes which shows the spin-momentum locking in evanescent fields. The direction of spin density force on a chiral particle placed outside the optical fiber is also shown. The longitudinal component of the force, F_z , has opposite directions for the two modes, but, the transverse component, F_ϕ , is in the same direction for both modes.

is reversed. The direction of the twist of the transverse spin-density around the fiber is fundamentally tied to the momentum and is unrelated to the OAM. A detailed analysis will be presented in future work and here we focus only on the consequences of this phenomenon on the non-trivial direction of optical forces on a chiral particle in the near-field of an optical fiber.

To compare the magnitude of the spin-momentum locked optical force with the other forces acting on a chiral particle, we have calculated the total force in different directions on a chiral particle placed near an optical fiber (Fig. 2.5). This figure compares the force for $m = 1$ and $m = -1$ modes. The radial component of the force F_r is dominated by the gradient force. Since the spin density force has no contribution in this component of the force, it has the same magnitude for both the modes. In Fig. 2.5(d) we show the striking contrast between positive and negative angular momentum modes. The longitudinal force F_z

changes sign in accordance with the angular momentum mode. Its behavior is fundamentally different from the transverse spin density force. Fig. 2.5(c) is the non-trivial lateral force which is related to the transverse spin-density. Its direction is independent of the angular momentum and is related only to the propagation direction in the fiber. The difference between the magnitude of this component for the two modes is because the $\hat{\phi}$ component of the radiation pressure has different directions for the two modes (Fig. 2.4).

2.6 Conclusion

In conclusion, we have demonstrated universality of spin-momentum locking and the resulting lateral optical force on chiral particles in evanescent fields. We have shown that the phenomena giving rise to unidirectional coupling is also at the heart of the lateral optical force. The lateral optical force can be harnessed for manipulation of small particles and chirality sorting in evanescent wave fields.

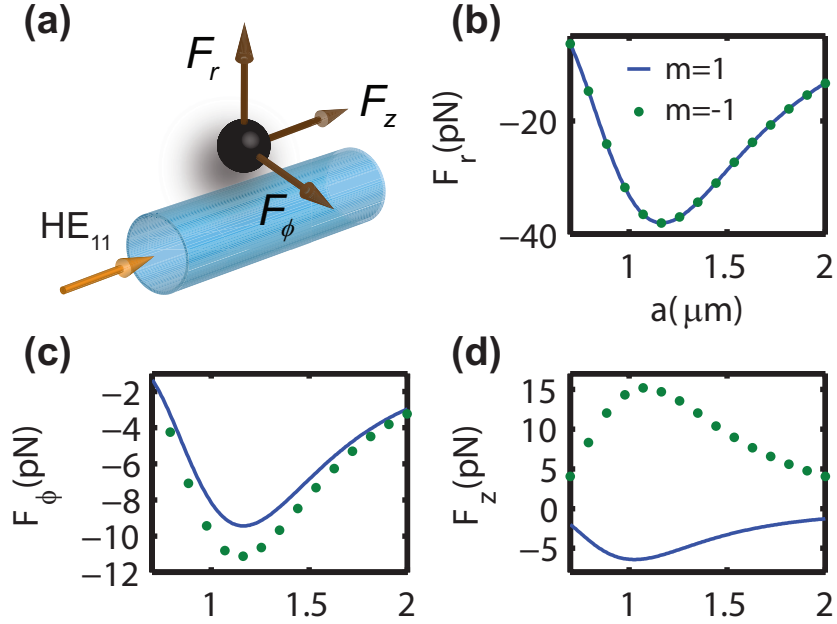


Figure 2.5. (a) Schematic of a chiral particle near an optical fiber. (b), (c) and (d) Time averaged optical force in different directions plotted versus radius of the fiber. The solid line shows the force for $m = 1$ mode and the dots show the force for $m = -1$ mode. The \hat{r} component is dominated by the gradient force and has the same value for both modes while the $\hat{\phi}$ component is dominated by the spin density force. The transverse component of the Poynting vector applies a radiation pressure force which is responsible for the difference in the $\hat{\phi}$ component of the force for the two modes. The direction of the transverse spin and transverse spin density force is independent of the OAM of the mode and is locked to its direction of propagation. Both radiation pressure and the spin density forces contribute to the \hat{z} component of the force. The radiation pressure is in $+\hat{z}$ direction for both modes but the spin density force has opposite directions. Therefore, for the $m = 1$ mode the force is in $+\hat{z}$ direction but for the $m = -1$ mode the force is in the opposite direction. The particle is placed 100nm away from the surface of the fiber and has the same properties as the particle in Fig. 2.3. The refractive index of the fiber is $n_1 = 1.5$ and the surrounding medium is vacuum. The wavelength of the incident beam is $\lambda = 5\mu\text{m}$ and the mode carries a total power of $P = 1\mu\text{W}$.

3. QUANTUM SENSING OF PHOTONIC SPIN DENSITY USING A SINGLE SPIN QUBIT

Nitrogen-vacancy (NV) centers in diamond have been used to probe electron spin excitations in matter such as magnons [32], magnetic thin films [33], and magnetic skyrmions [35]. Even in nonmagnetic materials such as plasmonic silver; low-frequency evanescent wave Johnson noise and ballistic transport of electrons can be probed by NV centers [34]. NV centers in diamond can also work as navigation guidance systems by vector sensing of earth’s magnetic field [90]. This emerging frontier of research shows how coherence in spin qubits allows for ultra sensitive read-out of magnetic fields and magnetic noise in quantum materials and beyond. It is therefore intriguing to explore how the synthetic magnetic fields generated by light can be probed using the same quantum metrological principles. Here, we put forth the concept of quantum metrology of a property of dynamical light fields at room temperature.

We propose and demonstrate that NV centers in diamond can sense the local polarization of spinning light fields within ultra small mode volumes. Our sensor is a single spin qubit interacting with the effective static magnetic field generated by a circularly polarized light field. We measure the induced phase of the spin qubit through optical read out to directly detect the photonic spin density (PSD) of a laser beam red-detuned to the optical transition of the NV center. We demonstrate coherent interaction at room temperature paving the way to probe exotic spin states of photons. We also put forth a rigorous theory of the interaction between photon spin density and the spin qubit using the full NV center Hamiltonian. Finally, we shed light on how on-chip nanophotonic structures possess effective static magnetic fields arising from the intrinsic spin of evanescent waves. This effect can be exploited in future spin quantum electrodynamics devices for on-chip targeted addressing of spin qubits.

The spinning field of light has long been associated with the concept of global polarization [1], [2]. Here the spin angular momentum (SAM) of light is a vector with its direction pinned parallel to the momentum of a far field propagating wave. In stark contrast, the PSD has only recently emerged to the forefront of nanophotonics [18], [21], [91]–[93]. PSD in confined or structured light beyond the traditional paraxial regime can exhibit exotic spatial variation of local polarization known as spin texture [94]. In recent years, exploring the near-field

properties of this spin texture has led to the discovery of exotic phenomena such as photonic skyrmions and topological electromagnetic phases of matter [25], [26], [95].

Interesting phenomena originating from near-field photon spin density include directional spontaneous emission, one-way scattering of surface plasmon polaritons, transverse spin in free space light beams, and anomalous optical forces [11], [14], [29], [88], [96]. Here, the nature of PSD is inferred indirectly through directional phenomena, i.e., spin-momentum locking or spin to orbital angular momentum conversion [24], [97], [98]. We note that the orbital angular momentum (OAM) of light is an extrinsic degree of freedom that can be directly detected due to its wavelength scale helical phase signatures [99]. However, direct measurement of PSD remains a challenge since the fundamental property of photon spin density exists in subwavelength volumes of the light field. Therefore, there is an urgent need to develop a nanoscale photon spin probe similar to near-field scanning optical microscopy [88], [93] routinely used to detect dipolar electric fields or magnetic force microscopy which can map nanoscale texture of electron spins.

3.1 Theoretical Model of Spin Qubit Interacting with Photonic Spin Density

In order to demonstrate the ultra-subwavelength probing of PSD, we study the interaction between the spin of a monochromatic optical beam and an NV center that is placed on an atomic force microscopy (AFM) tip. This is a versatile system for future explorations of spin texture of complex optical beams. We note that the light-matter interaction between the Gaussian beam and the spin qubit only occurs due to virtual photon transitions since our incident beam is far detuned from the energy levels of the NV center. Thus the signature of the PSD is in the phase of the single spin qubit. We therefore need quantum metrological tools to quantify this unique coherent light-qubit interaction at room temperature.

In classical electrodynamics (CED), the total angular momentum of charged particles and electromagnetic fields are given by $\vec{J}_{\text{CED}} = \sum_{\alpha} \vec{x}_{\alpha} \times \vec{p}_{\alpha} + \epsilon \int d^3x \vec{\mathcal{E}}_{\perp} \times \vec{A}_{\perp} + \epsilon \int d^3x \mathcal{E}_{\perp}^j (\mathbf{x} \times \nabla) A_{\perp}^j$ (see chap. I in Ref. [17]), where $\vec{\mathcal{E}}(\vec{r}, t)$ is the electric field, $\vec{A}(\vec{r}, t)$ is the vector potential, the subindex \perp denotes the transverse part of the vector field, and ϵ is the permittivity. These three terms denote the OAM of the charges, SAM of light, and OAM of light, respectively.

In this equation, the integral kernels give the photonic spin and OAM densities. While the term SAM is also used to describe the kernel of the SAM term in the literature, we use the term PSD for the kernel to distinguish it from the SAM. Our goal is to emphasize on the local and nanoscale characteristics of it. In this chapter, we demonstrate a technique that can be used to measure the PSD beam $\vec{S}^{\text{obs}} = \epsilon \vec{\mathcal{E}}_{\perp}(\vec{r}, t) \times \vec{A}_{\perp}(\vec{r}, t)$ [16] with nanoscale resolution using a single NV center in diamond.

For a monochromatic beam with frequency ω_0 , the PSD can be written as $\vec{S}^{\text{obs}} = (1/4\omega_0)\text{Im}[\epsilon \vec{E}^* \times \vec{E} + \mu \vec{H}^* \times \vec{H}] = \vec{S}_E^{\text{obs}} + \vec{S}_M^{\text{obs}}$ where $\vec{E}^*(\vec{H}^*)$ denotes the complex conjugate of the complex electric (magnetic) field [19], [20], i.e., $\vec{\mathcal{E}}_{\perp} = (\vec{E} + \vec{E}^*)/2$. The PSD is time independent and is related to the handedness of the polarization of the beam. According to the selection rules of electric-dipole transitions, circularly polarized light will change the electronic orbital angular momentum by $\pm\hbar$ while keeping the electron-spin state unchanged. However, due to spin-orbit coupling, the transition frequencies in the NV center become dependent on the electron spin states as shown in Fig. 3.1(b). Under a detuned incident light beam, virtual electric-dipole transitions will induce ac Stark shifts in the ground electronic state [100]–[103]. As illustrated in Figs. 3.1(c) and 3.1(d), the amplitude of these shifts (δ_0 and $\delta_{\pm 1}$) depend on both the electronic spin state of the NV center and the photonic spin density of the excitation. We show that this effect manifests itself as a PSD dependent effective static magnetic field. We exploit the single NV center as a nanoscale quantum magnetometer [104] to measure this effective static magnetic field created by the target spinning light.

We consider the detailed energy level structure of NV centers in the basis of RCP and LCP transitions to express the net energy shift as a function of PSD. The effective excited-state Hamiltonian of the NV center is given by [105], [106],

$$\begin{aligned}
H_{\text{ES}} = & (\gamma_{\text{NV}}B + \Delta_{\text{es}} + \lambda_z)|A_{\uparrow}\rangle\langle A_{\uparrow}| \\
& + (-\gamma_{\text{NV}}B + \Delta_{\text{es}} + \lambda_z)|A_{\downarrow}\rangle\langle A_{\downarrow}| - 2\Delta_{\text{es}}|E_R\rangle\langle E_R| \\
& - 2\Delta_{\text{es}}|E_L\rangle\langle E_L| + (\gamma_{\text{NV}}B + \Delta_{\text{es}} - \lambda_z)|E_{\uparrow}\rangle\langle E_{\uparrow}| \\
& + (-\gamma_{\text{NV}}B + \Delta_{\text{es}} - \lambda_z)|E_{\downarrow}\rangle\langle E_{\downarrow}|,
\end{aligned} \tag{3.1}$$

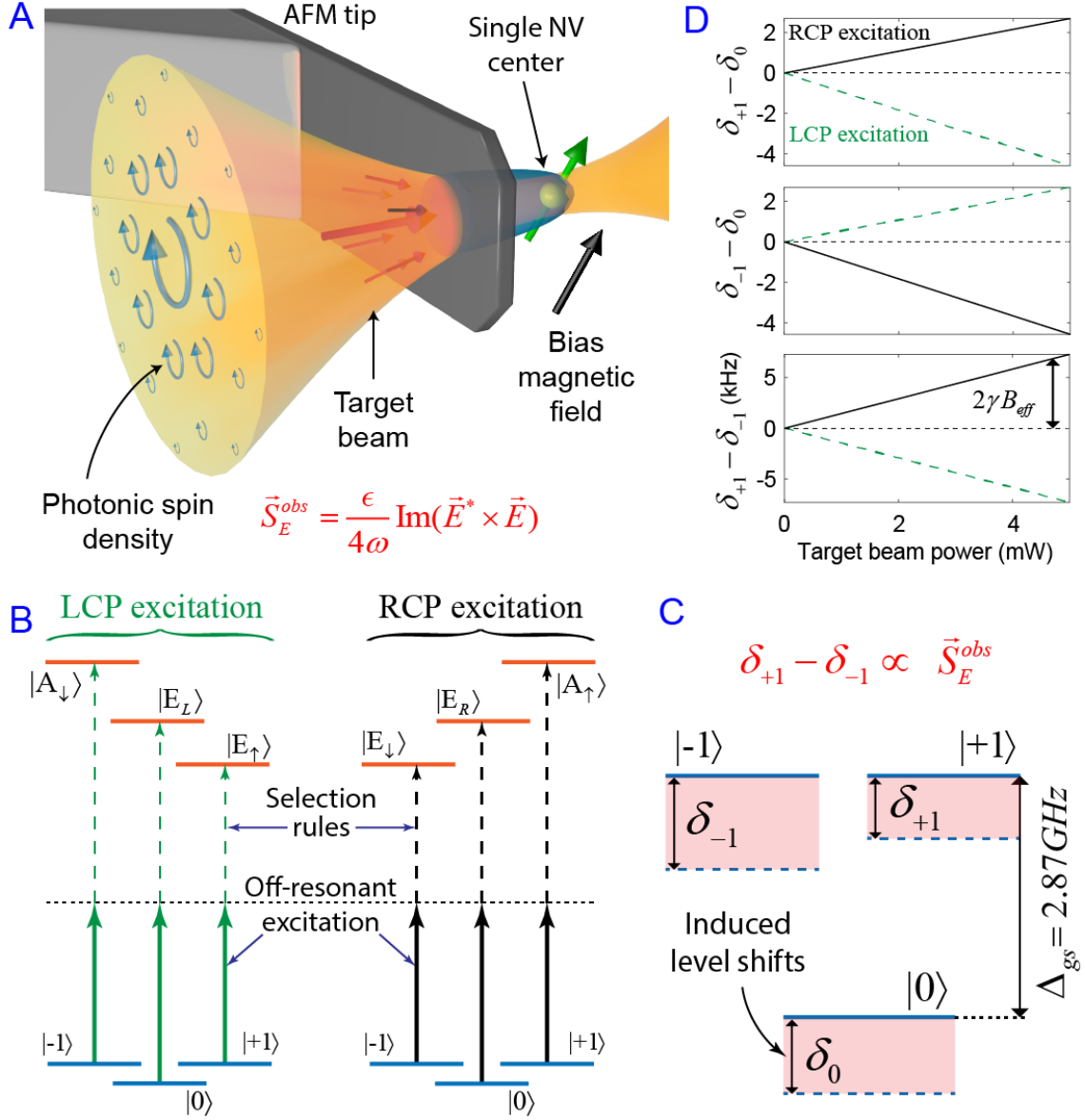


Figure 3.1. Probing PSD with a single NV center. (a) A target beam, red-detuned to the NV center transition, is incident on a single NV center on an AFM tip. We measure the relative energy level shifts in the ground state and show its proportionality to the PSD. The single NV center serves as a room-temperature nanoscale probe for PSD. (b) Ground- and excited-state energy levels of an NV center showing the selection rules for RCP and LCP excitation. (c) Level shifts induced in the ground state due to the virtual transitions under the off-resonant target beam. (d) Power and polarization (spin) dependence of the relative energy shifts in the ground state, resembling Zeeman splitting. An effective static magnetic field is defined as $B_{eff} = (\delta_{+1} - \delta_{-1})/2\gamma$.

where $\gamma_{\text{NV}} = 2\pi \times 28$ MHz/mT, B is the external static magnetic field, $\lambda_z \approx 2\pi \times 5.5$ GHz is the spin-orbit coupling, and $\Delta_{\text{es}} \approx 2\pi \times 1.42/3$ GHz is the spin-spin-induced zero-field splitting. $|A_\uparrow\rangle$, $|A_\downarrow\rangle$, $|E_R\rangle$, $|E_L\rangle$, $|E_\uparrow\rangle$, and $|E_\downarrow\rangle$ are spin and orbital angular momentum resolved excited states shown in Fig. 3.1(b). Using second-order perturbation theory, ac Stark shift for the ground-state energy levels is [100], [107],

$$\delta_i = \frac{1}{4\hbar^2} \sum_f \frac{|\langle f|\vec{d}|i\rangle \cdot \vec{E}(\vec{r}, t)|^2}{\Delta_{if} + \Gamma_f^2/4\Delta_{if}}. \quad (3.2)$$

where $|i\rangle$ and $|f\rangle$ are the initial and final states for all possible transitions, Δ_{ij} is the difference between the center frequency of the off-resonant excitation (ω_0) and the resonance frequency of the transition (ω_{ij}), and Γ_f is the spontaneous decay rate of the final state. Using the Hamiltonian in Eq. (3.1) and the transition rules for circularly polarized incident light, we arrive at the result of the effective static magnetic field generated by spin density of light (see Appendix B):

$$B_{\text{eff}} \equiv \frac{\delta_{+1} - \delta_{-1}}{2\gamma_{\text{NV}}} \propto \vec{S}_E^{\text{obs}} \cdot \hat{n}, \quad (3.3)$$

where \hat{n} is the direction of the NV center. From Eq. (3.3), we see that the strength of the effective static magnetic field is proportional to the projection of the electric PSD (\vec{S}_E^{obs}) on the NV center axis (\hat{n}). In the expression above, we have used the spin states $|\pm 1\rangle$ to form the probe qubit as it leads to effective static magnetic fields directly proportional to the PSD. One can also use $|0\rangle \leftrightarrow |\pm 1\rangle$ transitions as the probe qubit. We show a comparison between the choice of probe qubits in Fig. 3.2(c). The magnetic portion of the PSD (\vec{S}_M^{obs}) does not interact with the NV center since the optical transitions are derived by electric dipole interactions.

The PSD of the target beam is determined by its power and degree of circular polarization. In our experiment, the wavelength of the target beam is $\lambda_0 = 800\text{nm}$, which is far off-resonant to the optical transition of the NV center at $\lambda = 637\text{nm}$ (Fig. 3.1(b)). We control the PSD by tuning the power of the beam and the angle θ between the linear polarizer and the quarter-wave plate (QWP) (see Fig. 3.2(a)). The degree of circular polarization (i.e., the photonic spin density) is $\vec{S}_E^{\text{obs}} \propto \sin(2\theta)\hat{z}$, where \hat{z} is the direction of propagation of the

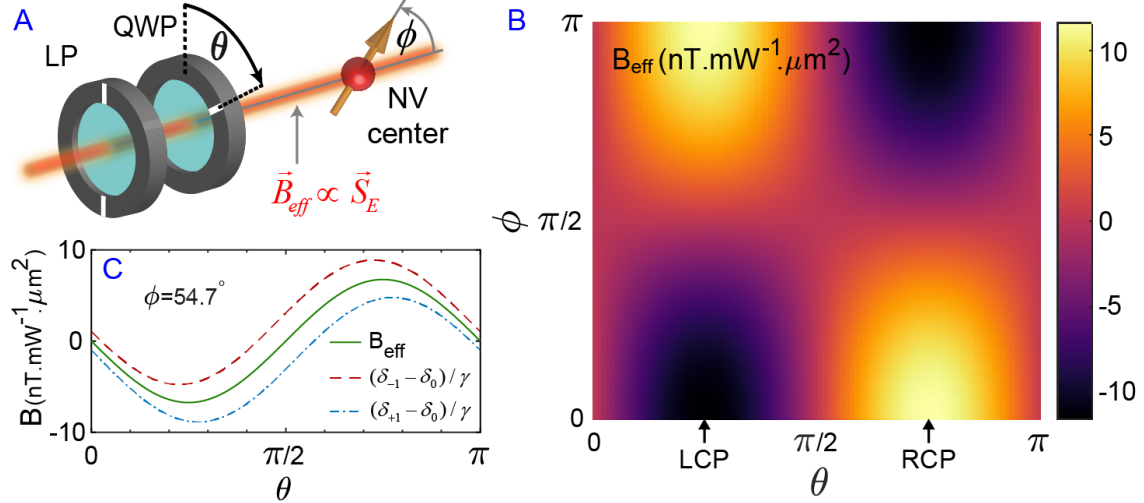


Figure 3.2. Effective static magnetic field induced by PSD. (a) A linear polarizer and a quarter wave plate control the PSD. (b) The effective magnetic field calculated for different QWP angles (θ) and alignment angles (ϕ). (c) The effective magnetic field calculated for an NV center in a (100) cut diamond, $\phi = 54.7^\circ$.

beam. Equation (3.3) shows that an NV center can only sense the projection of a magnetic field on its defect axis. Therefore, the measured effective static magnetic field also depends on the alignment angle ϕ between the NV center axis and the PSD vector. We show the theoretical simulation of the effective static magnetic field B_{eff} sensed by an NV center, as a function of θ and ϕ in Fig. 3.2(b). We should note that in the experimental results, the alignment angle is fixed at $\phi = 54.7^\circ$ due to the growth angle of the diamond crystal. For this specific angle, we show the effective magnetic field experienced by the probe qubit in Fig. 3.2(c). This variation of the effective static magnetic field with degree of circular polarization is the unique signature of PSD. We note that the target laser is red-detuned to the optical transition of the NV center and is not absorbed by the NV center. Therefore, the resulting effective static magnetic field is not due to the absorption or emission related spectral features of the NV center. It is related to the induced phase in the spin qubit measured by optical read out.

Table 3.1. Dynamical decoupling measurement parameters used for the results shown in Fig. 3.4.

Number of XY8 repetitions	4
Free precession time (τ)	$1.2\mu s$
Total sequence time	$\sim 40\mu s$
Target beam pulse length (τ')	$1\mu s$
Total interaction time	$15\mu s$
π -pulse length	$\sim 50ns$

3.2 Experimental Demonstration Using a Single NV Center

We overcome the challenge of room-temperature observation of PSD to pave the way for future on-chip applications. We exploit a large detuning of the target PSD beam to the optical transition of the NV center to avoid absorption of photons by the NV center which would result in a loss of coherence. This detuning results in an amplitude of a few tens of nanotesla for the generated effective static magnetic field. In order to probe this effective magnetic field at the location of the single NV center, we use ac magnetometry techniques at room temperature. In ac magnetometry, high sensitivity is achieved due to a long coherence time from spectral filtering of magnetic fluctuations (e.g., nuclear noise) coupled to the NV center [36], [54]. Figure 3.3 shows the dynamics of the measurements. A 532nm laser is used to initialize and readout the state of the qubit. After initialization, a series of microwave pulses are sent in XY8 configuration to achieve dynamical decoupling of the qubit from background noise [108]. The intensity of the target beam is modulated to match the frequency of the XY8 pulse for ac magnetometry. Furthermore, we perform two measurements for which the phase induced by the PSD has opposite signs (Figs. 3.3(e) and 3.3(f)). This is achieved by taking advantage of the sign of an ac field as shown in Fig. 3.3(a). We suppress the effect of any systematic noise by subtracting the outcome of these two measurements. The parameters used in the measurements are shown in Table 3.1.

The first striking evidence of photonic spin density measurement is shown in Fig. 3.4(c). We observe that the effective static magnetic field generated by PSD directly follows the ellipticity of the polarization of the target beam. For a Gaussian beam, the PSD is proportional to the degree of ellipticity of the polarization. In our experiment, we control the

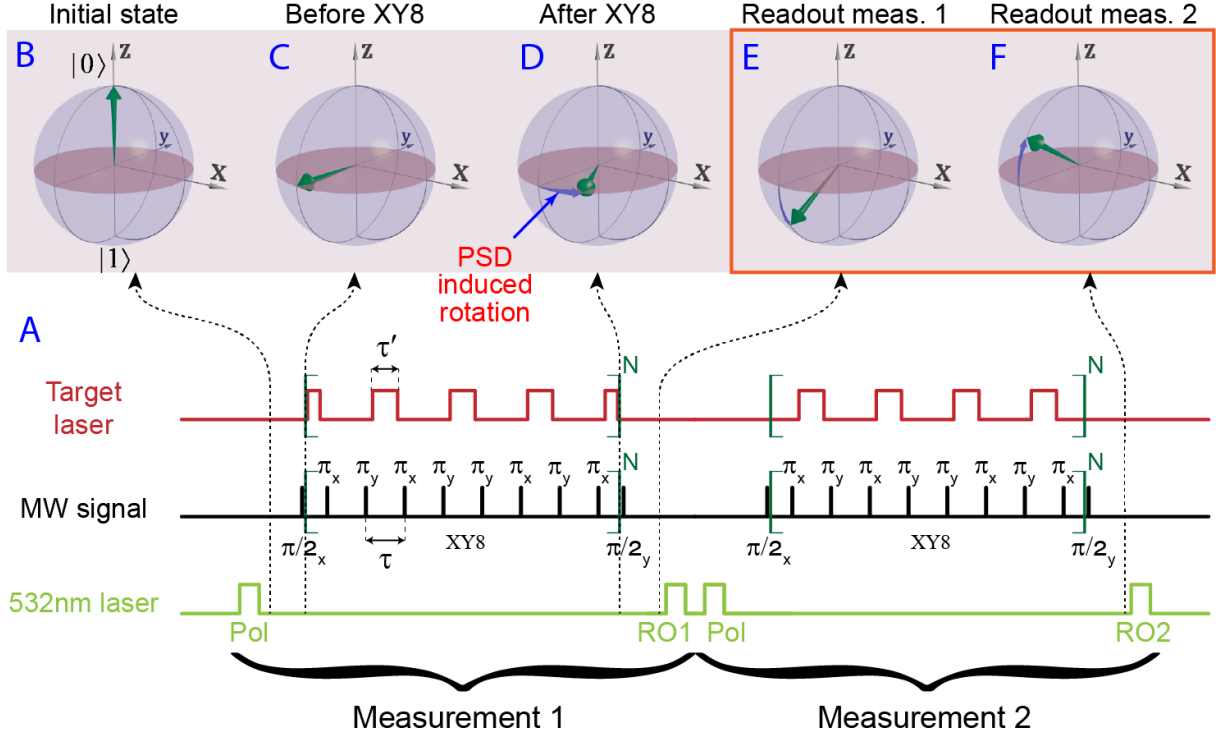


Figure 3.3. Isolating the signature of photonic spin density using dynamical decoupling and ac magnetometry with a single spin qubit. (a) Pulse sequence used for measuring the PSD. In each measurement a pair of 532nm laser pulses initialize (polarize) and read out the state of the NV center. During each measurement an XY8 MW pulse performs dynamical decoupling on the spin of the NV center. The target beam, generating the PSD, is turned on and off during the XY8 sequence to generate a net effect on the final state of the NV center. We perform two measurements in which the target beam induces rotations in opposite directions on the spin vector in the Bloch sphere. By subtracting the outcome of these two measurement we eliminate any systematic noise in the measurement. [(b)-(f)] Bloch sphere representation of the state of the qubit after polarization, before the XY8 pulse, after the XY8 pulse, and before readout. Panels (e) and (f) show a schematic comparison between the PSD-induced rotations in measurement 1 and measurement 2. The PSD is generated by the target beam. RO, readout; Pol, polarizing.

ellipticity of the target beam using a linear polarizer and QWP. Fig. 3.4(c) shows the observed dependence of the effective static magnetic field on the angle of the QWP (θ). Also plotted are a sinusoidal fit of the data (red dashed curve) and the result of full wave numerical simulations (purple curve). The data show a small dc offset in the curve which is not present in Eq. (3.3). This offset is related to an asymmetry in the system's geometry,

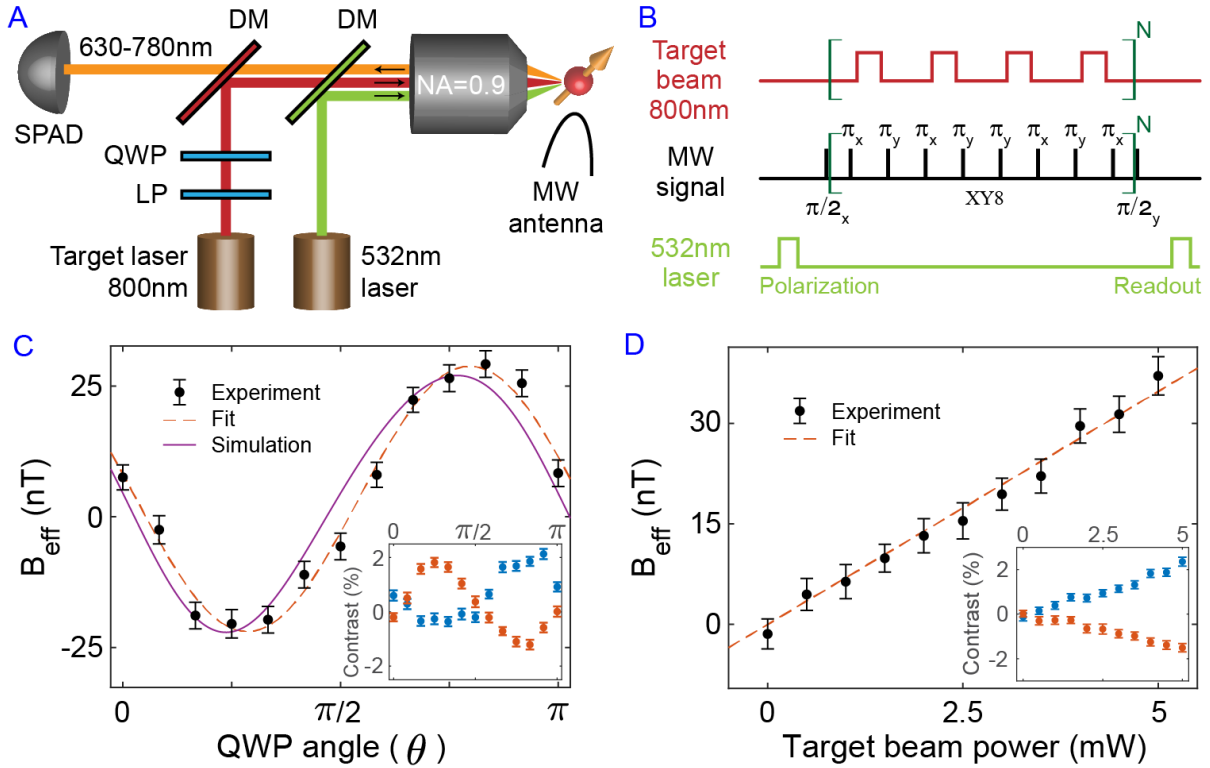


Figure 3.4. Demonstration of nanoscale PSD probe with a single NV center. (a) Simplified schematic of the experimental setup. (b) Pulse sequence showing dynamical decoupling for ac magnetometry and amplitude modulation of the target beam to generate an ac effective magnetic field suitable for high sensitivity measurement. (c) Measured PSD for different QWP angles with target beam power of 4mW. The dashed red curve is a sine fit to the data, the solid purple curve is the numerical simulation results, matching closely to the measurements. (d) Measured PSD as a function of incident power for $\theta = 3\pi/4$ showing a linear dependence. The dashed red curve is a linear fit. Insets show the raw measurement data for $|0\rangle \rightarrow | + 1\rangle$ (red) and $|0\rangle \rightarrow | - 1\rangle$ (blue) transitions. Panels (c) and (d) show that the effective field is directly proportional to PSD.

which would lead to the presence of transverse spin at the location of the NV center. This transverse spin obeys spin-momentum locking rules [21], [96] and does not depend on the QWP angle and therefore, gives rise to the offset (see Appendix F).

The second convincing proof of PSD measurement is the linear dependence of the effective static magnetic field on the power of the beam [Eq. (3.3)] shown in Fig. 3.4(d). The PSD is linearly proportional to the power of the beam. This is in contrast to real magnetic fields where the amplitude scales with the square root of the power. The dashed red line shows a linear fit to the measured data. It should be noted that for each data point in Figs. 3.4(c) and 3.4(d) we measure the energy shifts $\delta_{\pm 1} - \delta_0$ separately and calculate the effective static magnetic field B_{eff} according to Eq. (3.3). The inset of these figures show the raw data for these measurements.

These two unique features in the measured effective static magnetic field also show that the measured quantity is not affected by temperature oscillations in the diamond caused by the target laser. A change in the temperature of the diamond can also lead to a shift in the energy levels of the NV center [109]. However, this effect is distinguishable from the effective static magnetic field induced by the PSD because the induced temperature oscillation is independent of the polarization of the beam while the PSD-induced effect depend on the degree of ellipticity of the beam as shown in Fig. 3.4(c). The results in Figs. 3.4(c) and 3.4(d) do not show any significant temperature oscillations in the sample.

3.3 Effective Static Magnetic Field in Optical Waveguides

We now discuss how this universal photonic spin density-induced effective static magnetic fields can be used in future generation of on-chip spin QED applications. We note that evanescent waves are a ubiquitous resource available on a scalable nanophotonic platform. These evanescent waves possess an intrinsic universal spin that can exert effective static magnetic fields on spin qubits with a subwavelength resolution. This effective magnetic field is only manifested on interaction of PSD with NV centers and is a synthetic magnetic field. PSD-induced effective static magnetic fields can produce giant spatial gradients on the order of $10T/m$ with an ultrafast temporal response [110]. This allows for on-chip and targeted

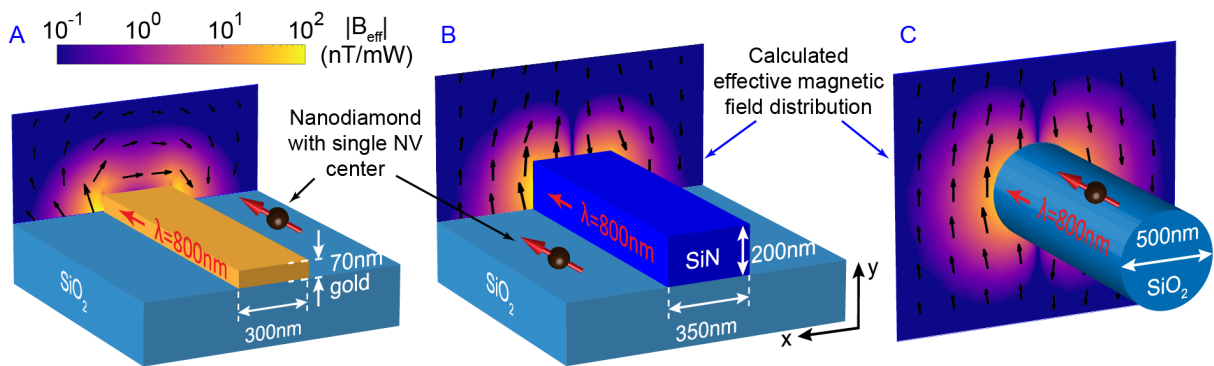


Figure 3.5. Effective static magnetic field sensed by an NV center near optical waveguides. Our rigorous simulations are performed using full wave analysis of the optical fields along with the light-matter interaction theory of Sec. 1. A plasmonic waveguide (a), a ridge waveguide (b), and an optical fiber (c) all producing transverse effective static magnetic fields due to the PSD of their evanescent fields. The direction of the effective static magnetic field is shown with black arrows and its amplitude with the colormap. The mode of the ridge waveguide is transverse electric (TE) and the mode of the optical fiber is \hat{x} polarized HE_{11} .

nanoscale addressing of spin qubits. Figure 3.5 shows the effective static magnetic field in the near-field region of a plasmonic waveguide, a ridge waveguide, and an optical fiber. This effective static magnetic field originates solely from the PSD of the evanescent waves in the vicinity of the waveguides. The direction of the field is in the $x - y$ plane and is shown with black arrows. All three cases show short-range effective static magnetic field suitable for addressing single NV centers on chip or deposited on the surface of an optical fiber. This phenomenon opens the door to dense integration of single spin qubits for on-chip spin QED applications.

3.4 Conclusion

In this chapter, we have demonstrated a room-temperature quantum probe for nanoscale spinning light fields. The spinning optical beam induces a magnetic field in the spin qubit causing a qubit rotation on the Bloch sphere (phase accumulation). The ultra-subwavelength behavior of spin angular momentum possess unique challenges for direct observation which we overcome using state of the art quantum sensing approaches. Our measurement reveals that

the NV center's room-temperature excited-state energy levels display striking agreement with those found in low-temperature measurements. This is in contrast to direct measurements on the excited state where its full features cannot be revealed due to time averaging [111], [112]. Our work can lead to new spin-dependent topological phases of light and also presents a way to exploit the universal resource of spinning evanescent waves available on an integrated photonics platform.

4. OPTICALLY INDUCED STATIC MAGNETIC FIELD IN ENSEMBLE OF NITROGEN-VACANCY CENTERS IN DIAMOND

Nitrogen-vacancy (NV) centers in diamond have emerged as a promising nanoscale magnetometer for probing condensed matter phenomena [33], [113]–[116]. However, their application has been mostly focused on phenomena arising from electronic and nuclear spin excitations such as probing Johnson noise and magnetic skyrmions [34], [35]. In the previous chapter we demonstrated room-temperature probing of photonic spin density (PSD) with a single NV center [117]. This demonstration opens a new avenue in quantum sensing of properties of optical fields. The recent studies of the subwavelength properties of optical fields have led to the discovery of exotic phenomena such as photonic skyrmions and spin-momentum locking of light [21], [25], [26], [95], [96], [118]. The advent of the NV center as a quantum sensors for the PSD can accelerate the experimental research in this field.

4.1 Outline of the Problem

In this chapter we demonstrate room-temperature probing of PSD with an ensemble of NV centers. We use this platform to show that the PSD induced static magnetic field is a broadband effect in the far-off-resonant regime. We study its wavelength dependence and the scaling of the field with the beam’s polarization ellipticity and optical power. The results of this chapter will help pave the way for enhancements in the effective static magnetic field, with the goal of expanding its range of applications to on-chip spin quantum electrodynamics and all-optical qubit control.

Fig. 4.1 shows the schematics of the experiment. An elliptically polarized beam is focused onto a diamond sample with an ensemble of NV centers. The beam possesses PSD related to the ellipticity of its polarization [19], [117], [119]. The electric PSD is defined as $\vec{S}_E^{\text{obs}} = (\epsilon/4\omega_0)\text{Im}(\epsilon\vec{E}^* \times \vec{E})$ where ϵ is the permittivity of the medium and \vec{E}^* denotes the complex conjugate of the complex electric field. The interaction of the beam with NV centers induces a rotation in the spin vector of the NV centers. This rotation is proportional to the PSD

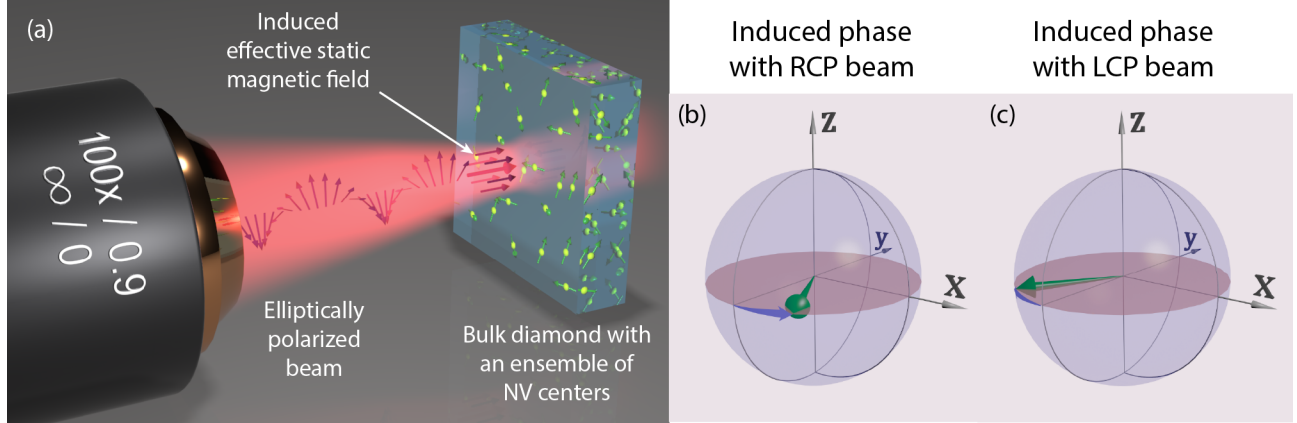


Figure 4.1. Interaction of the PSD of an optical beam with the electronic spin of NV centers. (a) Schematic of the measurements where a focused beam with elliptical polarization interacts with an ensemble of NV centers. (b) The Bloch sphere representation of the NV centers' electronic spin showing an induced rotation caused by the optical beam. The amount of this induced rotation depends on the PSD of the beam. The direction of the PSD and the bias magnetic field are aligned such that the induced rotation is equal for all NV centers in the ensemble.

of the beam and we define an effective static magnetic field to describe the strength of this interaction (see [117]). The NV centers are randomly scattered in the bulk of a single crystalline diamond, with their four different orientations determined by the (100) growth plane. A bias magnetic field is placed normal to the surface of the sample and is aligned to have the same projection along all NV center orientations. The PSD of the elliptically polarized beam is parallel to the direction of propagation and is also normal to the surface of the sample. This use of symmetries in the system ensures that the PSD induced rotation is the same over all of the NV centers. Moreover, the spot size of the PSD beam is designed to be larger than the spot size of the excitation laser to ensure that all excited NV centers are illuminated uniformly with the PSD beam. Figures 4.1(b) and 4.1(c) illustrate the rotation of the spin vector on the Bloch sphere. These two figures show the rotations induced by RCP and LCP incident beams. The two different polarizations induce rotations in opposite directions due to their different PSD. We measure this induced rotation by performing ac magnetometry using Hahn echo technique.

4.2 Coherence Time and Sensitivity

Figure 4.2 shows the pulse sequence used for the ac magnetometry measurements and our approach to optimizing the sensitivity of the measurement. The sensitivity is proportional to $\eta \propto \frac{1}{\sqrt{T_2}}$ [54]. Here η has units of nT/\sqrt{Hz} and T_2 is the NV centers' coherence time. Therefore, to optimize the sensitivity we maximize the coherence time. The top panel in Fig. 4.2(a) shows the pulse sequence used for measuring Rabi oscillations. The outcome of this measurement is shown in Fig. 4.2(b) and its inset. The red curve in this figure shows a fit to the envelope of the oscillations. The decay of this curve shows the coherence time T_2^* of the spin qubits. This coherence time is limited by inhomogeneous broadening of the ensemble resonance. This broadening is a result of the background magnetic noise generated by carbon-13 atoms in the diamond crystal. To reduce the effect of this noise we use Hahn echo pulse sequence shown in Fig. 4.2(b) [54], [58]. This pulse sequence takes advantage of the slowly varying nature of the background noise to lower its effect on the spin qubits. The outcome of this measurement is shown in Fig. 4.2(c). Noise cancellation causes the initial decay of the signal (blue dashed line) to be slower than the decay of the Rabi oscillations. Moreover, there are revivals in the signal due to the periodic motion of nuclear spins also under the influence of the applied bias magnetic field [120]. The envelope of the periodic revivals (dotted green line) shows the slowest decay in the coherence signal. We use the second revival ($\tau \approx 42\mu s$) for our measurements to achieve a long interaction time and the best sensitivity.

The pulse sequences for measuring the effective static magnetic field are shown in Fig. 4.3(a). The two sequences shown in this figure take advantage of the phase of an ac signal. If the PSD pulse is sent in the first half of the Hahn echo sequence (top panel) it induces a positive phase in the spin qubit and if it is sent in the second half (bottom panel) the induced phase will have the opposite sign. Therefore, we perform two measurements as shown in Fig. 4.3(a) and subtract the outcome of the two measurements to calculate the effective static magnetic field induced by the PSD signal. This technique helps with eliminating possible systematic errors in the read out process as well.

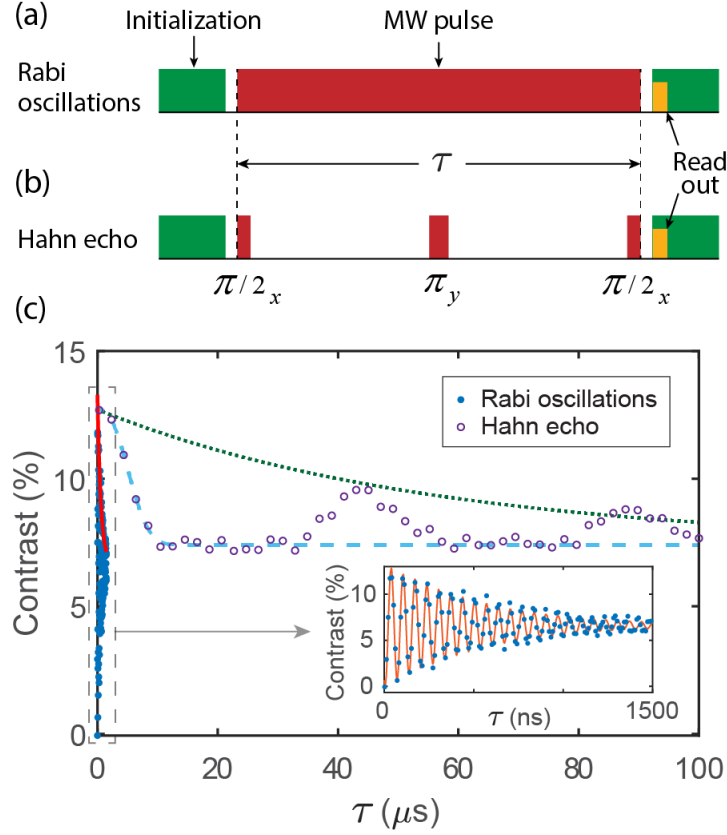


Figure 4.2. Optimizing the coherence time of NV center ensemble. (a) The pulse sequence used for measuring Rabi oscillations and inhomogeneous broadening T_2^* for the ensemble. (b) The Hahn echo pulse sequence for measuring spin echo and coherence time T_2 . (c) Measurement results for the pulse sequences shown in (a) (blue dots) and (b) (purple circles). The Rabi oscillations show the shortest timescale, T_2^* . The inset shows the detail of this measurement. The red line is the envelope of the red curve from the the inset. The Hahn echo shows a slower decay due to elimination of inhomogeneous broadening and periodic revivals in the signal. The fits to the decay and revivals are shown with dashed blue and dotted green lines, respectively. The revivals are due to the periodic motion of the carbon-13 nuclear spins under the bias magnetic field. We use the second revival point ($\tau = 42\mu s$) for the effective static magnetic field measurements.

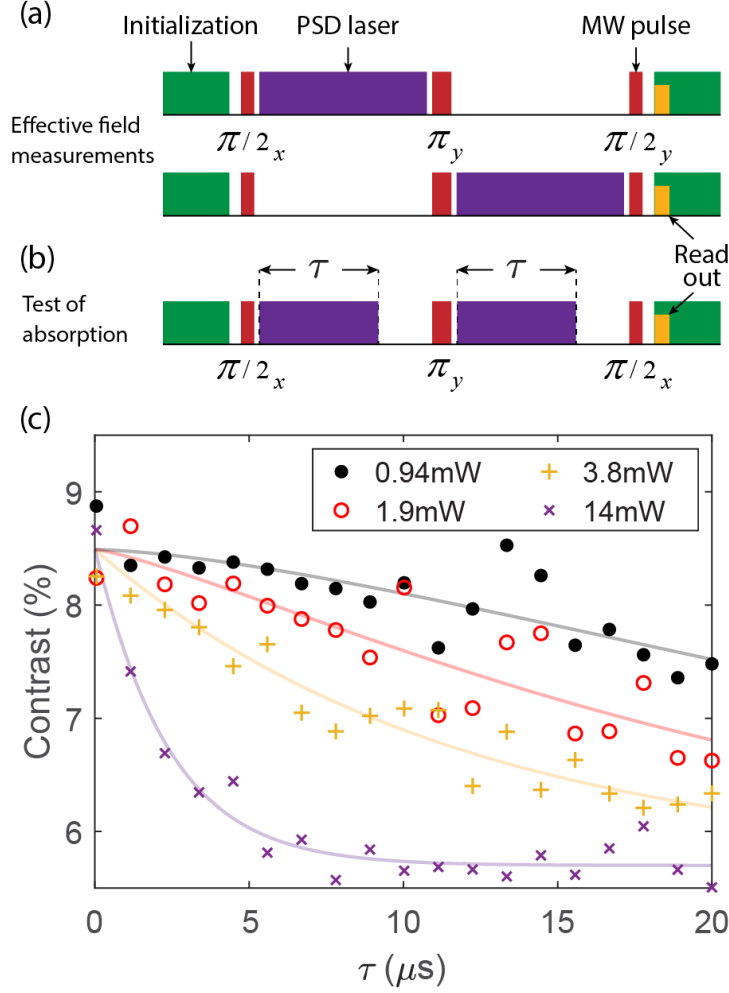


Figure 4.3. Incorporation of the PSD signal with the Hahn echo pulse sequence. (a) The PSD signal is added to the Hahn echo pulse sequence. Since this pulse sequence is only sensitive to ac magnetic fields, we add the PSD signal to one half of the sequence. Adding the PSD pulse to the first or second half induces rotations in opposite directions in the spin of the NV center which is similar to ac magnetic field with π phase difference. We extract the amplitude of the effective static magnetic field by subtracting the outcome of the two measurements. (b) Pulse sequence designed to measure the decoherence caused by the off-resonant absorption of the PSD signal. Here we add the PSD signal to both halves of the Hahn echo sequence to avoid spin rotations due to the effective static magnetic field. By increasing the pulse length τ we increase the probability of off-resonant absorption events in one measurement and observe the trend of the loss of the coherence signal. (c) The decoherence induced by the PSD signal for different PSD laser powers measured for $\lambda = 705nm$. In the case of complete decoherence the signal reaches half of the maximum contrast which is the average for the $|0\rangle$ and $|\pm 1\rangle$ states.

Illuminating NV centers with the PSD laser can affect their coherence through off-resonant absorption. To capture this effect we use the pulse sequence shown in Fig. 4.3(b). In this pulse sequence the rotations induced by the two PSD pulses cancel each other and we only see decoherence caused by the addition of the PSD laser. By increasing the pulse length τ we can study this effect. Fig. 4.3(c) shows the decoherence effect from off-resonant absorption for different laser powers. The four sets of data show how different laser powers affect the measurement outcome for $\lambda = 705nm$. The x-axis shows the length of each of the PSD pulses. As the pulse length increases the probability of off-resonant absorption also increases. The results of this measurement helps us determine the maximum laser power which does not cause significant decoherence to the NV centers. It should be mentioned that we do not observe any decoherence for wavelengths $\lambda = 785nm$ and $\lambda = 818nm$ with laser powers reaching $P = 20mW$. As the wavelength of the PSD laser gets closer to the optical resonance of the NV center at $\lambda = 637nm$ off-resonant absorption becomes stronger. The decoherence caused by this effect is noticeable for $\lambda = 730nm$ and becomes significant for $\lambda = 705nm$ as shown in Fig. 4.3(c).

4.3 Optically Induced Magnetic Field for an Ensemble of NV Centers

Figure 4.4 depicts the outcome of the effective static magnetic field measurements. The effective static magnetic field is proportional to the PSD of the optical beam. We can tune the PSD of the optical beam by controlling its power and its polarization. The PSD of the optical beam is linearly proportional to the optical power. Fig. 4.4(a)-(c) shows how the effective field depends on optical power of the PSD beam for three different wavelengths. The dashed lines show linear fits to the data for each wavelength. The linear dependence of the effective field on the optical power matches the expected behavior for PSD.

Figure 4.4(d)-(f) shows the dependence of the effective static magnetic field on the polarization of the PSD beam for three different wavelengths. The beam polarization is controlled with a QWP. The PSD of the beam has a $\vec{S}_E^{\text{obs}} \propto \sin(2\theta)\hat{z}$ dependence on the rotation angle of the QWP (θ) where \hat{z} is the direction of propagation of the beam. The dashed lines show

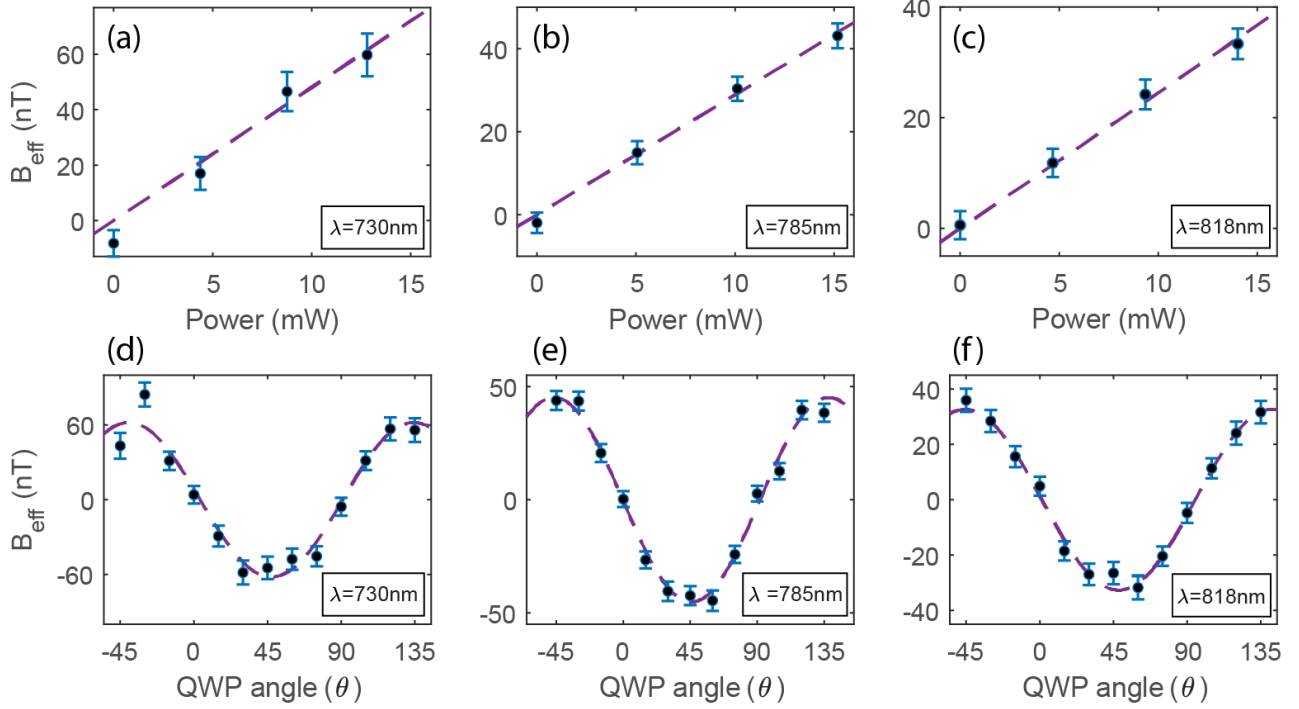


Figure 4.4. Scaling of the effective static magnetic field with beam power and polarization ellipticity. (a)-(c) Scaling of the effective field with the optical power of the PSD beam for different wavelengths. We observe linear dependence independent of the wavelength. (d)-(f) The dependence of the effective field on the ellipticity of polarization for different wavelengths. The ellipticity is controlled by rotating a QWP by an angle θ where $\theta = 0^\circ, 90^\circ$ correspond to linear polarization and $\theta = \pm 45^\circ, 135^\circ$ correspond to circular polarization. The fits to the curves are $y = \sin(2\theta)$ which is the expected dependence of PSD to QWP angle θ . We observe good agreement between theory and experiment for all wavelengths.

a fit of $\sin(2\theta)$ to the data for each wavelength. Fig. 4.4 shows that the measured effective static magnetic field is indeed proportional to the PSD for different wavelengths.

4.4 Wavelength Dependence of the Optically Induced Magnetic Field

The main goal of this chapter is to determine the wavelength dependence of the effective static magnetic field in the far off-resonant limit. This result is shown in Fig. 4.5. The measurements are performed for four different wavelengths. The main factor that affects the strength of the effective static magnetic field is the detuning between the laser wavelength and

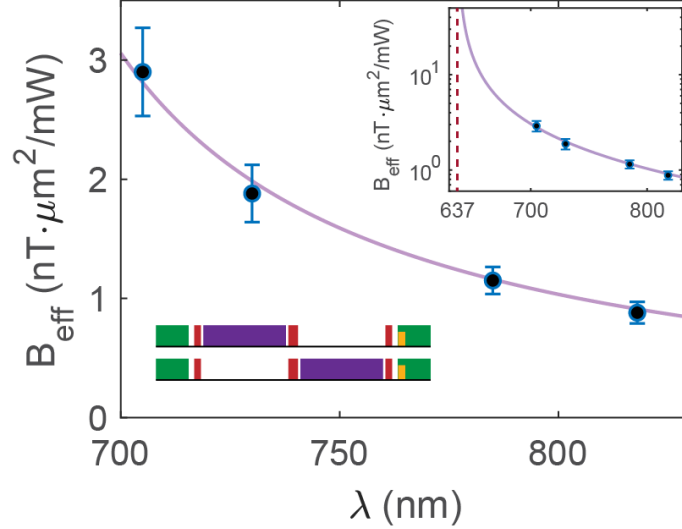


Figure 4.5. The dependence of the effective static magnetic field strength on the wavelength of the PSD beam. The rapid increase of field strength as the wavelength decreases shows a promising route for enhancing the effective static magnetic field. The inset in the top right corner shows the data in log scale along with the optical transition of the NV center at $\lambda = 637\text{nm}$. As the detuning decreases, the off-resonant absorption by the NV centers affects their coherence and the error bars become larger. To measure the data point at $\lambda = 705\text{nm}$ the sample is cooled to 30° below room temperature to lower the off-resonant absorption.

the optical transition of the NV centers. As the detuning is decreased the probability of off-resonant absorption by the NV centers increases. This absorption leads to decoherence of the NV centers and loss of sensitivity in the measurement (Fig. 4.3(c)). In these measurements the off-resonant absorption is noticeable for $\lambda = 730\text{nm}$ and becomes a dominant factor at $\lambda = 705\text{nm}$. In order to measure the effective static magnetic field for $\lambda = 705\text{nm}$ we have cooled down the sample using a thermoelectric cooler by 30° below room temperature.

The purple line in Fig. 4.5 shows a fit to the data. We have considered a fit that depends only on the wavelength λ and the detuning Δ . The fit is $y = C/\lambda\Delta$ where C is a constant and shows a good agreement with the data. The insets show the data on a log-scale and the pulse sequence for the measurements. The optical transition of the NV centers at $\lambda = 637\text{nm}$ is also shown in the inset. The fast growing nature of the effective static magnetic field for smaller detunings is captured in the inset. However, due to the off-resonant absorption,

it is not possible to probe the system for wavelengths smaller than $\lambda = 700nm$ at room temperature. Unraveling the scaling of the effective static magnetic field for near-resonant wavelengths requires rigorous studies at cryogenic temperatures.

4.5 Conclusion

In summary, we have demonstrated the optical induced static magnetic field for an ensemble of NV centers at room temperature. We show that this effective static magnetic field is proportional to the PSD of the off-resonant excitation. The decoherence induced by the off-resonant optical beam is studied for different wavelengths. Using this platform, we have characterized the wavelength dependence of the optically induced static magnetic field in the far-off-resonant regime. The results of this study can pave the way to utilize this effective magnetic field for on-chip applications and all-optical control of qubits.

5. CONCLUSIONS

In this thesis we have studied the properties of photonic spin density (PSD) in the near-field regime and demonstrated a platform for coherent light-spin-qubit interaction based on PSD. We have shown that nitrogen-vacancy (NV) centers in diamond can coherently interact with an optical beam where the interaction strength is determined by PSD in the nanoscale. We have characterized this interaction and used it to probe the PSD of an optical beam.

The first chapter provided an introduction to the field of near-field photonic spin. We presented an overview to the new findings in this field that has emerged over the past decade. Then the achievements of this field were summarized to show the need for a platform to utilize the near-field properties of PSD in quantum technologies. We then introduced NV centers in diamond as a promising tool for this purpose. Lastly, the properties and capabilities of NV centers were discussed before presenting the contributions of this thesis.

Chapter 2 focused on exploring the near-field properties of optical fields. We discussed the spin-momentum locking phenomenon for evanescent electromagnetic waves and established a connection between this phenomenon and the recent observations related to directional coupling of emission and scattering from particles into optical waveguides. We then studied the optical forces arising from this universal phenomenon and showed that the fundamental origin of recently reported non-trivial optical chiral forces is spin-momentum locking in evanescent optical fields.

In Chapter 3 we proposed and demonstrated that NV centers can be used as a quantum sensor for detecting the PSD. This demonstration includes the probing of PSD of an incident beam on a single NV center and showing that the scaling of the interaction strength with optical power and polarization of the incident beam matches that of the PSD of the beam. We also presented a rigorous theoretical analysis of this interaction. We showed that this interaction induces an effective magnetic field that affects the NV center's quantum state. To probe this optically-induced magnetic field we perform ac magnetometry at room temperature. The NV center is capable of nanometer-resolution sensing which enables deep-subwavelength probing of PSD. Furthermore, we showed that optical waveguides intrinsically carry PSD which makes this platform compatible with integrated photonic circuits. These

achievements pave the way toward quantum sensing of exotic phases of photons as well as building on-chip interfaces between optical beams and spin-qubits based on PSD.

Chapter 4 demonstrated the optically induced magnetic field for an ensemble of NV centers. The goal of this chapter is to explore the possible routes for enhancing the induced static magnetic field. We studied the effect of off-resonant absorption of the excitation beam on the coherence of the spin-qubits which limits the sensitivity of the measurements. We furthermore studied the effect of the wavelength of the excitation beam on the strength of the effective static magnetic field and the off-resonant absorption. The results of this chapter provides necessary information for further explorations of this effect.

REFERENCES

- [1] R. A. Beth, “Mechanical Detection and Measurement of the Angular Momentum of Light,” *Physical Review*, vol. 50, pp. 115–125, Jul. 1936.
- [2] C. V. Raman and S. Bhagavantam, “Experimental Proof of the Spin of the Photon,” *Nature*, vol. 129, pp. 22–23, Jan. 1932.
- [3] S. B. Wang and C. T. Chan, “Lateral optical force on chiral particles near a surface,” *Nature Communications*, vol. 5, Mar. 2014.
- [4] R. Mitsch, C. Sayrin, B. Albrecht, P. Schneeweiss, and A. Rauschenbeutel, “Quantum state-controlled directional spontaneous emission of photons into a nanophotonic waveguide,” *Nature Communications*, vol. 5, Dec. 2014.
- [5] R. P. Cameron, S. M. Barnett, and A. M. Yao, “Discriminatory optical force for chiral molecules,” *New Journal of Physics*, vol. 16, no. 1, p. 013 020, 2014.
- [6] P. V. Kapitanova, P. Ginzburg, F. J. Rodríguez-Fortuño, *et al.*, “Photonic spin Hall effect in hyperbolic metamaterials for polarization-controlled routing of subwavelength modes,” *Nature Communications*, vol. 5, Feb. 2014.
- [7] D. O’Connor, P. Ginzburg, F. J. Rodríguez-Fortuño, G. A. Wurtz, and A. V. Zayats, “Spin–orbit coupling in surface plasmon scattering by nanostructures,” *Nature Communications*, vol. 5, Nov. 2014.
- [8] J. Petersen, J. Volz, and A. Rauschenbeutel, “Chiral nanophotonic waveguide interface based on spin-orbit interaction of light,” *Science*, vol. 346, no. 6205, pp. 67–71, Oct. 2014.
- [9] M. H. Alizadeh and B. M. Reinhard, “Transverse Chiral Optical Forces by Chiral Surface Plasmon Polaritons,” *ACS Photonics*, vol. 2, no. 12, pp. 1780–1788, Dec. 2015.
- [10] A. Hayat, J. P. B. Mueller, and F. Capasso, “Lateral chirality-sorting optical forces,” *Proceedings of the National Academy of Sciences*, p. 201 516 704, Oct. 2015.
- [11] F. J. Rodríguez-Fortuño, N. Engheta, A. Martínez, and A. V. Zayats, “Lateral forces on circularly polarizable particles near a surface,” *Nature Communications*, vol. 6, no. 1, p. 8799, Nov. 2015.
- [12] S. Scheel, S. Y. Buhmann, C. Clausen, and P. Schneeweiss, “Directional spontaneous emission and lateral Casimir-Polder force on an atom close to a nanofiber,” *Physical Review A*, vol. 92, no. 4, p. 043 819, Oct. 2015.

- [13] I. Söllner, S. Mahmoodian, S. L. Hansen, *et al.*, “Deterministic photon–emitter coupling in chiral photonic circuits,” *Nature Nanotechnology*, vol. 10, no. 9, pp. 775–778, Sep. 2015.
- [14] T. Zhang, M. R. C. Mahdy, Y. Liu, *et al.*, “All-Optical Chirality-Sensitive Sorting via Reversible Lateral Forces in Interference Fields,” *ACS Nano*, vol. 11, no. 4, pp. 4292–4300, Apr. 2017.
- [15] S. Pendharker, F. Kalhor, T. V. Mechelen, *et al.*, “Spin photonic forces in non-reciprocal waveguides,” *Optics Express*, vol. 26, no. 18, pp. 23 898–23 910, Sep. 2018.
- [16] L.-P. Yang, F. Khosravi, and Z. Jacob, “Quantum spin operator of the photon,” *arXiv preprint arXiv:2004.03771*, 2020.
- [17] C. Cohen-Tannoudji, J. Dupont-Roc, and G. Grynberg, *Photons and Atoms-Introduction to Quantum Electrodynamics*. Wiley-VCH, 1997.
- [18] K. Y. Bliokh, A. Y. Bekshaev, and F. Nori, “Extraordinary momentum and spin in evanescent waves,” *Nature Communications*, vol. 5, Mar. 2014.
- [19] M. V. Berry, “Optical currents,” *Journal of Optics A: Pure and Applied Optics*, vol. 11, no. 9, p. 094 001, 2009.
- [20] M. F. Picardi, K. Y. Bliokh, F. J. Rodríguez-Fortuño, F. Alpegiani, and F. Nori, “Angular momenta, helicity, and other properties of dielectric-fiber and metallic-wire modes,” *Optica*, vol. 5, pp. 1016–1026, Aug. 2018.
- [21] T. V. Mechelen and Z. Jacob, “Universal spin-momentum locking of evanescent waves,” *Optica*, vol. 3, no. 2, pp. 118–126, Feb. 2016.
- [22] B. le Feber, N. Rotenberg, and L. Kuipers, “Nanophotonic control of circular dipole emission,” *Nature Communications*, vol. 6, Apr. 2015.
- [23] F. Le Kien, S. N. Chormaic, and T. Busch, “Chiral excitation of a single atom by a quantized single-photon pulse in a guided mode of a nanofiber,” *Physical Review A*, vol. 101, no. 6, p. 063 816, Jun. 2020.
- [24] C. Sayrin, C. Junge, R. Mitsch, *et al.*, “Nanophotonic Optical Isolator Controlled by the Internal State of Cold Atoms,” *Physical Review X*, vol. 5, no. 4, p. 041 036, Dec. 2015.
- [25] L. Du, A. Yang, A. V. Zayats, and X. Yuan, “Deep-subwavelength features of photonic skyrmions in a confined electromagnetic field with orbital angular momentum,” *Nature Physics*, vol. 15, no. 7, pp. 650–654, Jul. 2019.

- [26] T. V. Mechelen and Z. Jacob, “Photonic Dirac monopoles and skyrmions: Spin-1 quantization [Invited],” *Optical Materials Express*, vol. 9, no. 1, pp. 95–111, Jan. 2019.
- [27] T. J. Davis, D. Janoschka, P. Dreher, B. Frank, F.-J. Meyer zu Heringdorf, and H. Giessen, “Ultrafast vector imaging of plasmonic skyrmion dynamics with deep subwavelength resolution,” *Science*, vol. 368, no. 6489, eaba6415, Apr. 2020.
- [28] A. Osada, R. Hisatomi, A. Noguchi, *et al.*, “Cavity Optomagnonics with Spin-Orbit Coupled Photons,” *Physical Review Letters*, vol. 116, no. 22, p. 223 601, Jun. 2016.
- [29] A. Javadi, D. Ding, M. H. Appel, *et al.*, “Spin–photon interface and spin-controlled photon switching in a nanobeam waveguide,” *Nature Nanotechnology*, vol. 13, no. 5, pp. 398–403, May 2018.
- [30] F. Khosravi, C. L. Cortes, and Z. Jacob, “Spin photonics in 3D whispering gallery mode resonators,” *Optics Express*, vol. 27, no. 11, pp. 15 846–15 855, May 2019.
- [31] E. Will, L. Masters, A. Rauschenbeutel, M. Scheucher, and J. Volz, “Coupling a Single Trapped Atom to a Whispering-Gallery-Mode Microresonator,” *Physical Review Letters*, vol. 126, no. 23, p. 233 602, Jun. 2021.
- [32] T. van der Sar, F. Casola, R. Walsworth, and A. Yacoby, “Nanometre-scale probing of spin waves using single electron spins,” *Nature Communications*, vol. 6, no. 1, p. 7886, Aug. 2015.
- [33] L. Thiel, Z. Wang, M. A. Tschudin, *et al.*, “Probing magnetism in 2D materials at the nanoscale with single-spin microscopy,” *Science*, vol. 364, no. 6444, pp. 973–976, Jun. 2019.
- [34] S. Kolkowitz, A. Safira, A. A. High, *et al.*, “Probing Johnson noise and ballistic transport in normal metals with a single-spin qubit,” *Science*, vol. 347, no. 6226, pp. 1129–1132, Mar. 2015.
- [35] Y. Dovzhenko, F. Casola, S. Schlotter, *et al.*, “Magnetostatic twists in room-temperature skyrmions explored by nitrogen-vacancy center spin texture reconstruction,” *Nature Communications*, vol. 9, no. 1, p. 2712, Jul. 2018.
- [36] M. W. Doherty, N. B. Manson, P. Delaney, F. Jelezko, J. Wrachtrup, and L. C. L. Hollenberg, “The nitrogen-vacancy colour centre in diamond,” *Physics Reports*, vol. 528, no. 1, pp. 1–45, Jul. 2013.
- [37] B. Rodiek, M. Lopez, H. Hofer, *et al.*, “Experimental realization of an absolute single-photon source based on a single nitrogen vacancy center in a nanodiamond,” *Optica*, vol. 4, no. 1, pp. 71–76, Jan. 2017.

- [38] S. Y. Kilin, A. P. Nizovtsev, T. M. Maevskaya, A. Dräbenstedt, and J. Wrachtrup, “Spectroscopy on single N–V defect centers in diamond: Tunneling of nitrogen atoms into vacancies and fluorescence spectra,” vol. 86, no. 3, pp. 201–206, Apr. 2000.
- [39] M. Kern, J. Jeske, D. W. M. Lau, A. D. Greentree, F. Jelezko, and J. Twamley, “Optical cryocooling of diamond,” *Physical Review B*, vol. 95, no. 23, p. 235 306, Jun. 2017.
- [40] A. Batalov, C. Zierl, T. Gaebel, *et al.*, “Temporal Coherence of Photons Emitted by Single Nitrogen-Vacancy Defect Centers in Diamond Using Optical Rabi-Oscillations,” *Physical Review Letters*, vol. 100, no. 7, p. 077 401, Feb. 2008.
- [41] L. Robledo, H. Bernien, T. v. d. Sar, and R. Hanson, “Spin dynamics in the optical cycle of single nitrogen-vacancy centres in diamond,” *New Journal of Physics*, vol. 13, no. 2, p. 025 013, Feb. 2011.
- [42] D. A. Hopper, H. J. Shulevitz, and L. C. Bassett, “Spin Readout Techniques of the Nitrogen-Vacancy Center in Diamond,” *Micromachines*, vol. 9, no. 9, p. 437, Sep. 2018.
- [43] B. J. Shields, Q. P. Unterreithmeier, N. P. de Leon, H. Park, and M. D. Lukin, “Efficient Readout of a Single Spin State in Diamond via Spin-to-Charge Conversion,” *Physical Review Letters*, vol. 114, no. 13, p. 136 402, Mar. 2015.
- [44] D. M. Irber, F. Poggiali, F. Kong, *et al.*, “Robust all-optical single-shot readout of nitrogen-vacancy centers in diamond,” *Nature Communications*, vol. 12, no. 1, p. 532, Jan. 2021.
- [45] Q. Zhang, Y. Guo, W. Ji, *et al.*, “High-fidelity single-shot readout of single electron spin in diamond with spin-to-charge conversion,” *Nature Communications*, vol. 12, no. 1, p. 1529, Mar. 2021.
- [46] K. Beha, A. Batalov, N. B. Manson, R. Bratschitsch, and A. Leitenstorfer, “Optimum Photoluminescence Excitation and Recharging Cycle of Single Nitrogen-Vacancy Centers in Ultrapure Diamond,” *Physical Review Letters*, vol. 109, no. 9, p. 097 404, Aug. 2012.
- [47] N. Aslam, G. Waldherr, P. Neumann, F. Jelezko, and J. Wrachtrup, “Photo-induced ionization dynamics of the nitrogen vacancy defect in diamond investigated by single-shot charge state detection,” *New Journal of Physics*, vol. 15, no. 1, p. 013 064, Jan. 2013.
- [48] C. Schreyvogel, V. Polyakov, R. Wunderlich, J. Meijer, and C. E. Nebel, “Active charge state control of single NV centres in diamond by in-plane Al-Schottky junctions,” *Scientific Reports*, vol. 5, no. 1, pp. 1–12, Jul. 2015.

- [49] S. Karaveli, O. Gaathon, A. Wolcott, *et al.*, “Modulation of nitrogen vacancy charge state and fluorescence in nanodiamonds using electrochemical potential,” *Proceedings of the National Academy of Sciences*, vol. 113, no. 15, pp. 3938–3943, Apr. 2016.
- [50] B. Du, X.-D. Chen, S.-C. Zhang, *et al.*, “Fluorescence modulation of the nitrogen-vacancy center with competition between charge-state conversion and stimulated emission,” *JOSA B*, vol. 37, no. 5, pp. 1468–1473, May 2020.
- [51] E. Bourgeois, M. Gulka, and M. Nesladek, “Photoelectric Detection and Quantum Read-out of Nitrogen-Vacancy Center Spin States in Diamond,” *Advanced Optical Materials*, vol. 8, no. 12, p. 1902132, 2020.
- [52] J. L. Webb, A. F. L. Poulsen, R. Staacke, *et al.*, “Laser threshold magnetometry using green-light absorption by diamond nitrogen vacancies in an external cavity laser,” *Physical Review A*, vol. 103, no. 6, p. 062603, Jun. 2021.
- [53] G. Balasubramanian, P. Neumann, D. Twitchen, *et al.*, “Ultralong spin coherence time in isotopically engineered diamond,” *Nature Materials*, vol. 8, no. 5, pp. 383–387, May 2009.
- [54] J. M. Taylor, P. Cappellaro, L. Childress, *et al.*, “High-sensitivity diamond magnetometer with nanoscale resolution,” *Nature Physics*, vol. 4, no. 10, pp. 810–816, Oct. 2008.
- [55] A. Dréau, M. Lesik, L. Rondin, *et al.*, “Avoiding power broadening in optically detected magnetic resonance of single NV defects for enhanced dc magnetic field sensitivity,” *Physical Review B*, vol. 84, no. 19, p. 195204, Nov. 2011.
- [56] L. Rondin, J.-P. Tetienne, T. Hingant, J.-F. Roch, P. Maletinsky, and V. Jacques, “Magnetometry with nitrogen-vacancy defects in diamond,” *Reports on Progress in Physics*, vol. 77, no. 5, p. 056503, 2014.
- [57] S. Meiboom and D. Gill, “Modified Spin-Echo Method for Measuring Nuclear Relaxation Times,” *Review of Scientific Instruments*, vol. 29, no. 8, pp. 688–691, Aug. 1958.
- [58] B. Naydenov, F. Dolde, L. T. Hall, *et al.*, “Dynamical decoupling of a single-electron spin at room temperature,” *Physical Review B*, vol. 83, no. 8, p. 081201, Feb. 2011.
- [59] J. Choi, H. Zhou, H. S. Knowles, R. Landig, S. Choi, and M. D. Lukin, “Robust Dynamic Hamiltonian Engineering of Many-Body Spin Systems,” *Physical Review X*, vol. 10, no. 3, p. 031002, Jul. 2020.
- [60] G. Kucsko, P. C. Maurer, N. Y. Yao, *et al.*, “Nanometre-scale thermometry in a living cell,” *Nature*, vol. 500, no. 7460, pp. 54–58, Aug. 2013.

- [61] P. Neumann, I. Jakobi, F. Dolde, *et al.*, “High-Precision Nanoscale Temperature Sensing Using Single Defects in Diamond,” *Nano Letters*, vol. 13, no. 6, pp. 2738–2742, Jun. 2013.
- [62] M. Lesik, J.-P. Tetienne, A. Tallaire, *et al.*, “Perfect preferential orientation of nitrogen-vacancy defects in a synthetic diamond sample,” *Applied Physics Letters*, vol. 104, no. 11, Mar. 2014.
- [63] J. Achard, V. Jacques, and A. Tallaire, “Chemical vapour deposition diamond single crystals with nitrogen-vacancy centres: A review of material synthesis and technology for quantum sensing applications,” *Journal of Physics D: Applied Physics*, vol. 53, no. 31, p. 313001, May 2020.
- [64] I. Vlasov, V. Ralchenko, A. Khomich, S. Nistor, D. Shoemaker, and R. Khmel'nitskii, “Relative Abundance of Single and Vacancy-Bonded Substitutional Nitrogen in CVD Diamond,” *physica status solidi (a)*, vol. 181, no. 1, pp. 83–90, 2000.
- [65] J. Martin, R. Wannemacher, J. Teichert, L. Bischoff, and B. Köhler, “Generation and detection of fluorescent color centers in diamond with submicron resolution,” *Applied Physics Letters*, vol. 75, no. 20, pp. 3096–3098, Nov. 1999.
- [66] S. Pezzagna, B. Naydenov, F. Jelezko, J. Wrachtrup, and J. Meijer, “Creation efficiency of nitrogen-vacancy centres in diamond,” *New Journal of Physics*, vol. 12, no. 6, p. 065017, Jun. 2010.
- [67] X. Song, G. Wang, X. Liu, *et al.*, “Generation of nitrogen-vacancy color center in nanodiamonds by high temperature annealing,” *Applied Physics Letters*, vol. 102, no. 13, p. 133109, Apr. 2013.
- [68] A. Haque and S. Sumaiya, “An Overview on the Formation and Processing of Nitrogen-Vacancy Photonic Centers in Diamond by Ion Implantation,” *Journal of Manufacturing and Materials Processing*, vol. 1, no. 1, p. 6, Sep. 2017.
- [69] B. Naydenov, F. Reinhard, A. Lämmle, *et al.*, “Increasing the coherence time of single electron spins in diamond by high temperature annealing,” *Applied Physics Letters*, vol. 97, no. 24, p. 242511, Dec. 2010.
- [70] T. Yamamoto, T. Umeda, K. Watanabe, *et al.*, “Extending spin coherence times of diamond qubits by high-temperature annealing,” *Physical Review B*, vol. 88, no. 7, p. 075206, Aug. 2013.
- [71] D. M. Toyli, C. D. Weis, G. D. Fuchs, T. Schenkel, and D. D. Awschalom, “Chip-Scale Nanofabrication of Single Spins and Spin Arrays in Diamond,” *Nano Letters*, vol. 10, no. 8, pp. 3168–3172, Aug. 2010.

- [72] B. K. Ofori-Okai, S. Pezzagna, K. Chang, *et al.*, “Spin properties of very shallow nitrogen vacancy defects in diamond,” *Physical Review B*, vol. 86, no. 8, p. 081 406, Aug. 2012.
- [73] L. M. Pham, S. J. DeVience, F. Casola, *et al.*, “NMR technique for determining the depth of shallow nitrogen-vacancy centers in diamond,” *Physical Review B*, vol. 93, no. 4, p. 045 425, Jan. 2016.
- [74] F. Alghannam and P. Hemmer, “Engineering of Shallow Layers of Nitrogen Vacancy Colour Centres in Diamond Using Plasma Immersion Ion Implantation,” *Scientific Reports*, vol. 9, no. 1, p. 5870, Apr. 2019.
- [75] S. Kawai, H. Yamano, T. Sonoda, *et al.*, “Nitrogen-Terminated Diamond Surface for Nanoscale NMR by Shallow Nitrogen-Vacancy Centers,” *The Journal of Physical Chemistry C*, vol. 123, no. 6, pp. 3594–3604, Feb. 2019.
- [76] S. Sangtawesin, B. L. Dwyer, S. Srinivasan, *et al.*, “Origins of Diamond Surface Noise Probed by Correlating Single-Spin Measurements with Surface Spectroscopy,” *Physical Review X*, vol. 9, no. 3, p. 031 052, Sep. 2019.
- [77] Z. Yuan, M. Fitzpatrick, L. V. H. Rodgers, S. Sangtawesin, S. Srinivasan, and N. P. de Leon, “Charge state dynamics and optically detected electron spin resonance contrast of shallow nitrogen-vacancy centers in diamond,” *Physical Review Research*, vol. 2, no. 3, p. 033 263, Aug. 2020.
- [78] K. Y. Bliokh and F. Nori, “Transverse spin of a surface polariton,” *Physical Review A*, vol. 85, no. 6, p. 061 801, Jun. 2012.
- [79] T. Van Mechelen and Z. Jacob, “Universal spin-momentum locking of evanescent waves,” *Optica*, vol. 3, no. 2, p. 118, Feb. 2016.
- [80] F. L. Kien and A. Rauschenbeutel, “Negative azimuthal force of nanofiber-guided light on a particle,” *Physical Review A*, vol. 88, no. 6, p. 063 845, Dec. 2013.
- [81] K. Y. Bliokh, D. Smirnova, and F. Nori, “Quantum spin Hall effect of light,” *Science*, vol. 348, no. 6242, pp. 1448–1451, Jun. 2015.
- [82] A. Aiello, N. Lindlein, C. Marquardt, and G. Leuchs, “Transverse Angular Momentum and Geometric Spin Hall Effect of Light,” *Physical Review Letters*, vol. 103, no. 10, p. 100 401, Aug. 2009.
- [83] F. J. Rodríguez-Fortuño, G. Marino, P. Ginzburg, *et al.*, “Near-Field Interference for the Unidirectional Excitation of Electromagnetic Guided Modes,” *Science*, vol. 340, no. 6130, pp. 328–330, Apr. 2013.

- [84] A. B. Young, A. C. T. Thijssen, D. M. Beggs, *et al.*, “Polarization Engineering in Photonic Crystal Waveguides for Spin-Photon Entanglers,” *Physical Review Letters*, vol. 115, no. 15, p. 153901, Oct. 2015.
- [85] A. Aiello and P. Banzer, “Transverse spin of light for all wavefields,” *arXiv:1502.05350 [physics, physics:quant-ph]*, Feb. 2015.
- [86] A. Ashkin, “Acceleration and Trapping of Particles by Radiation Pressure,” *Physical Review Letters*, vol. 24, pp. 156–159, Jan. 1970.
- [87] A. Ashkin, J. M. Dziedzic, J. E. Bjorkholm, and S. Chu, “Observation of a single-beam gradient force optical trap for dielectric particles,” *Optics Letters*, vol. 11, no. 5, p. 288, May 1986.
- [88] M. Neugebauer, T. Bauer, A. Aiello, and P. Banzer, “Measuring the Transverse Spin Density of Light,” *Physical Review Letters*, vol. 114, no. 6, p. 063901, Feb. 2015.
- [89] G. P. Agrawal, *Fiber-Optic Communication Systems*, 3 edition. New York: Wiley-Interscience, Jun. 2002.
- [90] J. A. Shockley and J. F. Raquet, “Navigation of Ground Vehicles Using Magnetic Field Variations,” *Navigation*, vol. 61, no. 4, pp. 237–252, 2014.
- [91] K. Y. Bliokh, F. J. Rodríguez-Fortuño, F. Nori, and A. V. Zayats, “Spin-orbit interactions of light,” *Nature Photonics*, vol. 9, no. 12, p. 796, Dec. 2015.
- [92] I. Shomroni, S. Rosenblum, Y. Lovsky, O. Bechler, G. Guendelman, and B. Dayan, “All-optical routing of single photons by a one-atom switch controlled by a single photon,” *Science*, vol. 345, no. 6199, pp. 903–906, Aug. 2014.
- [93] X. Yin, P. Shi, L. Du, and X. Yuan, “Spin-resolved near-field scanning optical microscopy for mapping of the spin angular momentum distribution of focused beams,” *Applied Physics Letters*, vol. 116, no. 24, p. 241107, Jun. 2020.
- [94] L.-P. Yang and Z. Jacob, “Quantum structured light: Non-classical spin texture of twisted single-photon pulses,” *Communications Physics*, 2021.
- [95] S. Tsesses, E. Ostrovsky, K. Cohen, B. Gjonaj, N. H. Lindner, and G. Bartal, “Optical skyrmion lattice in evanescent electromagnetic fields,” *Science*, vol. 361, no. 6406, pp. 993–996, Sep. 2018.
- [96] F. Kalhor, T. Thundat, and Z. Jacob, “Universal spin-momentum locked optical forces,” *Applied Physics Letters*, vol. 108, no. 6, p. 061102, Feb. 2016.

- [97] A. V. Arzola, L. Chvátal, P. Jákl, and P. Zemánek, “Spin to orbital light momentum conversion visualized by particle trajectory,” *Scientific Reports*, vol. 9, no. 1, p. 4127, Mar. 2019.
- [98] S.-H. Gong, F. Alpegiani, B. Sciacca, E. C. Garnett, and L. Kuipers, “Nanoscale chiral valley-photon interface through optical spin-orbit coupling,” *Science*, vol. 359, no. 6374, pp. 443–447, Jan. 2018.
- [99] Z. Ji, W. Liu, S. Krylyuk, *et al.*, “Photocurrent detection of the orbital angular momentum of light,” *Science*, vol. 368, pp. 763–767, May 2020.
- [100] I. H. Deutsch and P. S. Jessen, “Quantum-state control in optical lattices,” *Phys. Rev. A*, vol. 57, pp. 1972–1986, 3 Mar. 1998.
- [101] B. B. Buckley, G. D. Fuchs, L. C. Bassett, and D. D. Awschalom, “Spin-light coherence for single-spin measurement and control in diamond,” *Science*, vol. 330, no. 6008, pp. 1212–1215, 2010.
- [102] B. Albrecht, Y. Meng, C. Clausen, A. Dureau, P. Schneeweiss, and A. Rauschenbeutel, “Fictitious magnetic-field gradients in optical microtraps as an experimental tool for interrogating and manipulating cold atoms,” *Physical Review A*, vol. 94, no. 6, p. 061401, Dec. 2016.
- [103] T. A. Wilkinson, D. J. Cottrill, J. M. Cramlet, *et al.*, “Spin-selective AC Stark shifts in a charged quantum dot,” *Applied Physics Letters*, vol. 114, no. 13, p. 133104, Apr. 2019.
- [104] C. L. Degen, F. Reinhard, and P. Cappellaro, “Quantum sensing,” *Review of Modern Physics*, vol. 89, no. 3, p. 035002, 2017.
- [105] J. R. Maze, A. Gali, E. Togan, *et al.*, “Properties of nitrogen-vacancy centers in diamond: The group theoretic approach,” *New Journal of Physics*, vol. 13, no. 2, p. 025025, 2011.
- [106] Y. Chu and M. D. Lukin, *Quantum optics with nitrogen-vacancy centers in diamond*. Oxford university press, 2017.
- [107] W. Happer and B. S. Mathur, “Effective operator formalism in optical pumping,” *Phys. Rev.*, vol. 163, pp. 12–25, 1 Nov. 1967.
- [108] M. A. Ali Ahmed, G. A. Álvarez, and D. Suter, “Robustness of dynamical decoupling sequences,” *Physical Review A*, vol. 87, no. 4, p. 042309, Apr. 2013.
- [109] V. M. Acosta, E. Bauch, M. P. Ledbetter, A. Waxman, L.-S. Bouchard, and D. Budker, “Temperature Dependence of the Nitrogen-Vacancy Magnetic Resonance in Diamond,” *Physical Review Letters*, vol. 104, no. 7, p. 070801, Feb. 2010.

- [110] R. Mitsch, C. Sayrin, B. Albrecht, P. Schneeweiss, and A. Rauschenbeutel, “Exploiting the local polarization of strongly confined light for sub-micrometer-resolution internal state preparation and manipulation of cold atoms,” *Physical Review A*, vol. 89, no. 6, p. 063 829, Jun. 2014.
- [111] P. Neumann, R. Kolesov, V. Jacques, *et al.*, “Excited-state spectroscopy of single NV defects in diamond using optically detected magnetic resonance,” *New Journal of Physics*, vol. 11, no. 1, p. 013 017, Jan. 2009.
- [112] L. J. Rogers, R. L. McMurtrie, M. J. Sellars, and N. B. Manson, “Time-averaging within the excited state of the nitrogen-vacancy centre in diamond,” *New Journal of Physics*, vol. 11, no. 6, p. 063 007, Jun. 2009.
- [113] M. J. H. Ku, T. X. Zhou, Q. Li, *et al.*, “Imaging viscous flow of the Dirac fluid in graphene,” *Nature*, vol. 583, no. 7817, pp. 537–541, Jul. 2020.
- [114] M. H. Abobeih, J. Randall, C. E. Bradley, *et al.*, “Atomic-scale imaging of a 27-nuclear-spin cluster using a quantum sensor,” *Nature*, vol. 576, no. 7787, pp. 411–415, Dec. 2019.
- [115] E. Lee-Wong, R. Xue, F. Ye, *et al.*, “Nanoscale Detection of Magnon Excitations with Variable Wavevectors Through a Quantum Spin Sensor,” *Nano Letters*, vol. 20, no. 5, pp. 3284–3290, May 2020.
- [116] N. J. McLaughlin, H. Wang, M. Huang, *et al.*, “Strong Correlation Between Superconductivity and Ferromagnetism in an Fe-Chalcogenide Superconductor,” *Nano Letters*, vol. 21, no. 17, pp. 7277–7283, Sep. 2021.
- [117] F. Kalhor, L.-P. Yang, L. Bauer, and Z. Jacob, “Quantum sensing of photonic spin density using a single spin qubit,” *Physical Review Research*, vol. 3, no. 4, p. 043 007, Oct. 2021.
- [118] L.-P. Yang and Z. Jacob, “Non-classical photonic spin texture of quantum structured light,” *Communications Physics*, vol. 4, no. 1, pp. 1–9, Sep. 2021.
- [119] L.-P. Yang, F. Khosravi, and Z. Jacob, “Quantum spin operator of the photon,” *arXiv: 2004.03771*, Dec. 2020.
- [120] L. Childress, M. V. Gurudev Dutt, J. M. Taylor, *et al.*, “Coherent Dynamics of Coupled Electron and Nuclear Spin Qubits in Diamond,” *Science*, vol. 314, no. 5797, pp. 281–285, Oct. 2006.
- [121] T. Setälä, A. Shevchenko, M. Kaivola, and A. T. Friberg, “Degree of polarization for optical near fields,” *Physical Review E*, vol. 66, p. 016 615, Jul. 2002.

- [122] A. Y. Bekshaev and M. S. Soskin, “Transverse energy flows in vectorial fields of paraxial beams with singularities,” *Optics Communications*, vol. 271, no. 2, pp. 332–348, Mar. 2007.
- [123] S. A. Maier, *Plasmonics: fundamentals and applications*. Springer, 2007.
- [124] L. D. Barron, *Molecular light scattering and optical activity*. Cambridge University Press, 2004.
- [125] I. Lindell, A. Sihvola, S. Tretyakov, and A. Viitanen, *Electromagnetic waves in chiral and bi-isotropic media*. Artech House, 1994.
- [126] T. A. Abtew, Y. Y. Sun, B.-C. Shih, P. Dev, S. B. Zhang, and P. Zhang, “Dynamic Jahn-Teller effect in the NV⁻ center in diamond,” *Phys. Rev. Lett.*, vol. 107, p. 146 403, 14 Sep. 2011.
- [127] U. Levy and Y. Silberberg, “Weakly diverging to tightly focused Gaussian beams: A single set of analytic expressions,” *JOSA A*, vol. 33, no. 10, pp. 1999–2009, Oct. 2016.

A. OPTICAL FORCE EQUATIONS

A.1 Electric and Magnetic Stokes Parameters

We define the fourth electric and magnetic Stokes parameters as [79], [121], [122]:

$$\vec{V}^e = \frac{1}{2} \sqrt{\frac{\epsilon_0}{\mu_0}} \text{Im}(\vec{E}^* \times \vec{E}) = \omega c \vec{S}_E^{\text{obs}} \quad (\text{A.1})$$

$$\vec{V}^m = \frac{1}{2} \sqrt{\frac{\mu_0}{\epsilon_0}} \text{Im}(\vec{H}^* \times \vec{H}) = \omega c \vec{S}_M^{\text{obs}} \quad (\text{A.2})$$

where the total fourth Stokes parameter is $\vec{V} = \vec{V}^e + \vec{V}^m$. This expression gives the same value as the conventional Stokes parameters for a plane wave.

A.2 Optical Force on a Chiral Particle

The optical force on chiral particle given by Wang and Chan [3] can be written in the form,

$$\langle \vec{F} \rangle = \langle \vec{F}_{gr} \rangle + \langle \vec{F}_{op} \rangle + \langle \vec{F}_{sr} \rangle, \quad (\text{A.3})$$

where $\langle \vec{F}_{gr} \rangle = \nabla U$ is the gradient force and,

$$U = 1/4(\text{Re}[\alpha_{ee}]|\vec{E}|^2 + \text{Re}[\alpha_{mm}]|\vec{H}|^2 - 2\text{Re}[\alpha_{em}]\text{Im}[\vec{H} \cdot \vec{E}^*]) \quad (\text{A.4})$$

$\langle \vec{F}_{op} \rangle$ is optical pressure force defined as:

$$\begin{aligned} \langle \vec{F}_{op} \rangle = & \frac{k_0}{c} \left(\frac{\text{Im}[\alpha_{ee}]}{\epsilon_0} + \frac{\text{Im}[\alpha_{mm}]}{\mu_0} \right) \langle \vec{N} \rangle \\ & - \text{Im}[\alpha_{em}] \nabla \times \langle \vec{N} \rangle \\ & - \frac{ck_0}{2} \left(\frac{\text{Im}[\alpha_{ee}]}{\epsilon_0} \nabla \times \vec{S}_E^{\text{obs}} + \frac{\text{Im}[\alpha_{mm}]}{\mu_0} \nabla \times \vec{S}_M^{\text{obs}} \right) \\ & + \omega^2 \text{Im}[\alpha_{em}] (\vec{S}_E^{\text{obs}} + \vec{S}_M^{\text{obs}}) \end{aligned} \quad (\text{A.5})$$

where $k_0 = \omega/c$.

$\langle \vec{F}_{sr} \rangle$ is scattering recoil force defined as:

$$\begin{aligned} \langle \vec{F}_{sr} \rangle = & -\frac{ck_0^4}{6\pi} \left\{ (\text{Re}[\alpha_{ee}\alpha_{mm}^*] + |\alpha_{em}|^2) \langle \vec{N} \rangle \right. \\ & + \sqrt{\frac{\mu_0}{\epsilon_0}} \text{Re}[\alpha_{ee}\alpha_{em}^*] \vec{V}^e + \sqrt{\frac{\epsilon_0}{\mu_0}} \text{Re}[\alpha_{mm}\alpha_{em}^*] \vec{V}^m \\ & \left. - \frac{1}{2} \text{Im}[\alpha_{ee}\alpha_{mm}^*] \text{Im}[\vec{E} \times \vec{H}^*] \right\}. \end{aligned} \quad (\text{A.6})$$

A.3 Polarizability of the Chiral Particle

The polarizability of the particle is an approximate value for a spherical particle of a volume $V = 100nm^3$ [123]. For such a particle the polarizability matrix is,

$$\begin{bmatrix} \alpha_{ee} & i\alpha_{em} \\ -i\alpha_{me} & \alpha_{mm} \end{bmatrix} = \begin{bmatrix} 1.2 + i0.1 & i0.01 \\ -i0.01 & 0.0002 \end{bmatrix} \times 10^{-24} \quad (\text{A.7})$$

The relative permittivity of the particle is assumed to be $\epsilon_r = 3 + i 0.28$ and the electric-electric polarizability factor α_{ee} is calculated using the formula [123] $\alpha_{ee} = 3V(\epsilon_r - \epsilon_m)/(\epsilon_r + 2\epsilon_m)$, where $\epsilon_m = 1$ is the relative permittivity of the vacuum. The chirality factor is calculated using the parameters of Hexahelicene molecule [5], [124] at wavelength $\lambda = 5\mu m$. The density of the particle is approximated with that of water.

The magnetic polarizability α_{mm} is chosen such to satisfy the condition [125] $\alpha_{ee}\alpha_{mm} \geq \alpha_{em}\alpha_{me}$. For a helical particle $\alpha_{ee}\alpha_{mm} = \alpha_{em}\alpha_{me}$.

B. CALCULATIONS FOR PHOTONIC SPIN DENSITY-INDUCED EFFECTIVE STATIC MAGNETIC FIELD

We now show how to calculate the effective static magnetic field induced by far off-resonant electric dipole transitions. Virtual electric dipole transitions will induce energy shifts in the ground states, which can be described by an effective Hamiltonian $H_{\text{shift}} = \sum_i \delta_i |i\rangle\langle i|$ with the shift [100], [107],

$$\delta_i = \frac{1}{4\hbar^2} \sum_f \frac{|\langle f | \vec{d} | i \rangle \cdot \vec{E}(\vec{r}, t)|^2}{\Delta_{if} + \Gamma_f^2/4\Delta_{if}}. \quad (\text{B.1})$$

Here, $|i\rangle$ and $|f\rangle$ are the initial and final states of the possible transitions in an NV center as shown in Fig. B.1, Δ_{ij} is the difference between the center frequency of the off-resonant excitation (ω_0) and the resonance frequency of the transition (ω_{ij}), Γ_f is the spontaneous decay rate of the final state, and $\vec{E}(\vec{r}, t)$ is the electric field of the excitation at the position of the NV (\vec{r}). We choose the detuning to be much larger than the spontaneous decay rate. Thus, the Γ_f^2 term will be neglected. We show that the energy difference in the states $\{|0\rangle, |\pm 1\rangle\}$ induced by the off-resonance light functions as an effective static magnetic field for the NV ground-state spin.

B.1 Energy Structure of NV Center

To calculate this effective static magnetic field, we first give the eigenenergy spectrum and the possible transitions in the NV center. We only consider the six triplet excited states and neglect the other singlet states [105], [106], as the electric dipole transitions do not change spin states. For convenience, we choose a basis set, which is both spin- and orbital angular momentum resolved:

$$|E_L\rangle = \frac{1}{\sqrt{2}} (|E_y\rangle - i|E_x\rangle) = \frac{i}{2} [|a_1\rangle |e_+\rangle - |e_+\rangle |a_1\rangle] \otimes (|\uparrow\downarrow\rangle + |\downarrow\uparrow\rangle), \quad (\text{B.2})$$

$$|E_R\rangle = \frac{1}{\sqrt{2}} (|E_y\rangle + i|E_x\rangle) = \frac{i}{2} [|a_1\rangle |e_-\rangle - |e_-\rangle |a_1\rangle] \otimes (|\uparrow\downarrow\rangle + |\downarrow\uparrow\rangle), \quad (\text{B.3})$$

$$|E_{\downarrow}\rangle = \frac{1}{\sqrt{2}} (|E_2\rangle + |E_1\rangle) = \frac{1}{\sqrt{2}} (|a_1\rangle |e_{-}\rangle - |e_{-}\rangle |a_1\rangle) \otimes |\downarrow\downarrow\rangle, \quad (\text{B.4})$$

$$|E_{\uparrow}\rangle = \frac{1}{\sqrt{2}} (|E_2\rangle - |E_1\rangle) = \frac{1}{\sqrt{2}} (|a_1\rangle |e_{+}\rangle - |e_{+}\rangle |a_1\rangle) \otimes |\uparrow\uparrow\rangle, \quad (\text{B.5})$$

$$|A_{\uparrow}\rangle = \frac{1}{\sqrt{2}} (|A_2\rangle + |A_1\rangle) = \frac{1}{\sqrt{2}} (|a_1\rangle |e_{-}\rangle - |e_{-}\rangle |a_1\rangle) \otimes |\uparrow\uparrow\rangle, \quad (\text{B.6})$$

$$|A_{\downarrow}\rangle = \frac{1}{\sqrt{2}} (|A_2\rangle - |A_1\rangle) = \frac{1}{\sqrt{2}} (|a_1\rangle |e_{+}\rangle - |e_{+}\rangle |a_1\rangle) \otimes |\downarrow\downarrow\rangle, \quad (\text{B.7})$$

where $|a_1\rangle$, $|e_x\rangle$, and $|e_y\rangle$ are the orbital states of the NV center and $|e_{\pm}\rangle = \mp (|e_x\rangle \pm i |e_y\rangle) / \sqrt{2}$.

The ground states are given by,

$$|-1\rangle = \frac{1}{\sqrt{2}} (|e_x e_y\rangle - |e_y e_x\rangle) \otimes |\downarrow\downarrow\rangle, \quad (\text{B.8})$$

$$|0\rangle = \frac{1}{2} (|e_x e_y\rangle - |e_y e_x\rangle) \otimes (|\uparrow\downarrow\rangle + |\downarrow\uparrow\rangle), \quad (\text{B.9})$$

$$|+1\rangle = \frac{1}{\sqrt{2}} (|e_x e_y\rangle - |e_y e_x\rangle) \otimes |\uparrow\uparrow\rangle. \quad (\text{B.10})$$

We note that this normalization is different from Refs. [105], [106]. The possible electric dipole transition are shown in Fig. B.1.

The effective excited-state Hamiltonian of the NV center is given by Eq. (3.1). The optical gap $\hbar\omega_{ge} \approx 1.945$ eV (637 nm) between the ground states and the excited states (see Fig. B.1) has not been shown in H_{ES} . The off-diagonal coupling between these six excited states does not change this virtual transition-induced effective static magnetic field. Thus, we have omitted those off-diagonal coupling terms and the excited-state Hamiltonian is of diagonal form $H_{\text{ES}} = E_j |j\rangle\langle j|$ where $|j\rangle \in \{|A_{\uparrow}\rangle, |A_{\downarrow}\rangle, |E_R\rangle, |E_L\rangle, |E_{\uparrow}\rangle, |E_{\downarrow}\rangle\}$.

B.2 Energy Shifts and Effective Magnetic Field for the Ground-state Spin

We now also give the transition elements of the electric dipole transitions in the NV center. As the upper basis is based on the two-hole picture, the electric dipole operator of the NV is given by

$$\vec{d} = e(\vec{r}_1 + \vec{r}_2), \quad (\text{B.11})$$

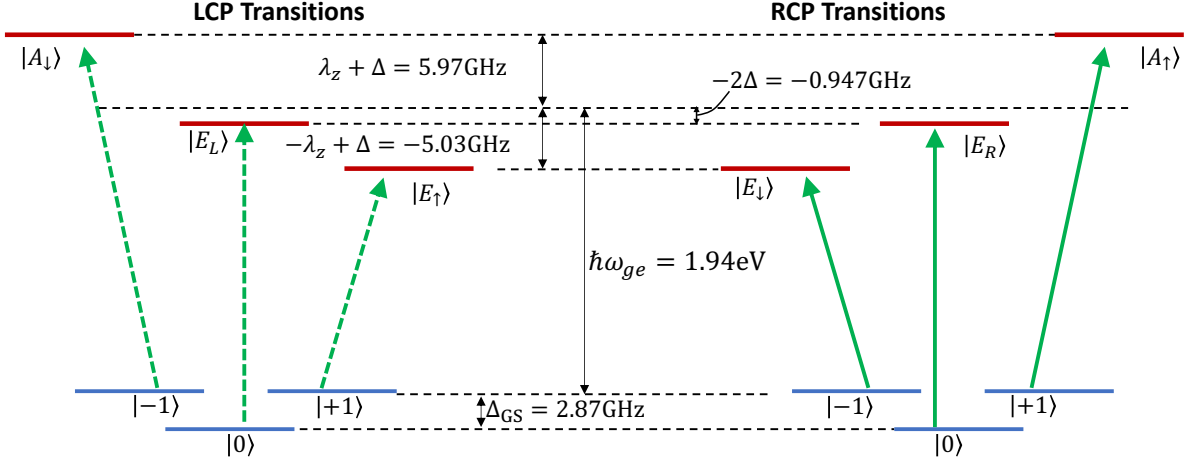


Figure B.1. Schematic of energy levels of the NV center. Here, there are no external magnetic field and strain. Left and right panels show the possible transitions induced by left circularly polarized (LCP) and right circularly polarized (RCP) lights.

Table B.1. Selection rules for optical transitions between the triplet ground states and the triplet excited states. We note that any transition connected with circularly polarized light can also be stimulated with linearly polarized lights. But the corresponding transition strength will be smaller.

Polarization	$ A_\uparrow\rangle$	$ A_\downarrow\rangle$	$ E_R\rangle$	$ E_L\rangle$	$ E_\uparrow\rangle$	$ E_\downarrow\rangle$
$ -1\rangle$		LCP				RCP
$ 0\rangle$			RCP	LCP		
$ +1\rangle$	RCP				LCP	

where \vec{r}_1 and \vec{r}_2 are the position operator of the two holes. According to the symmetry of the orbits shown in [106], the nonzero elements of the dipolar transitions are

$$e \langle e_x | r_x | e_x \rangle = -e \langle e_y | r_y | e_y \rangle = e \langle e_y | r_y | e_x \rangle \neq 0. \quad (\text{B.12})$$

and

$$e \langle a_1 | r_x | e_x \rangle = e \langle a_1 | r_y | e_y \rangle \equiv d_0 \neq 0. \quad (\text{B.13})$$

The possible transitions and the corresponding transition strength can be easily obtained by the transition element. The nonzero transition elements are follows:

$$\langle E_L | \vec{d} | 0 \rangle = d_0 \vec{e}_R, \quad \langle E_R | \vec{d} | 0 \rangle = d_0 \vec{e}_L, \quad (\text{B.14})$$

$$\langle A_\uparrow | \vec{d} | +1 \rangle = id_0 \vec{e}_L, \quad \langle E_\uparrow | \vec{d} | +1 \rangle = id_0 \vec{e}_R \quad (\text{B.15})$$

$$\langle A_\downarrow | \vec{d} | -1 \rangle = id_0 \vec{e}_R, \quad \langle E_\downarrow | \vec{d} | -1 \rangle = id_0 \vec{e}_L, \quad (\text{B.16})$$

where we have defined the unit vectors

$$\vec{e}_L = (\vec{e}_x + i\vec{e}_y)/\sqrt{2}, \quad \vec{e}_R = (\vec{e}_x - i\vec{e}_y)/\sqrt{2}. \quad (\text{B.17})$$

Using the identities of the unit vectors $\vec{e}_R \cdot \vec{e}_R^* = \vec{e}_R \cdot \vec{e}_L = 1$ and $\vec{e}_R \cdot \vec{e}_R = \vec{e}_L \cdot \vec{e}_L = 0$, one can easily obtain the selection rules in Table B.1.

The value of the transition element can be obtained from the life times of the triplet excited states:

$$\tau_{\text{NV}} = \frac{1}{\gamma_{\text{NV}}} \approx \left(\frac{\omega_{\text{eg}}^3 d_0^2}{3\pi\hbar\epsilon_0 c^3} \right)^{-1}. \quad (\text{B.18})$$

In this work, the lifetime of the NV center is taken as $\tau_{\text{NV}} = 15$ ns. Then, we have $d_0 \approx 2.485 \times 10^{-29}$ C · m.

For simplicity, we first consider the case where the NV center axis is aligned with the propagating direction of the off-resonant excitation ($+\hat{z}$). The energy shifts in the ground states sub-levels under a LCP or RCP excitation field are given by

$$\delta_{-1,L} = \frac{1}{4\hbar^2} \frac{d_0^2 \Delta_{-1,A_\downarrow}}{\Delta_{-1,A_\downarrow}^2 + \Gamma^2/4} |\vec{E}(\vec{r})|^2, \quad \delta_{-1,R} = \frac{1}{4\hbar^2} \frac{d_0^2 \Delta_{-1,E_\downarrow}}{\Delta_{-1,E_\downarrow}^2 + \Gamma^2/4} |\vec{E}(\vec{r})|^2, \quad (\text{B.19})$$

$$\delta_{0,L} = \frac{1}{4\hbar^2} \frac{d_0^2 \Delta_{0,E_L}}{\Delta_{0,E_L}^2 + \Gamma^2/4} |\vec{E}(\vec{r})|^2, \quad \delta_{0,R} = \frac{1}{4\hbar^2} \frac{d_0^2 \Delta_{0,E_R}}{\Delta_{0,E_R}^2 + \Gamma^2/4} |\vec{E}(\vec{r})|^2, \quad (\text{B.20})$$

$$\delta_{+1,L} = \frac{1}{4\hbar^2} \frac{d_0^2 \Delta_{+1,E_\uparrow}}{\Delta_{+1,E_\uparrow}^2 + \Gamma^2/4} |\vec{E}(\vec{r})|^2, \quad \delta_{+1,R} = \frac{1}{4\hbar^2} \frac{d_0^2 \Delta_{+1,A_\uparrow}}{\Delta_{+1,A_\uparrow}^2 + \Gamma^2/4} |\vec{E}(\vec{r})|^2. \quad (\text{B.21})$$

where the detunings are given by

$$\Delta_{-1,j} = \omega_0 - (\omega_{ge} + E_j + \gamma_{NV}B), \quad (\text{B.22})$$

$$\Delta_{0,j} = \omega_0 - (\omega_{ge} + E_j + \Delta_{GS}), \quad (\text{B.23})$$

$$\Delta_{+1,j} = \omega_0 - (\omega_{ge} + E_j - \gamma_{NV}B). \quad (\text{B.24})$$

C. EFFECTIVE STATIC MAGNETIC FIELD FOR PROBE QUBITS

In the experiment, we choose two ground state sub-levels to form a qubit to detect the relative energy shift between them. The effective static magnetic fields for the three possible qubits are defined as

$$B_{01,L} = \frac{\delta_{+1,L} - \delta_{0,L}}{\gamma_{NV}}, \quad B_{01,R} = \frac{\delta_{+1,R} - \delta_{0,R}}{\gamma_{NV}}, \quad (\text{C.1})$$

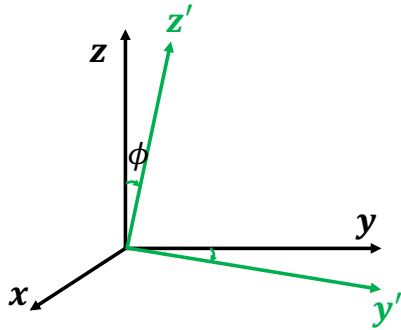
$$B_{-10,L} = \frac{\delta_{0,L} - \delta_{-1,L}}{\gamma_{NV}}, \quad B_{-10,R} = \frac{\delta_{0,R} - \delta_{-1,R}}{\gamma_{NV}} \quad (\text{C.2})$$

$$B_{-11,L} = \frac{\delta_{+1,L} - \delta_{-1,L}}{2\gamma_{NV}}, \quad B_{-11,R} = \frac{\delta_{+1,R} - \delta_{-1,R}}{2\gamma_{NV}}. \quad (\text{C.3})$$

We note that the amplitude of the effective static magnetic field is linearly proportional to the off-resonant laser power. We can also tune the effective magnetic field via changing the polarization of the laser. The polarization unit vector of an arbitrary polarized light can be expanded as

$$\vec{e} = \vec{e}_L \cos\left(\theta - \frac{\pi}{4}\right) + \vec{e}_R \sin\left(\theta - \frac{\pi}{4}\right), \quad (\text{C.4})$$

where the angle $\theta \in [0, 2\pi)$ is the rotation angle of a QWP. In addition, in the experiment the NV center axis makes an angle ϕ with the propagating direction of the off-resonant beam.



$$\begin{aligned} \mathbf{e}'_x &= \mathbf{e}_x \\ \mathbf{e}'_y &= \mathbf{e}_y \cos \phi - \mathbf{e}_z \sin \phi \\ \mathbf{e}'_z &= \mathbf{e}_z \cos \phi + \mathbf{e}_y \sin \phi \end{aligned}$$

Figure C.1. Transformation between the NV center coordinate frame and the off-resonant beam coordinate frame.

We need to transform the LCP and RCP unit vectors in the NV center coordinate frame ($x'y'z'$) into the excitation beam coordinate frame (xyz) as shown in Fig. C.1,

$$\vec{e}'_L = \frac{1}{2}\vec{e}_L(\cos\phi + 1) + \frac{1}{2}\vec{e}_R(\cos\phi - 1) + \frac{1}{\sqrt{2}}\vec{e}_z \sin\phi, \quad (\text{C.5})$$

$$\vec{e}'_R = \frac{1}{2}\vec{e}_R(\cos\phi + 1) + \frac{1}{2}\vec{e}_L(\cos\phi - 1) + \frac{1}{\sqrt{2}}\vec{e}_z \sin\phi. \quad (\text{C.6})$$

In this case, the three effective magnetic fields are given by

$$B_{01} = B_{01,L}|\vec{e} \cdot \vec{e}'_L|^2 + B_{01,R}|\vec{e} \cdot \vec{e}'_R|^2, \quad (\text{C.7})$$

$$B_{-10} = B_{-10,L}|\vec{e} \cdot \vec{e}'_L|^2 + B_{-10,R}|\vec{e} \cdot \vec{e}'_R|^2, \quad (\text{C.8})$$

$$B_{-11} = B_{-11,L}|\vec{e} \cdot \vec{e}'_L|^2 + B_{-11,R}|\vec{e} \cdot \vec{e}'_R|^2. \quad (\text{C.9})$$

Using the fact that $\delta_{-1,L} = \delta_{+1,R}$ and $\delta_{-1,R} = \delta_{+1,L}$, we can rewrite B_{-11} as

$$B_{-11} = \frac{\delta_{+1,L} - \delta_{+1,R}}{2\gamma_{NV}|\vec{E}(\vec{r})|^2} \{-i[\vec{E}^*(\vec{r}) \times \vec{E}(\vec{r})] \cdot \vec{\hat{n}}\} \quad (\text{C.10})$$

$$= \frac{\omega_0(\delta_{+1,L} - \delta_{+1,R})}{\epsilon\gamma_{NV}|\vec{E}(\vec{r})|^2} \{\vec{S} \cdot \vec{\hat{n}}\} \quad (\text{C.11})$$

$$\approx -\frac{\omega_0 d_0^2 \lambda_z}{\hbar^2 \epsilon \gamma_{NV} \Delta_{+1,A\uparrow} \Delta_{+1,E\uparrow}} \{\vec{S} \cdot \vec{\hat{n}}\}. \quad (\text{C.12})$$

Here ϵ is the permittivity of diamond, $\vec{S} = -(i\epsilon/4\omega_0)[\vec{E}^* \times \vec{E} + \vec{H}^* \times \vec{H}] = -(i\epsilon/2\omega_0)\vec{E}^* \times \vec{E}$ is the photonic spin density in the single-frequency limit, and $\vec{\hat{n}}$ is the direction of the NV center. We have also used the relation,

$$\vec{e}^* \times \vec{e} = i \left[\cos^2 \left(\theta - \frac{\pi}{4} \right) - \sin^2 \left(\theta - \frac{\pi}{4} \right) \right] \vec{e}_z = i \sin(2\theta) \vec{e}_z. \quad (\text{C.13})$$

In the far off-resonant case $\Delta_{+1,A\uparrow} \approx \Delta_{+1,E\uparrow} = \Delta$. In this case the denominator is only determined by the frequency of the off-resonant beam and the spin-orbit coupling factor in the excited state. B_{eff} can be written in the following form,

$$B_{eff} = B_{-11} = -\frac{\omega_0 d_0^2 \lambda_z}{\hbar^2 \epsilon \gamma_{NV} \Delta^2} (\vec{S}_E \cdot \vec{\hat{n}}) = C(\vec{S}_E \cdot \vec{\hat{n}}) \quad (\text{C.14})$$

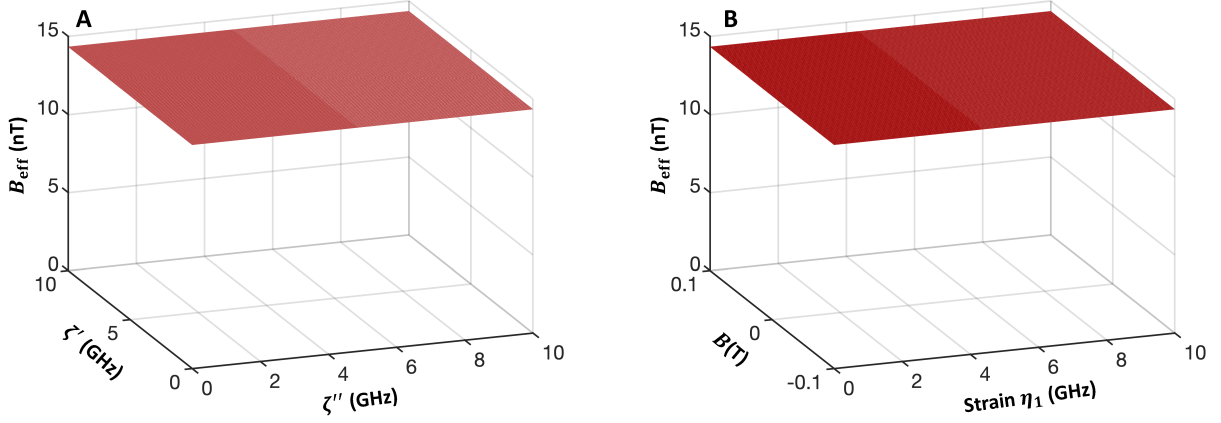


Figure C.2. (a) The effective static magnetic field B_{eff} experienced by the qubit formed by $| - 1 \rangle$ and $| + 1 \rangle$ as a function of spin-spin-induced zero-field splitting ζ' and ζ'' . (b) The effective static magnetic field B_{eff} as a function of the external magnetic field B and the strain η_1 . Here, the other parameters are taken as $\lambda_z/2\pi = 5.5$ GHz, $\Delta_{\text{es}}/2\pi = 1.42/3$ GHz, the center wavelength of the right-handed circularly polarized excitation is $\lambda_0 = 800$ with laser power 1mW.

where C is a constant.

C.1 Influence of Coupling between NV Center's Excited-state Sublevels on the Effective Static Magnetic Field

In this subsection, we show that the off-diagonal coupling in the excited-state sublevels will not affect the effective static magnetic field. The full Hamiltonian for the excited state of the NV center in the set of basis $\{|A_\uparrow\rangle, |A_\downarrow\rangle, |E_R\rangle, |E_L\rangle, |E_\uparrow\rangle, |E_\downarrow\rangle\}$ is given by [106],

$$H_{\text{ES}} = \begin{bmatrix} \gamma_{\text{NV}}B + \Delta_{\text{es}} + \lambda_z & \zeta' & 0 & 0 & -(\eta_1 + i\eta_2) & 0 \\ \zeta' & -\gamma_{\text{NV}}B + \Delta_{\text{es}} + \lambda_z & 0 & 0 & 0 & -(\eta_1 - i\eta_2) \\ 0 & 0 & -2\Delta_{\text{es}} & -(\eta_1 + i\eta_2) & 0 & -\zeta'' \\ 0 & 0 & -(\eta_1 - i\eta_2) & -2\Delta_{\text{es}} & \zeta'' & 0 \\ -(\eta_1 - i\eta_2) & 0 & 0 & \zeta'' & \gamma_{\text{NV}}B + \Delta_{\text{es}} - \lambda_z & 0 \\ 0 & -(\eta_1 + i\eta_2) & -\zeta'' & 0 & 0 & -\gamma_{\text{NV}}B + \Delta_{\text{es}} - \lambda_z \end{bmatrix}, \quad (\text{C.15})$$

where ζ' and ζ'' are the spin-spin-induced off-diagonal zero-field splitting (ZFS). In an experiment, we can easily tune the Zeeman splitting with an external magnetic field. The strain η_1 , η_2 can also be tuned by adding an electric field. These off-diagonal terms have been neglected in Eq. (3.1) because they do not change the effective static magnetic field induced by PSD as we show in this subsection.

For a given set of parameters, we can diagonalize the Hamiltonian (C.15) to obtain the eigenstates and the corresponding eigenvalues:

$$H_{\text{ES}} |m\rangle = E_m |m\rangle, m = 1, \dots, 6. \quad (\text{C.16})$$

Here, we only take the effective static magnetic field induced by an RCP light as an example.

The energy shifts in the ground-state sublevels are given by

$$\delta_{-1,R} = \frac{d_0^2}{4\hbar^2} \sum_m \frac{\langle E_\downarrow | m \rangle \langle m | E_\downarrow \rangle \Delta_{-1,m}}{\Delta_{-1,m}^2 + \Gamma^2/4} |\vec{E}(\vec{r})|^2, \quad (\text{C.17})$$

$$\delta_{0,R} = \frac{d_0^2}{4\hbar^2} \sum_m \frac{\langle E_R | m \rangle \langle m | E_R \rangle \Delta_{0,m}}{\Delta_{0,m}^2 + \Gamma^2/4} |\vec{E}(\vec{r})|^2, \quad (\text{C.18})$$

$$\delta_{+1,R} = \frac{d_0^2}{4\hbar^2} \sum_m \frac{\langle A_\uparrow | m \rangle \langle m | A_\uparrow \rangle \Delta_{+1,m}}{\Delta_{+1,m}^2 + \Gamma^2/4} |\vec{E}(\vec{r})|^2, \quad (\text{C.19})$$

where

$$\Delta_{-1,m} = \omega_0 - (\omega_{ge} + E_m + \gamma_{\text{NV}}B), \quad (\text{C.20})$$

$$\Delta_{0,m} = \omega_0 - (\omega_{ge} + E_m + \Delta_{\text{GS}}), \quad (\text{C.21})$$

$$\Delta_{+1,m} = \omega_0 - (\omega_{ge} + E_m - \gamma_{\text{NV}}B). \quad (\text{C.22})$$

The effective static magnetic field can be defined via Eqs. (C.1)-(C.3).

In the case of applying a far off-resonant beam with center wavelength $\lambda_0 = 800$ nm, an NV center is not pumped to the excited state. As shown in Fig. C.2(a), the effective static magnetic field B_{eff} induced by a circularly polarized light is almost independent of the amplitude of the off-diagonal ZFS terms, ζ'' and ζ'' , which mix the excited-state sublevels.

In Fig. C.2(b), we show that in the far off-resonant case, the effective static magnetic field B_{eff} is also independent of the external magnetic field and strain η .

In this subsection we showed numerically that coupling between the excited-state sub-levels does not change the energy shift experienced by the ground-state energy levels due to a far off-resonant excitation. A similar argument also applies to the dynamic Jahn-Teller effect in the NV center's electronic excited states [126]. Therefore, it is possible to measure a PSD dependent effective static magnetic field while resolving NV center's excited-state energy levels at room temperature is not possible.

D. EXPERIMENTAL SETUP

A schematic of the experimental setup is shown in Fig. D.1(a). The setup comprises an NV center and three main beam paths. The NV center [Fig. D.1(b)] is on an AFM tip and is implanted 10nm deep into the surface of the tip. The tip is purchased from QZabre LLC. The second-order correlation measurement for the single NV center is shown in Fig. D.1(b). A magnet breaks the degeneracy of $|\pm 1\rangle$ states by applying a magnetic field $B_{bias} \approx 1.1mT$. An antenna made of a 15 μm -thick tungsten wire delivers a MW signal to the NV center to induce Rabi oscillations [Fig. D.1(c)]. Figure D.2 shows the instrument response function (IRF) for the detection system. IRF is measured for two wavelengths spanning the PL spectrum of NV centers. For each wavelength the IRF is smaller than 40ps. However, the

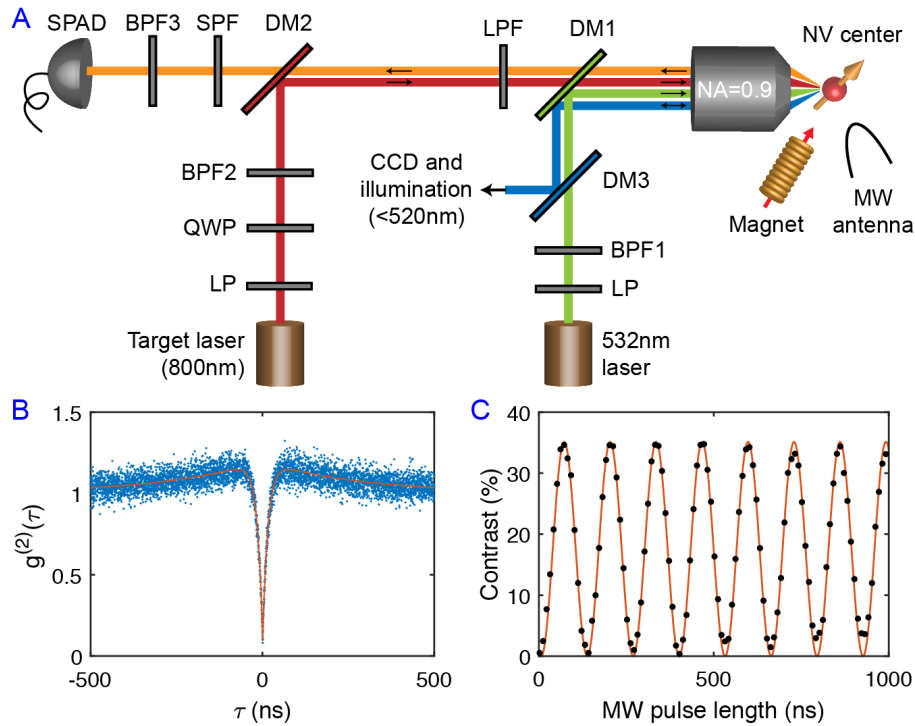


Figure D.1. Schematic of the experimental setup. (a) Schematic of the setup showing the beam paths and filters. (b) Second-order correlation measurement showing that the AFM tip contains a single NV center. (c) Rabi oscillations showing the interaction of the microwave beam (MW) with the NV center. LP, linear polarizer; DM, dichroic mirror; BPF, band-pass filter; LPF, long-pass filter; SPF, short-pass filter; QWP, quarter-wave plate.

chromatic dispersion of a fiber coupler used to deliver the PL signal to SPADs causes a 37ps relative delay between the detection peaks for the two wavelengths. The total width of the IRF including this dispersion delay is $W_{IRF} \approx 75ps \pm 5$.

A 532nm laser is used for excitation and readout of the state of the NV center. The beam is chopped with an AOM for pulsed measurements. After the linear polarizer the beam is coupled to a polarization maintaining (PM) fiber. The output of the fiber is collimated and filtered with a band-pass filter (BPF) (Thorlabs FLH532-10).

The target laser is a TTL controlled laser diode module (Power Technology Inc. PMT150). The beam is coupled into a PM fiber after a linear polarizer. The output of the fiber is collimated and goes through a quarter-wave plate before being filtered with a BPF (FBH800-10). Due to reflection from a dichroic mirror, the polarization of the beam has an ellipticity of $\varepsilon = 1.08$ before entering the objective lens when the QWP is at its optimal angle.

The photoluminescence signal from the NV center is filtered with a long-pass filter (Semrock BLP02-561-R), a short-pass filter (Semrock SP01-785RU), and a BPF (Semrock FF01-709/167). Three dichroic mirrors (DM) combine and separate the beams; DM1, Thorlabs DMLP550R; DM2, Semrock FF750-SDi02; DM3, Semrock FF520-Di02. The PL signal is detected by a Micro Photon Devices SPAD. For measuring $g^{(2)}$ the signal is coupled to a fiber optic beam splitter and is detected with two SPADs.

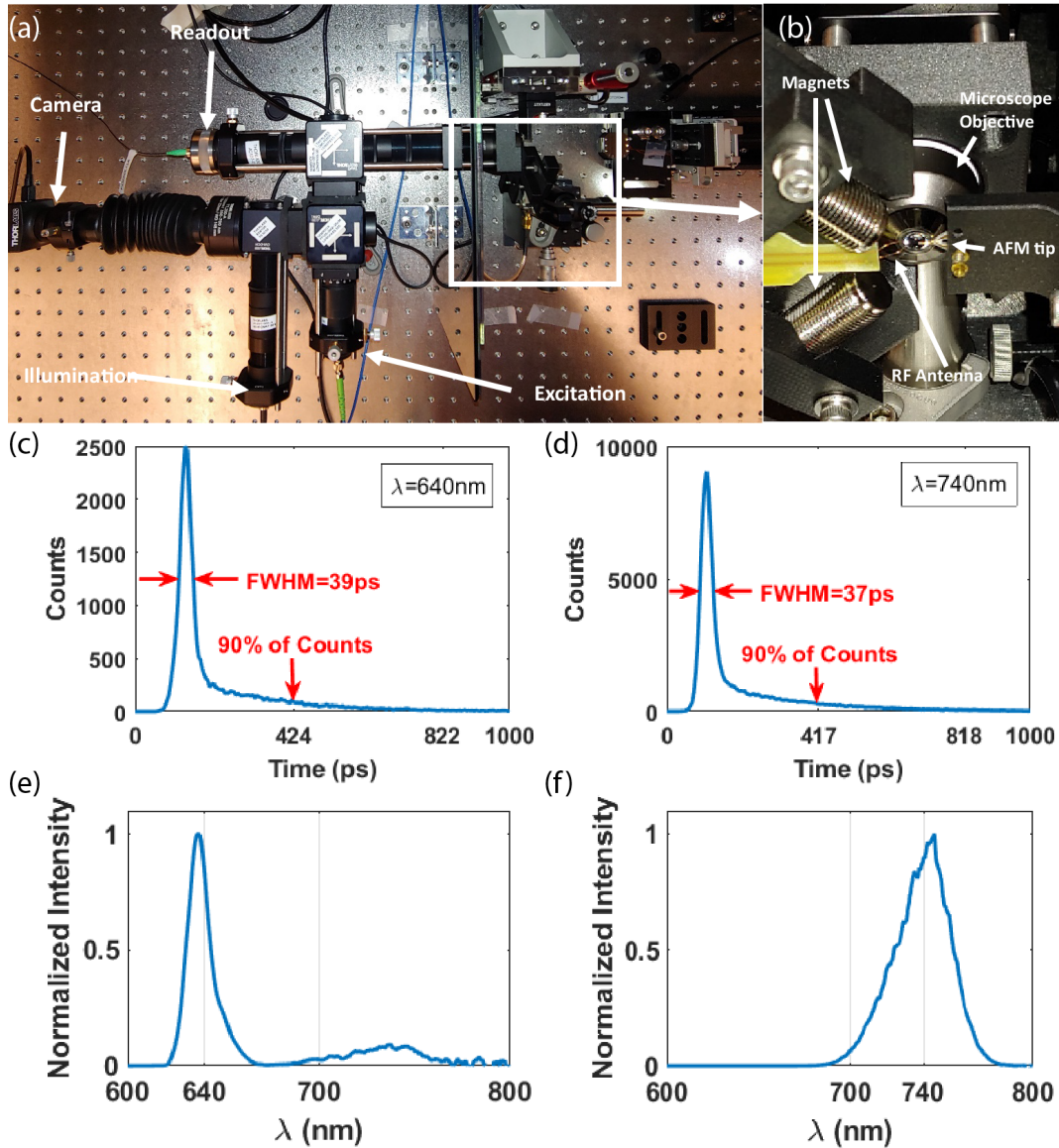


Figure D.2. Instrument response function of the detection system. (a)-(b) Pictures of the experimental setup showing the key components. (c)-(d) The response function of the detection system for two different wavelengths covering the PL spectrum of NV center. The excitation signal is a femtosecond pulsed laser. (e)-(f) The spectra for the excitation signals used in panels (c) and (d) to measure the instrument response function.

E. PULSE SEQUENCE

Here we will explain how the measurement is performed in details. Depending on which transition the MW field is resonant to ($|0\rangle$ to $|+1\rangle$ or $|0\rangle$ to $|-1\rangle$) we choose those two states as a two-level system. The pulse sequence shown in Fig. 3.3 starts with initializing the NV center in $|0\rangle$ state. Then a series of π and $\pi/2$ pulses manipulate the state of the NV center to prepare the NV center for interaction and readout and to increase the coherence time. The state after each pulse is calculated using the following rotation matrices,

$$R_x(\theta) = \begin{bmatrix} \cos\frac{\theta}{2} & -i\sin\frac{\theta}{2} \\ -i\sin\frac{\theta}{2} & \cos\frac{\theta}{2} \end{bmatrix}$$

$$\text{and } R_y(\theta) = \begin{bmatrix} \cos\frac{\theta}{2} & -\sin\frac{\theta}{2} \\ \sin\frac{\theta}{2} & \cos\frac{\theta}{2} \end{bmatrix},$$

where $\theta = \pi/2$ ($\theta = \pi$) for $\pi/2$ pulse (π pulse).

We show the calculations for $|0\rangle$ to $|+1\rangle$ transition here. The sequence starts with initializing the NV center into $|0\rangle$ state. Then a $\pi/2$ pulse rotates the spin into a superposition state and a series of π pulses perform the dynamical decoupling while the target beam affects the state of the NV center. The effect of each pulse of the target beam is captured by an added phase, ϕ . We are assuming that the MW pulses are very short and off-resonant to the NV center by $\omega - \omega_0 = \delta\omega$. This adds a phase $\Theta = \delta\omega\tau/2$ during each free procession period of length $\tau/2$. In our experiment we omit the first and last half target pulses in measurement 1 and omit the last target pulse in measurement 2 for simplicity. Therefore, each measurement contains total of $4N - 1$ target pulses, where N is the number of XY8 pulses.

After sending N number of XY8 pulses, a total of $8N$ π pulses have been sent. The state of the NV center before the last $\pi/2$ pulse is

$$|\psi(N\tau)\rangle = \frac{\sqrt{2}}{2}(e^{-i(4N-1)\phi}|0\rangle - ie^{i(4N-1)\phi}|+1\rangle),$$

We set the last $\pi/2$ pulse in the $-\hat{y}$ direction. The state of the NV center after this pulse is

$$|\psi(N\tau)\rangle = e^{-i\pi/4}(\cos(\pi/4 - \Phi)|0\rangle - i \sin(\pi/4 - \Phi)|+1\rangle), \quad (\text{E.1})$$

where $\Phi = (4N - 1)\phi$ is the total phase induced by the target beam. Measured contrast for this state, C_1 , is

$$C_1 = C^{max} |\langle \pm 1 | \psi \rangle|^2 = \sin^2(\pi/4 - \Phi)C^{max}, \quad (\text{E.2})$$

where C^{max} is the contrast measured for $|\pm 1\rangle$ states.

The outcome of Measurement 2 similarly will be

$$C_2 = \sin^2(\pi/4 + \Phi)C^{max}, \quad (\text{E.3})$$

where the difference in the sign of Φ is due to the target pulses being sent in the opposite time slots. We calculate the phase Φ by subtracting the outcome of the two measurements,

$$C = C_1 - C_2 = \frac{C^{max}}{2}(\cos(\pi/2 + 2\Phi) - \cos(\pi/2 - 2\Phi)) = -\sin(2\Phi)C^{max}. \quad (\text{E.4})$$

In this approach, any undesired effect caused by adding the target beam (e.g., change of temperature and coherence) will be eliminated in the subtraction.

To measure C^{max} , we employ the following procedure to ensure all the effects decreasing the coherence of the quantum states are accounted for. First we calculate the contrast C^{ave} for the state $|\psi\rangle = e^{-i\pi/4}(|0\rangle - i|+1\rangle)/\sqrt{2}$. Based on the measurements performed, $C^{ave} = (C_1 + C_2)/2$. Then we measure the contrast C^{+1} for the state $|\psi\rangle = -i|+1\rangle$. This measurement is performed with a pulse sequence similar to Measurements 1 and 2 with the difference that the last $\pi/2$ pulse is in \hat{x} direction. Moreover, the target pulses are sent during both time slots to cancel out the effect of each other. The length of the pulses are set to halve of the pulses in Measurements 1 and 2 to keep the average power reaching the

NV center same as measurements 1 and 2. This way any decoherence added to the system due to presence of the target beam is accounted for in measuring C^{+1} . Then we have,

$$C^{max} = 2(C^{+1} - C^{ave}). \quad (\text{E.5})$$

If instead of the target pulses a magnetic field B parallel to the axis of the NV center was applied, then the measured contrast would have been,

$$C = \sin(2\Phi)C^{max} = -\sin((8N - 2)\phi)C^{max}, \quad (\text{E.6})$$

where $\phi = \gamma B\tau'/2$. In this equation γ is the gyromagnetic ratio for the NV center, and τ' is the length of the target pulses. Therefore, we define an effective magnetic field equivalent to the effect caused by the target beam,

$$\begin{aligned} B^{eff} &= \frac{-1}{(4N - 1)\gamma\tau'} \sin^{-1} \left(\frac{C}{C^{max}} \right), \\ &\approx \frac{-C}{(4N - 1)\gamma\tau' C^{max}} \end{aligned} \quad (\text{E.7})$$

In our experiments, shown in Fig. 3 (main text), $\tau' = 1\mu s$ and $N = 4$ is the number of XY8 pulses. For Fig. 3(c) C^{max} is measured for the two measurements as, $C_{|0\rangle \rightarrow |-1\rangle}^{max} = 20.3\% \pm 0.6$ and $C_{|0\rangle \rightarrow |+1\rangle}^{max} = 19.2\% \pm 0.9$. For Fig. 3(d) C^{max} is measured for the two measurements as, $C_{|0\rangle \rightarrow |-1\rangle}^{max} = 20.2\% \pm 0.8$ and $C_{|0\rangle \rightarrow |+1\rangle}^{max} = 19.1\% \pm 0.6$.

F. FULL-WAVE ANALYSIS OF PROPAGATION OF LIGHT IN AFM TIP

Numerical simulations presented in Fig. 3.4(c) and Fig. 3.5 are performed with CST Studio Suite. The detail of the simulation results shown in Fig. 3.4(c) is explained here. Figure F.1(a) shows the normalized amplitude of the electric field in the structure. The structure is an AFM tip on a substrate both made of diamond. The dimensions of the tip are estimates provided by QZabre company for the AFM tip we purchased. The excitation is a beam with wavelength $\lambda_0 = 800nm$ and Numerical aperture $NA = 0.65$ which resembles the target beam in our experiment [127]. Similarly to the experimental setup, the beam is x -polarized before going through a QWP and travels through the fast axis of the wave plate when the wave plate angle (θ) is zero. Due to reflection of the target beam from a dichroic mirror in the experiment, the polarization of the beam has an ellipticity of $\varepsilon = 1.08$ before entering the objective lens when the QWP is at its optimal angle. However, this ellipticity is neglected in the simulations. The power of the beam is $P = 4mW$ before the objective lens which has a measured transmission of $T = 78\%$ at this wavelength. The power of the incident beam in the simulation is set to match this transmitted power in the experiment. The beam travels in $+\hat{z}$ direction and is focused at a distance $z_0 = 1.8\mu m$ if the medium was vacuum. The parameter z_0 is chosen such to qualitatively match the simulation results to the amplitude of the measured effective field.

Figure F.1(b) shows the transverse effective field in the AFM tip in a plane $10nm$ away from the end of the tip. This plane coincides with the depth of the implanted NV center. The black circle shows the circumference of the diamond tip in this plane. The colorbar shows the amplitude of the transverse field and the black arrows show its direction. This transverse field gives rise to the dc offset in the experimental result [Fig. 3.4(c)]. If the NV center is placed off-axes to the AFM tip there would be a nonzero transverse spin component at its location. This transverse component behaves differently from the longitudinal component of the photonic spin density when changing the QWP angle, giving rise to a dc offset.

To illustrate the effect of transverse spin, we show the effective magnetic field for an NV center in $\hat{n} = (\hat{x} + \hat{y} - \hat{z})/\sqrt{3}$ direction (same as the direction of the NV center in our

experiment) placed at different locations on the transverse plane. Figure F.1(c) shows the effective magnetic field along the direction of this NV center. Each curve corresponds to a different location for the NV center marked with white dots on Fig. F.1(b). The dots have a relative distance of $d = -10nm\hat{x} + 10nm\hat{y}$ to each other. This figure clearly shows the development of the dc offset as the distance to the center of the tip increases. The Curve shown in Fig. 3.4(c) is the same as curve 7 in Fig. F.1(c).

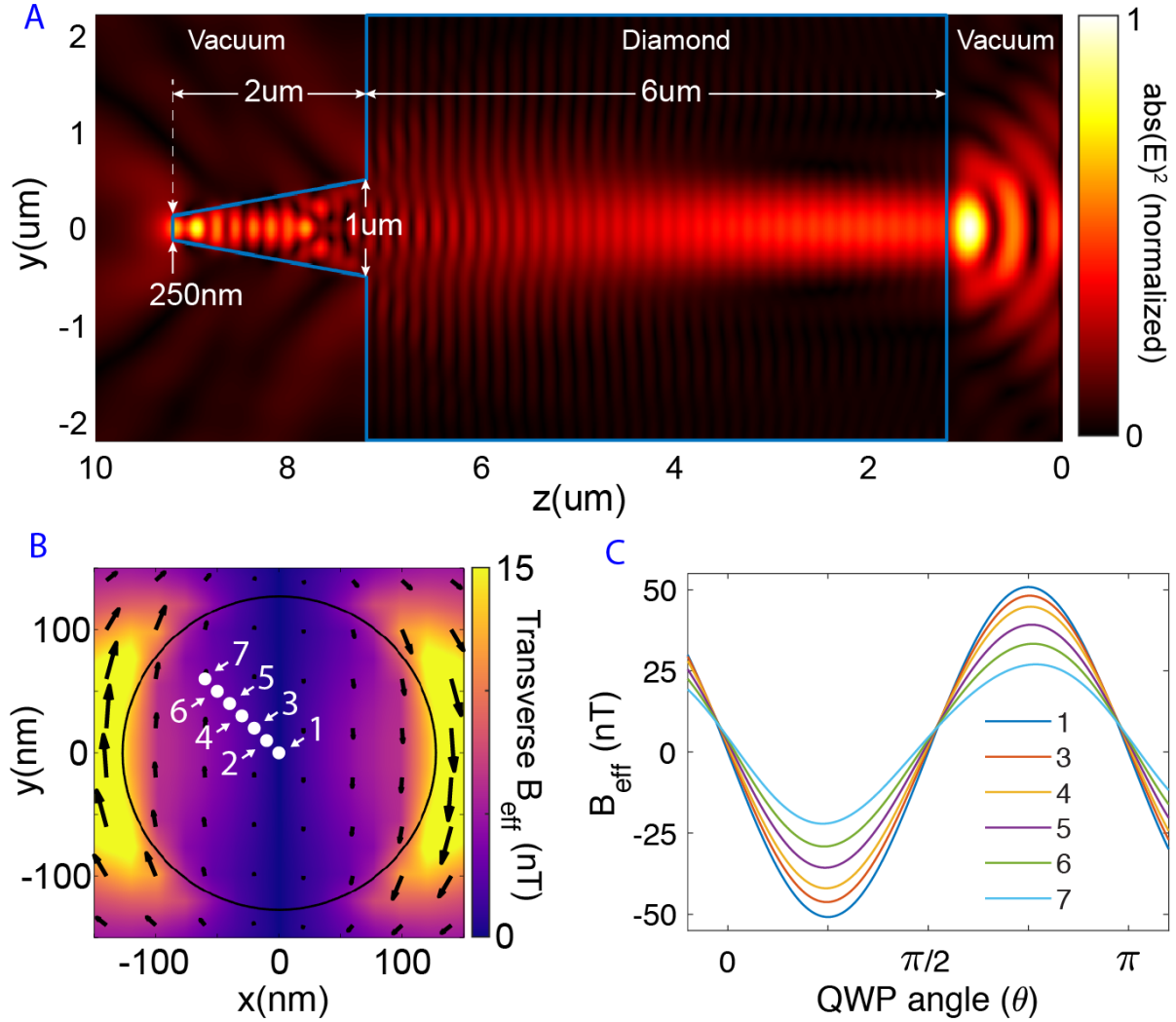


Figure F.1. Numerical simulations for the effective field amplitude in an AFM tip. (a) Amplitude of the electric field in an AFM tip made of diamond. (b) Amplitude and direction of the transverse component of the effective field in the plane of the NV center. (c) The effective field seen by an NV center with direction $\hat{n} = (\hat{x} + \hat{y} - \hat{z})/\sqrt{3}$ placed at various locations shown in panel (b) with white dots.